Eindhoven University of Technology

MASTER

Method on Steepest Descent for point sources in multi-layered media

Smink, R.W.

Award date:
2004

[Link to publication](#)

TU/e technische universiteit eindhoven
Faculty of Electrical Engineering
Division Telecommunication Technology and Electromagnetics
Chair of Electromagnetics

Method of Steepest Descent for point sources in multi-layered media

by R.W. Smink

EM-1-04

February, 2004

Report of Master Thesis performed at
TU/e, Electromagnetics Section and
TNO-FEL, The Hague

Supervisor:
Dr.ir. A. Neto (TNO-FEL)
Dr.ir. G. Gerini (TNO-FEL)
Ir. M.C. van Beurden (TU/e)
Prof.dr. A.G. Tijhuis (TU/e)

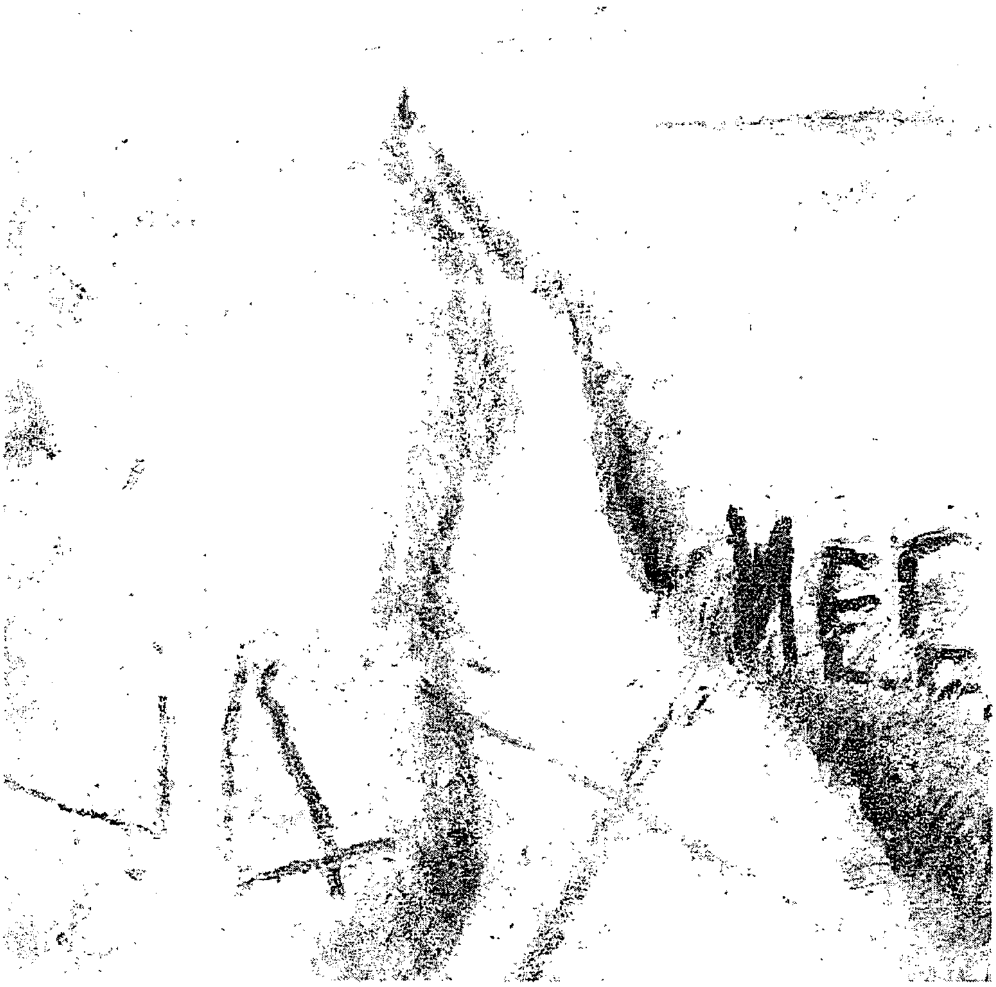

Method of Steepest Descent for point sources in multi-layered media

Rutger Smink

Method of Steepest Descent for point sources in multi-layered media

R.W. Smink

Cover design: Jan de Wachter
'De twijfel langs de weg'
Size 242-240mm

Summary

We have derived spectral dyadic Green's functions for several planarly multi-layered structures excited by electric and magnetic sources. If we transform these dyadics back to the spatial domain with the aid of the inverse Fourier transformation, we encounter the Sommerfeld Integral (SI). Since this integral cannot be evaluated in closed form, we will apply the Method of Steepest Descent to compute it numerically in an efficient way. This implies that we have to deform the integration path of the SI to the path of Steepest Descent (SDP). In this report the efficiency of integration along the SDP is demonstrated by comparing it with a slightly deformed Sommerfeld Integration Path, called the First-Contour Deformation (FCD). This latter path avoids all singularities in the plane of integration and is therefore much easier to implement. The relative error and the difference in computation time of the SI between both paths are set against each other for a structure containing a perfectly conducting ground plane with a dielectric slab on top.

Contents

Chapter 1

Introduction

Antennas for high-frequency micro-electronic systems are frequently fabricated by photolithographic techniques on dielectric substrates with different permittivities and permeabilities. To compute the electromagnetic field in such a *layered medium*, many researchers have intensively studied these structures, over the last forty years [3, 5, 6]. In the seventies and eighties, applications, such as geophysical prospecting and remote sensing, where the main reason for this study. However, most of the recent developments in this area have been driven by applications like micro-strip patch antennas, printed circuit boards, and monolithic micro- and millimeter-wave integrated circuits. Although many of these stratified structures have a simple geometric shape, their analysis is complicated by the fact that the sources are radiating in the presence of material interfaces. In those special cases where the material boundaries are conformed to a planar, cylindrical, or spherical surface, Green's functions can be obtained from the eigenvalues and eigenfunctions.

In this report only *planarly stratified media* are considered. For these structures, the eigenvectors take the form of a plane-wave spectrum. Therefore, the Green's functions will be presented in their spectral representation by using the Fourier transformation. To obtain the spatial-domain Green's functions, the inverse Fourier transformation is applied. This transformation results in the so-called *Sommerfeld Integral* (SI), whose numerical evaluation is the main topic of this report. It is of great importance that the computation of the SI is performed *efficiently*, since it has to be evaluated repeatedly in order to calculate the electromagnetic field. Several efficient techniques have been proposed to accelerate this numerical integration, like for example the Discrete Complex Image Method [13], a series representations of Green's functions using Perfectly Matched Layers [17], extrapolation methods for SI tails [16], and the *Method of Steepest Descent* [6]. The latter is the method that we will apply to compute the SI's.

The basic idea of the Method of Steepest Descent is to deform the integration path of the

SI to a path along which the integrand decreases most rapidly away from the saddle point, the so-called Path of Steepest Descent (SDP). However, since we are dealing with layered structures, surface- and leaky-wave singularities are present in the plane of integration as well. Therefore, we cannot deform the integration path arbitrarily, because if the path encounters a singularity, its contribution has to be added to the integral. To calculate this contribution, we need to find the exact location of the singularity, at the expense of extra computation time. The numerical results of the integral obtained by integration along the SDP are compared with the results obtained via a slightly deformed SI path, called the First-Contour Deformation (FCD). This FCD avoids all surface- and leaky-wave singularities and therefore no information regarding their locations is necessary. This comparison gives us an insight in the efficiency of the Method of Steepest Descent. Also the far-field asymptotic expansion is derived with the aid of the *saddle-point method*, which offers a quick way to determine the leading-order approximation of an integral. The numerical results of the far-field closed-form expressions will be compared with the results of the integral computed along the SDP, to obtain an indication for the distance beyond which the far field starts.

In Chapter 2, we start from the time-harmonic Maxwell equations to arrive at a spectral representation of the electromagnetic fields for planarly stratified structures excited by electric and magnetic point sources. To retrieve the spatial domain representation, we encounter the Sommerfeld Integral. Properties like branch cuts, branch points and singularities of the integrand are discussed in Chapter 3. In Chapter 4, we will demonstrate the possibilities when deforming an integration path. This is necessary, since the SDP can change in the plane of integration. The location of this path is also derived in this chapter, together with a search routine to find the necessary singularities in the plane of integration. Numerical results of the far-field asymptotic expressions and of the integrals computed along the SDP and the FCD are deployed in Chapter 5. Finally, conclusions are drawn in Chapter 6.

Chapter 2

General analysis of layered structures

We present a general analysis to obtain the electromagnetic field excited by an electric or magnetic point source located at $z = z' = 0$ in a stratified structure. A stratified structure with three different dielectric layers is shown in Figure 2.1. Each layer is assumed to be infinite in the x- and y-direction, which implies that edge effects, like diffraction, are absent. The thickness of a layer is denoted by d_n, where n is the number of the layer.

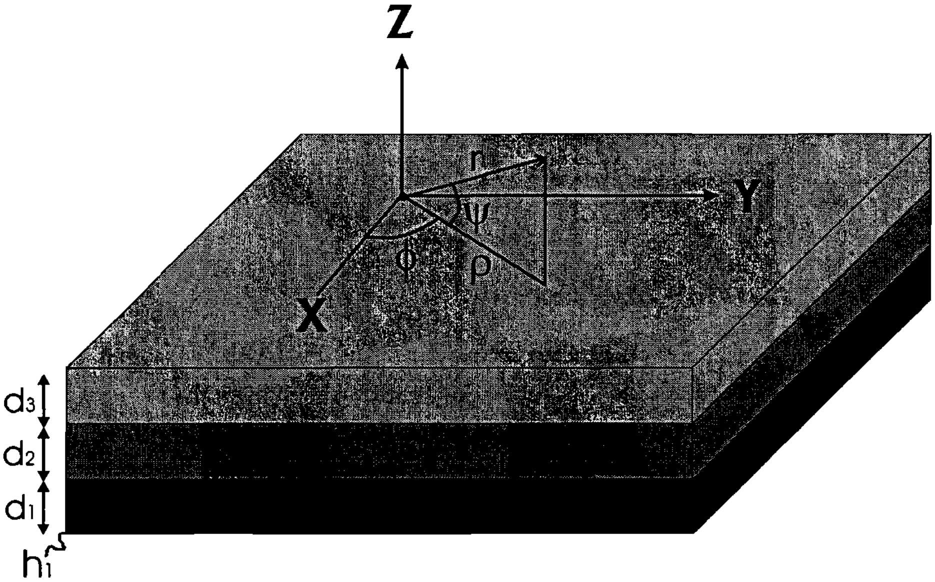

Figure 2.1: geometry of a three-layered planar structure.

2.1 Maxwell's equations

To calculate the electromagnetic field in an arbitrary point for a general stratified structure, we start from the time-harmonic Maxwell equations. With an $e^{j\omega t}$ time dependence, they are given by

$$\begin{aligned}\nabla\times\boldsymbol{E} &= -\boldsymbol{M}-j\omega\boldsymbol{B}, &\text{(2.1a)}\\ \nabla\times\boldsymbol{H} &= \boldsymbol{J}+j\omega\boldsymbol{D}, &\text{(2.1b)}\\ \nabla\cdot\boldsymbol{D} &= \rho, &\text{(2.1c)}\\ \nabla\cdot\boldsymbol{B} &= \rho_m, &\text{(2.1d)}\end{aligned}$$

where

$$\begin{array}{llll}\boldsymbol{E} & = \text{electric field,} & \boldsymbol{H} & = \text{magnetic field,}\\ \boldsymbol{D} & = \text{electric flux density,} & \boldsymbol{B} & = \text{magnetic flux density,}\\ \boldsymbol{J} & = \text{electric current density,} & \boldsymbol{M} & = \text{magnetic current density,}\\ \rho & = \text{electric charge density,} & \rho_m & = \text{magnetic charge density.}\end{array} \quad (2.2)$$

Vectors are denoted by a bold typeface. If we assume that the medium in each layer is isotropic, then the following constitutive relations apply in the absence of primary fields

$$\begin{aligned}\boldsymbol{B} &= \mu(z)\boldsymbol{H}, &\text{(2.3a)}\\ \boldsymbol{D} &= \varepsilon(z)\boldsymbol{E}, &\text{(2.3b)}\end{aligned}$$

where $\mu(z)$ and $\varepsilon(z)$ are the permeability and the permittivity of the medium, respectively. Further, we assume that all media are lossless, that each layer is homogeneous and that the permeability is independent of the height z. Since the permittivity $\varepsilon(z)$ depends on the z-coordinate, we can solve the Maxwell equations in the spectral domain.

2.1.1 Transmission-line theory

We introduce the following spatial Fourier transformations [15, 21]:

$$\begin{aligned}\tilde{\boldsymbol{E}}(\boldsymbol{k}_\rho,z,\omega) &= \int_{-\infty}^{\infty}\int_{-\infty}^{\infty}\boldsymbol{E}(\boldsymbol{r},\omega)e^{j\boldsymbol{k}_\rho\cdot\boldsymbol{\rho}}dxdy,\\ \tilde{\boldsymbol{H}}(\boldsymbol{k}_\rho,z,\omega) &= \int_{-\infty}^{\infty}\int_{-\infty}^{\infty}\boldsymbol{H}(\boldsymbol{r},\omega)e^{j\boldsymbol{k}_\rho\cdot\boldsymbol{\rho}}dxdy,\end{aligned} \quad (2.4)$$

with

$$\begin{aligned}\boldsymbol{k}_\rho &= k_x\hat{x}+k_y\hat{y},\\ \boldsymbol{\rho} &= x\hat{x}+y\hat{y},\end{aligned} \quad (2.5)$$

where $\hat{(.)}$ is a unit vector. These are vectors in the transverse plane. Variations in the z-direction are always considered in the spatial domain.

The Fourier transformation of Equation (2.4) reduces the nabla operator in Equation (2.1) to

$$\nabla_t + \hat{z}\partial_z \leftrightarrow -j\boldsymbol{k}_\rho + \hat{z}\partial_z, \tag{2.6}$$

which is decomposed in a *transverse* and *longitudinal* part. In a similar way, the electromagnetic fields are decomposed, i.e.,

$$\begin{aligned}\tilde{\boldsymbol{E}}(\boldsymbol{k}_\rho, z, \omega) &= \tilde{\boldsymbol{E}}_\rho(\boldsymbol{k}_\rho, z, \omega) + \tilde{E}_z(\boldsymbol{k}_\rho, z, \omega)\hat{z},\\ \tilde{\boldsymbol{H}}(\boldsymbol{k}_\rho, z, \omega) &= \tilde{\boldsymbol{H}}_\rho(\boldsymbol{k}_\rho, z, \omega) + \tilde{H}_z(\boldsymbol{k}_\rho, z, \omega)\hat{z},\end{aligned} \tag{2.7}$$

as well as Maxwell's equations

$$\left.\begin{aligned}-j\boldsymbol{k}_\rho \times \tilde{H}_z\hat{z} + \hat{z} \times \partial_z\tilde{\boldsymbol{H}}_\rho &= j\omega\varepsilon(z)\tilde{\boldsymbol{E}}_\rho + \tilde{\boldsymbol{J}}_\rho\\ -j\boldsymbol{k}_\rho \times \tilde{E}_z\hat{z} + \hat{z} \times \partial_z\tilde{\boldsymbol{E}}_\rho &= -j\omega\mu\tilde{\boldsymbol{H}}_\rho - \tilde{\boldsymbol{M}}_\rho\end{aligned}\right\}\text{transverse components,} \tag{2.8}$$

$$\left.\begin{aligned}-j\boldsymbol{k}_\rho \times \tilde{\boldsymbol{H}}_\rho &= j\omega\varepsilon(z)\tilde{E}_z\hat{z} + \tilde{J}_z\hat{z}\\ -j\boldsymbol{k}_\rho \times \tilde{\boldsymbol{E}}_\rho &= -j\omega\mu\tilde{H}_z\hat{z} - \tilde{M}_z\hat{z}\end{aligned}\right\}\text{longitudinal components,} \tag{2.9}$$

where we used Equation (2.3).

Next, the transverse field components $\tilde{\boldsymbol{E}}_\rho$ and $\tilde{\boldsymbol{H}}_\rho$ are expressed in components, which are parallel and orthogonal to the normalized direction $\boldsymbol{k}_\rho/k_\rho$ as [21]

$$\tilde{\boldsymbol{E}}_\rho = j\frac{\boldsymbol{k}_\rho}{k_\rho}V_{TM} - j(\hat{z} \times \frac{\boldsymbol{k}_\rho}{k_\rho})V_{TE}, \tag{2.10a}$$

$$\tilde{\boldsymbol{H}}_\rho = j(\hat{z} \times \frac{\boldsymbol{k}_\rho}{k_\rho})I_{TM} + j\frac{\boldsymbol{k}_\rho}{k_\rho}I_{TE}. \tag{2.10b}$$

The scalars $V_{TE,TM}(\boldsymbol{k}_\rho, z, z')$ and $I_{TE,TM}(\boldsymbol{k}_\rho, z, z')$ in the *transverse plane* have the same dimensions, except for the normalizing constant $1/k_\rho$, as a voltage and current along a transmission line. This property will be exploited later on. Now, let us substitute Equation (2.10a) in the longitudinal part of Equation (2.9), i.e.,

$$\begin{aligned}-j\boldsymbol{k}_\rho \times \left[j\frac{\boldsymbol{k}_\rho}{k_\rho}V_{TM} - j(\hat{z} \times \frac{\boldsymbol{k}_\rho}{k_\rho})V_{TE}\right] &= -j\omega\mu\tilde{H}_z\hat{z} - \tilde{M}_z\hat{z}\\ \Rightarrow \tilde{H}_z\hat{z} &= \left[\frac{k_\rho V_{TE} - \tilde{M}_z}{j\omega\mu}\right]\hat{z},\end{aligned} \tag{2.11}$$

which gives us an expression for the longitudinal magnetic field component $\tilde{H}_z$. Substitution of Equation (2.10b) in the longitudinal part of Equation (2.9), gives for the electric-field component $\tilde{E}_z$ the following expression

$$\begin{aligned} -j\boldsymbol{k}_\rho \times \left[j(\hat{z} \times \frac{\boldsymbol{k}_\rho}{k_\rho}) I_{TM} + j\frac{\boldsymbol{k}_\rho}{k_\rho} I_{TE} \right] &= j\omega\varepsilon(z)\tilde{E}_z\hat{z} + \tilde{J}_z\hat{z} \\ \Rightarrow \tilde{E}_z\hat{z} &= \left[\frac{k_\rho I_{TM} - \tilde{J}_z}{j\omega\varepsilon(z)} \right] \hat{z}. \end{aligned} \tag{2.12}$$

The Equations (2.10), (2.11), and (2.12) are all substituted in the transverse part of Maxwell's equations, given by Equation (2.8). If we distinguish between the components parallel and orthogonal to the direction $\boldsymbol{k}_\rho / k_\rho$ and decompose the sources in these directions as well, i.e.,

$$\begin{aligned} \tilde{\boldsymbol{J}}_\rho &= \Big(\frac{\boldsymbol{k}_\rho}{k_\rho} \cdot \tilde{\boldsymbol{J}}_\rho \Big) \frac{\boldsymbol{k}_\rho}{k_\rho} + \Big(\hat{z} \times \frac{\boldsymbol{k}_\rho}{k_\rho} \cdot \tilde{\boldsymbol{J}}_\rho \Big) \frac{\hat{z} \times \boldsymbol{k}_\rho}{k_\rho}, \\ \tilde{\boldsymbol{M}}_\rho &= \Big(\frac{\boldsymbol{k}_\rho}{k_\rho} \cdot \tilde{\boldsymbol{M}}_\rho \Big) \frac{\boldsymbol{k}_\rho}{k_\rho} + \Big(\hat{z} \times \frac{\boldsymbol{k}_\rho}{k_\rho} \cdot \tilde{\boldsymbol{M}}_\rho \Big) \frac{\hat{z} \times \boldsymbol{k}_\rho}{k_\rho}, \end{aligned} \tag{2.13}$$

we obtain the following first-order differential equations

$$\left. \begin{aligned} \partial_z I_{TM} &= -j\omega\varepsilon(z) V_{TM} + j\Big(\frac{\boldsymbol{k}_\rho}{k_\rho} \cdot \tilde{\boldsymbol{J}}_\rho \Big) \\ \partial_z V_{TM} &= \frac{k_z^2 I_{TM}}{j\omega\varepsilon(z)} + j\Big(\hat{z} \times \frac{\boldsymbol{k}_\rho}{k_\rho} \cdot \tilde{\boldsymbol{M}}_\rho \Big) + \frac{k_\rho \tilde{J}_z \hat{z}}{j\omega\varepsilon(z')} \end{aligned} \right\} \text{TM components,} \tag{2.14}$$

$$\left. \begin{aligned} \partial_z I_{TE} &= \frac{k_z^2 V_{TE}}{j\omega\mu} - j\Big(\hat{z} \times \frac{\boldsymbol{k}_\rho}{k_\rho} \cdot \tilde{\boldsymbol{J}}_\rho \Big) + \frac{k_\rho \tilde{M}_z \hat{z}}{j\omega\mu} \\ \partial_z V_{TE} &= -j\omega\mu I_{TE} + j\Big(\frac{\boldsymbol{k}_\rho}{k_\rho} \cdot \tilde{\boldsymbol{M}}_\rho \Big) \end{aligned} \right\} \text{TE components,} \tag{2.15}$$

where

$$k_z^2(z) = \omega^2 \mu \varepsilon(z) - k_\rho^2, \tag{2.16}$$

with the following requirements

$$\begin{aligned} \operatorname{Im}[k_z(z)] &\leq 0, \\ \operatorname{Re}[k_z(z)] \geq 0 \ \text{ if } \ \operatorname{Im}[k_z(z)] &= 0. \end{aligned} \tag{2.17}$$

These requirements are chosen in such a way that the radiated field remains bounded or propagates away from the source as $|z| \to \infty$ for an $e^{j\omega t}$ time dependence. In Chapter 3, the consequences of these requirements are discussed.

Equations (2.14) and (2.15) yield two coupled sets of equations. The first one is determined by the functions V_{TM} and I_{TM}. From Equation (2.11), it follows that for this type of solution, the longitudinal part of the magnetic field equals zero. Therefore, these solutions are referred to as TM-modes. On the other hand, the longitudinal part of the electric field equals zero for the functions V_{TE} and I_{TE}, according to Equation (2.12), which are therefore referred to as the TE-modes. Finally, we note that the longitudinal component $\tilde{J}_z$ only generates TM-modes, whereas the component $\tilde{M}_z$ only generates TE-modes. If a longitudinal component $\tilde{J}_z$ is located *exactly* at the transition between two media, its permittivity is given by

$$\frac{1}{\varepsilon(z')} = \frac{1}{2}\left(\frac{1}{\varepsilon(z'-)} + \frac{1}{\varepsilon(z'+)}\right), \tag{2.18}$$

where $\varepsilon(z'-)$ denotes the permittivity of the media below the transition and $\varepsilon(z'+)$ the one of the media above.

Next, we introduce the modal characteristic impedances of a transmission line [6], i.e.,

$$Z_{TM}(z) = \frac{1}{Y_{TM}(z)} = \frac{k_z(z)}{\omega\varepsilon(z)} \Big\}\text{ for } TM\text{-modes,} \tag{2.19}$$

$$Z_{TE}(z) = \frac{1}{Y_{TE}(z)} = \frac{\omega\mu}{k_z(z)} \Big\}\text{ for } TE\text{-modes.} \tag{2.20}$$

If we substitute these characteristic impedances in Equation (2.14) and (2.15), we obtain the following transmission-line equations

$$\begin{aligned} \partial_z V_p &= -jk_z Z_p I_p + v_p, \\ \partial_z I_p &= -jk_z Y_p V_p + i_p, \end{aligned} \tag{2.21}$$

where the subscript p assumes the values of TE and TM. The voltage $v_p(\boldsymbol{k}_\rho, z')$ and current $i_p(\boldsymbol{k}_\rho, z')$ sources in Equation (2.21) are given by

$$\begin{aligned} v_{TM} &= j\Big(\hat{z} \times \frac{\boldsymbol{k}_\rho}{k_\rho} \cdot \tilde{\boldsymbol{M}}_\rho\Big) + \frac{k_\rho \tilde{J}_z \hat{z}}{j\omega\varepsilon(z')},\ i_{TM} = j\Big(\frac{\boldsymbol{k}_\rho}{k_\rho} \cdot \tilde{\boldsymbol{J}}_\rho\Big), \\ i_{TE} &= -j\Big(\hat{z} \times \frac{\boldsymbol{k}_\rho}{k_\rho} \cdot \tilde{\boldsymbol{J}}_\rho\Big) + \frac{k_\rho \tilde{M}_z \hat{z}}{j\omega\mu},\ v_{TE} = j\Big(\frac{\boldsymbol{k}_\rho}{k_\rho} \cdot \tilde{\boldsymbol{M}}_\rho\Big). \end{aligned} \tag{2.22}$$

To obtain the spectral electromagnetic fields, we substitute the Equations (2.10), (2.11), and (2.12) in Equation (2.7), i.e.,

$$\begin{aligned} \tilde{\boldsymbol{E}} &= j\frac{\boldsymbol{k}_\rho}{k_\rho} V_{TM} - j(\hat{z} \times \frac{\boldsymbol{k}_\rho}{k_\rho}) V_{TE} + \left[\frac{k_\rho I_{TM} - \tilde{J}_z}{j\omega\varepsilon(z)}\right]\hat{z}, \\ \tilde{\boldsymbol{H}} &= j(\hat{z} \times \frac{\boldsymbol{k}_\rho}{k_\rho}) I_{TM} + j\frac{\boldsymbol{k}_\rho}{k_\rho} I_{TE} + \left[\frac{k_\rho V_{TE} - \tilde{M}_z}{j\omega\mu}\right]\hat{z}, \end{aligned} \tag{2.23}$$

which indicates that *outside the source region* V_{TM}, I_{TM} and V_{TE}, I_{TE} represent fields that are, respectively, TM and TE to z.

2.1.2 Source-free transmission-line equations

We shall consider a region which contains no sources. This implies that the transmission-line equations of Equation (2.21) are given by

$$\begin{aligned} \partial_z V_p &= -jk_z Z_p I_p, \\ \partial_z I_p &= -jk_z Y_p V_p, \end{aligned} \tag{2.24}$$

which are the *homogeneous source-free* transmission-line equations. Since k_z and Z_p remain constant in *each layer*, because we assumed the layers to be homogeneous, Equation (2.24) is reduced to the following second-order differential equations

$$\left[\partial_z^2 + k_{z,i}^2\right] I_p = 0, \tag{2.25a}$$

$$\left[\partial_z^2 + k_{z,i}^2\right] V_p = 0, \tag{2.25b}$$

where i denotes the layer number, as defined in Figure 2.1, and the wavenumber is, with the aid of Equation (2.16), given by

$$k_{z,i}^2 = \omega^2 \mu \varepsilon_i - k_\rho^2. \tag{2.26}$$

The solutions of the homogeneous transmission-line equations of Equation (2.25) are written in travelling-wave form as [19]

$$\begin{aligned} V_p &= V^+ e^{-jk_{z,i}(z - z')} + V^- e^{jk_{z,i}[z - (z' + d)]}, \\ I_p &= \frac{1}{Z_{p,i}} \left[V^+ e^{-jk_{z,i}(z - z')} - V^- e^{jk_{z,i}[z - (z' + d)]} \right], \end{aligned} \tag{2.27}$$

where $V^+(\boldsymbol{k}_\rho, z')$ and $V^-(\boldsymbol{k}_\rho, z')$ are the amplitudes of voltage waves at the source $z = z' = 0$ and at a transition $z = z' + d$, as shown in Figure 2.2. The first exponential term represents a wave travelling in the $+z$-direction, if we assume an $e^{j\omega t}$ time dependence. The second term represents a wave travelling in the $-z$-direction.

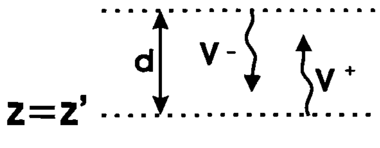

Figure 2.2: voltage waves $V^+(\boldsymbol{k}_\rho, z')$ and $V^-(\boldsymbol{k}_\rho, z')$ starting at the transitions $z = z'$ and $z = z' + d$, respectively.

2.1.3 Spectral dyadic Green's functions for the transmission-line equations

In Section 2.1.2, we have obtained a solution for the homogenous transmission-line equations in the source-free regions. To obtain a solution for Equation (2.21), we require a way to describe the source regions in the transmission line [15]. This description is simplified if we first consider point-source excitations and then obtain the total response by superposition.

In linear media, the fields due to the unit-current densities $\tilde{\boldsymbol{J}}$ and $\tilde{\boldsymbol{M}}$ may be expressed in their spectral domain representations as [6]

$$\begin{aligned} \tilde{\boldsymbol{E}} &= \langle \underline{\underline{\tilde{G}}}^{e,j}; \tilde{\boldsymbol{J}} \rangle + \langle \underline{\underline{\tilde{G}}}^{e,m}; \tilde{\boldsymbol{M}} \rangle, \\ \tilde{\boldsymbol{H}} &= \langle \underline{\underline{\tilde{G}}}^{h,j}; \tilde{\boldsymbol{J}} \rangle + \langle \underline{\underline{\tilde{G}}}^{h,m}; \tilde{\boldsymbol{M}} \rangle, \end{aligned} \tag{2.28}$$

where $\underline{\underline{\tilde{G}}}^{p,q}(\boldsymbol{k}_\rho, z, z')$ is the spectral dyadic Green's function relating p-type fields at a height z and q-type sources at z'. The notation $\langle , \rangle$ is used for integrals of products of two functions separated by the comma over the source region. The dot over the comma indicates the dot product.

In view of the linearity of the transmission-line equations of Equation (2.21), one can obtain the solutions for the functions V_p and I_p at any point z by **superposing** separate contributions from suitable point voltage- and current-generators at the point z'. In analogy with Equation (2.28), one finds [15]

$$\begin{aligned} V_p &= \langle V_p^i, i_p \rangle + \langle V_p^v, v_p \rangle, \\ I_p &= \langle I_p^i, i_p \rangle + \langle I_p^v, v_p \rangle, \end{aligned} \tag{2.29}$$

where p is either TM or TE. The functions $V_p^i(\boldsymbol{k}_\rho, z, z')$ and $V_p^v(\boldsymbol{k}_\rho, z, z')$ are so-called Transmission-Line Green's Functions (TLGF's), which are the voltage responses at z to a *unit-strength current* or *voltage source* at z', respectively. The TLGF's $I_p^i(\boldsymbol{k}_\rho, z, z')$ and $I_p^v(\boldsymbol{k}_\rho, z, z')$ are the corresponding current responses to the same excitations.

Next, let us substitute Equation (2.29) in Equation (2.23) and use Equation (2.22). If we decompose the point source $\tilde{\boldsymbol{J}}_\rho$ in x- and y-unit vectors, i.e.,

$$\tilde{\boldsymbol{J}}_\rho = \tilde{J}_x \delta(z - z')\hat{x} + \tilde{J}_y \delta(z - z')\hat{y}, \tag{2.30}$$

and use the decomposed transverse wavenumber $\boldsymbol{k}_\rho$ of Equation (2.5), then the spectral dyadic Green's functions $\underline{\underline{\tilde{G}}}^{e,j}(\boldsymbol{k}_\rho, z, z')$, $\underline{\underline{\tilde{G}}}^{h,j}(\boldsymbol{k}_\rho, z, z')$, $\underline{\underline{\tilde{G}}}^{e,m}(\boldsymbol{k}_\rho, z, z')$, and $\underline{\underline{\tilde{G}}}^{h,m}(\boldsymbol{k}_\rho, z, z')$ are, respectively, given in the *Tables* 2.1, 2.2, 2.3, and 2.4,

	$\tilde{J}_x$	$\tilde{J}_y$	$\tilde{J}_z$
$\tilde{E}_x$	$-\frac{k_x^2 V_{TM}^i + k_y^2 V_{TE}^i}{k_\rho^2}$	$\frac{k_x k_y \left[- V_{TM}^i + V_{TE}^i \right]}{k_\rho^2}$	$\frac{k_x}{k_z(z')} Z_{TM}(z') V_{TM}^v$
$\tilde{E}_y$	$\frac{k_x k_y \left[- V_{TM}^i + V_{TE}^i \right]}{k_\rho^2}$	$-\frac{k_x^2 V_{TE}^i + k_y^2 V_{TM}^i}{k_\rho^2}$	$\frac{k_y}{k_z(z')} Z_{TM}(z') V_{TM}^v$
$\tilde{E}_z$	$\frac{k_x}{k_z(z)} Z_{TM}(z) I_{TM}^i$	$\frac{k_y}{k_z(z)} Z_{TM}(z) I_{TM}^i$	$X1$ [See Equation (2.31)]

Table 2.1: spectral dyadic Green's functions $\underline{\underline{\tilde{\boldsymbol{G}}}}^{e,j}(\boldsymbol{k}_\rho, z, z')$.

	$\tilde{J}_x$	$\tilde{J}_y$	$\tilde{J}_z$
$\tilde{H}_x$	$\frac{k_x k_y \left[I_{TM}^i - I_{TE}^i \right]}{k_\rho^2}$	$\frac{k_y^2 I_{TM}^i + k_x^2 I_{TE}^i}{k_\rho^2}$	$-\frac{k_y}{k_z(z')} Z_{TM}(z') I_{TM}^v$
$\tilde{H}_y$	$-\frac{k_x^2 I_{TM}^i + k_y^2 I_{TE}^i}{k_\rho^2}$	$-\frac{k_x k_y \left[I_{TM}^i - I_{TE}^i \right]}{k_\rho^2}$	$\frac{k_x}{k_z(z')} Z_{TM}(z') I_{TM}^v$
$\tilde{H}_z$	$\frac{k_y}{k_z(z)} Y_{TE}(z) V_{TE}^i$	$-\frac{k_x}{k_z(z)} Y_{TE}(z) V_{TE}^i$	0

Table 2.2: spectral dyadic Green's functions $\underline{\underline{\tilde{\boldsymbol{G}}}}^{h,j}(\boldsymbol{k}_\rho, z, z')$.

with

$$X1 = -\frac{k_\rho^2}{k_z(z) k_z(z')} Z_{TM}(z) Z_{TM}(z') I_{TM}^v - \frac{1}{j\omega\varepsilon(z')} \delta(z - z'), \tag{2.31}$$

and

$$X2 = -\frac{k_\rho^2}{k_z(z) k_z(z')} Y_{TE}(z) Y_{TE}(z') V_{TE}^i - \frac{1}{j\omega\mu} \delta(z - z'), \tag{2.32}$$

where δ is the Dirac delta distribution.

The elements of these spectral dyadic Green's functions will be denoted as $G_{u,v}^{p,q}(\boldsymbol{k}_\rho, z, z')$, where the subscripts u, v represent the orientation of the source and observer, respectively.

Observe that the Dirac delta distribution in the Equations (2.31) and (2.32) is independent of k_ρ. This makes it possible to transform these equations back to the spatial domain, as we will see in Section 2.2. In the spatial domain, this contribution should be added if the fields at the height of the source point $z = z'$ have to be computed.

Further, we notice that if the source is directed along the z-direction, a different unit

	$\tilde{M}_x$	$\tilde{M}_y$	$\tilde{M}_z$
$\tilde{E}_x$	$\frac{k_x k_y \left[V_{TM}^v - V_{TE}^v\right]}{k_\rho^2}$	$-\frac{k_x^2 V_{TM}^v + k_y^2 V_{TE}^v}{k_\rho^2}$	$\frac{k_y}{k_z(z')} Y_{TE}(z') V_{TE}^i$
$\tilde{E}_y$	$\frac{k_y^2 V_{TM}^v + k_x^2 V_{TE}^v}{k_\rho^2}$	$-\frac{k_x k_y \left[V_{TM}^v - V_{TE}^v\right]}{k_\rho^2}$	$-\frac{k_x}{k_z(z')} Y_{TE}(z') V_{TE}^i$
$\tilde{E}_z$	$-\frac{k_y}{k_z(z)} Z_{TM}(z) I_{TM}^v$	$\frac{k_x}{k_z(z)} Z_{TM}(z) I_{TM}^v$	0

Table 2.3: spectral dyadic Green's functions $\underline{\underline{\tilde{\boldsymbol{G}}}}^{e,m}(\boldsymbol{k}_\rho, z, z')$.

	$\tilde{M}_x$	$\tilde{M}_y$	$\tilde{M}_z$
$\tilde{H}_x$	$-\frac{k_x^2 I_{TE}^v + k_y^2 I_{TM}^v}{k_\rho^2}$	$\frac{k_x k_y \left[-I_{TE}^v + I_{TM}^v\right]}{k_\rho^2}$	$\frac{k_x}{k_z(z')} Y_{TE}(z') I_{TE}^i$
$\tilde{H}_y$	$\frac{k_x k_y \left[-I_{TE}^v + I_{TM}^v\right]}{k_\rho^2}$	$-\frac{k_x^2 I_{TM}^v + k_y^2 I_{TE}^v}{k_\rho^2}$	$\frac{k_y}{k_z(z')} Y_{TE}(z') I_{TE}^i$
$\tilde{H}_z$	$\frac{k_x}{k_z(z)} Y_{TE}(z) V_{TE}^v$	$\frac{k_y}{k_z(z)} Y_{TE}(z) V_{TE}^v$	$X2$ [See Equation (2.32)]

Table 2.4: spectral dyadic Green's functions $\underline{\underline{\tilde{\boldsymbol{G}}}}^{h,m}(\boldsymbol{k}_\rho, z, z')$.

source than the one which is oriented along the x- or y-direction, should be included in the transmission line.

2.1.4 Network representation of point sources

In Section 2.1.3, we have observed that Transmission-Line Green's Functions (TLGF's) are obtained if we excite the transmission line by a unit-strength voltage or current point source. However, the location of these sources in the transmission line has not yet been specified. Therefore, we rewrite the transmission-line equations of Equation (2.21), with their point source excitations in $z = z'$ as [6]

$$\begin{aligned} \partial_z V_p &= -j k_{z,i} Z_{p,i} I_p + v_p \delta(z - z'), \\ \partial_z I_p &= -j k_{z,i} Y_{p,i} V_p + i_p \delta(z - z'), \end{aligned} \tag{2.33}$$

where δ is the Dirac delta and i is the layer number. If we integrate Equation (2.33) over z between the limits $z' - \alpha$ and $z' + \alpha$, where $\alpha \longrightarrow 0$, we obtain the following discontinuity relations for V_p and I_p at $z = z'$,

$$\left[V_p\right]_{z'-\alpha}^{z'+\alpha} = v_p(z'), \qquad \left[I_p\right]_{z'-\alpha}^{z'+\alpha} = i_p(z'). \tag{2.34}$$

These discontinuity relations can be represented by a network representation as shown in Figure 2.3, with a voltage and current point source. The voltage generator has a strength of $v_p(z')/2$ on both sides of the current generator.

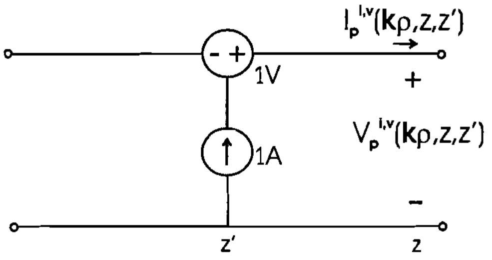

Figure 2.3: network representation for point source excitation to determine the TLGF's $I_p^{i,v}$ and $V_p^{i,v}$

2.1.5 Determination of the Transmission-Line Green's Functions (TLGF's) for a transmission-line network

As mentioned in Section 2.1, we consider a multi-layered medium with piecewise constant parameters, i.e. the permittivity and permeability remain constant in each layer. These layers can be represented by transmission lines, where we have to make sure that the boundary conditions at the junction between two of these transmission lines are satisfied. These state that V_p and I_p across a direct junction should be continuous. This property follows directly from the continuity of the transverse electric and magnetic fields at such a transition (cf. Equation (2.10)). Then, the Transmission-Line Green's Functions (TLGF's) $V_p^{i,v}$ and $I_p^{i,v}$ in a point z outside the source region can be obtained with Equation (2.27). To obtain the TLGF's inside the source region, the boundary conditions at the point source should be used. As soon as the TLGF's are known, the spectral dyadic Green's functions can be calculated to obtain the electromagnetic field.

Let us illustrate this with an example where we consider a case in which an array of waveguides is placed under a dielectric slab on a ground plane. According to the equivalence theory [2], the apertures of the waveguides are equivalent to magnetic dipoles placed on a perfect electric conductor. This is shown in Figure 2.4(a) for one aperture, represented by one magnetic point source. By superposing the contributions of several point sources with suitable amplitudes, we are able to model to total aperture of the waveguide. The equivalent transmission-line network is shown in Figure 2.4(b).

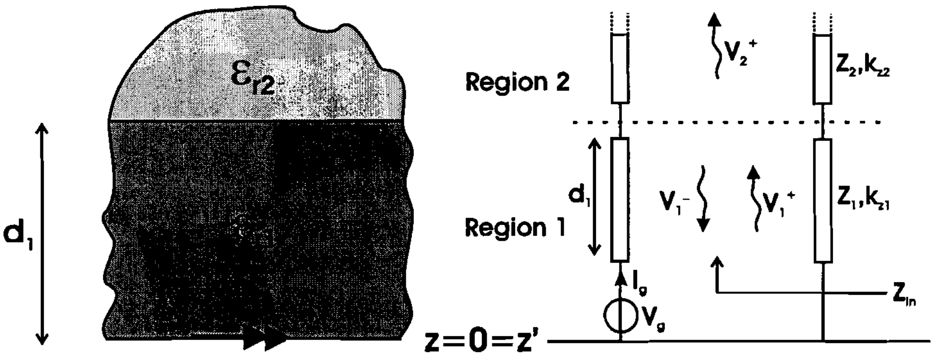

(a) (b)

Figure 2.4: 2D-geometry with a magnetic dipole on a ground plane and a dielectric slab on top (a); equivalent transmission-line network with a voltage source (V_g) in series (b)

Let us assume that we wish to calculate the magnetic field spectra in the x-direction in an observation point z. The magnetic source is located at $z = z' = 0$ and is oriented along the x-direction as well. This means that the spectral domain Green's function $G_{x,x}^{h,m}$ in *Table* 2.4 should be calculated. More specifically, the TLGF's I_{TM}^v and I_{TE}^v are needed. This means that we have to include a unit-strength voltage source in our transmission line, as shown in Figure 2.4(b).

Outside the source region, the solution of the source-free transmission-line equations are given by Equation (2.27). Since we have two regions with constant parameters, we obtain the following expressions

$$V_{p,1}^v = V_1^+ e^{-jk_{z,1}(z-z')} + V_1^- e^{jk_{z,1}[z-(z'+d_1)]}, \tag{2.35a}$$

$$I_{p,1}^v = \frac{V_1^+}{Z_{p,1}} e^{-jk_{z,1}(z-z')} - \frac{V_1^-}{Z_{p,1}} e^{jk_{z,1}[z-(z'+d_1)]}, \tag{2.35b}$$

$$V_{p,2}^v = V_2^+ e^{-jk_{z,2}[z-(z'+d_1)]}, \tag{2.35c}$$

$$I_{p,2}^v = \frac{V_2^+}{Z_{p,2}} e^{-jk_{z,2}[z-(z'+d_1)]}, \tag{2.35d}$$

where the wavenumbers are, with the aid of Equation (2.26), given by

$$\begin{array}{ll} k_z(z) = k_{z,1}^2 = \omega^2\mu\varepsilon_1 - k_\rho^2 & \text{if } z \text{ is in region 1,} \\ k_z(z) = k_{z,2}^2 = \omega^2\mu\varepsilon_2 - k_\rho^2 & \text{if } z \text{ is in region 2.} \end{array} \tag{2.36}$$

Observe that there is no wave travelling in the $-z$-direction in region 2, which implies that we only have an $e^{-jk_z z}$ behavior. To obtain the TLGF's $I_{p,1}^v$ and $I_{p,2}^v$, we need the amplitudes of the incident and reflected voltage waves, i.e. V_1^+, V_1^-, and V_2^+. This is achieved by using the boundary conditions at every transition between two layers and at the point source.

At the source, the current I_g is given by

$$I_g = \frac{V_g}{Z_{p,in}}, \tag{2.37}$$

where $Z_{p,in}$ is the input impedance of the transmission line [19], i.e.,

$$Z_{p,in} = Z_{p,1}\left[\frac{Z_{p,2} + jZ_{p,1}\tan(k_{z,1}d_1)}{Z_{p,1} + jZ_{p,2}\tan(k_{z,1}d_1)}\right], \tag{2.38}$$

in which the characteristic impedances $Z_{p,1}$ and $Z_{p,2}$ follow from Equation (2.19):

$$\left.\begin{array}{ll} Z_{TM,1}(z) = \frac{k_{z,1}}{\omega\varepsilon_1} & \text{if } z \text{ is in region } 1, \\ Z_{TM,2}(z) = \frac{k_{z,2}}{\omega\varepsilon_2} & \text{if } z \text{ is in region } 2, \end{array}\right\} \text{for } TM\text{-modes}, \tag{2.39}$$

$$\left.\begin{array}{ll} Z_{TE,1}(z) = \frac{\omega\mu}{k_1} & \text{if } z \text{ is in region } 1, \\ Z_{TE,2}(z) = \frac{\omega\mu}{k_2} & \text{if } z \text{ is in region } 2. \end{array}\right\} \text{for } TE\text{-modes}. \tag{2.40}$$

The boundary conditions at the source state that the current should be continuous there. Therefore, we obtain with the aid of the Equations (2.35b) and (2.37) the following expression:

$$\begin{aligned} I_g = I_{p,1}(z = z') &= \frac{1}{Z_{p,1}}\left(V_1^+ - V_1^-\right), \\ V_{p,2}^v &= \frac{1}{Z_{p,1}}\left(V_1^+ - V_1^-\right), \end{aligned} \tag{2.41}$$

which gives us a relationship between V_1^+ and V_1^-, i.e.,

$$\boxed{V_1^+ = \frac{Z_{p,1}V_g}{Z_{p,in}} + V_1^-.} \tag{2.42}$$

At the transition between region 1 and 2, at $z = z' + d_1$, the following boundary conditions hold

$$V_{p,1}(z = z' + d_1) = V_{p,2}(z = z' + d_1), \tag{2.43a}$$

$$I_{p,1}(z = z' + d_1) = I_{p,2}(z = z' + d_1), \tag{2.43b}$$

owing to the continuity of the transverse electric and magnetic fields, and thus

$$V_1^+e^{-jk_{z,1}d_1} + V_1^- = V_2^+, \tag{2.44a}$$

$$\frac{1}{Z_{p,1}}\left(V_1^+e^{-jk_{z,1}d_1} - V_1^-\right) = \frac{V_2^+}{Z_{p,2}}. \tag{2.44b}$$

When subtracting Equation (2.44b) from Equation (2.44a), we get a second relationship between V_1^+ and V_1^-, i.e.,

$$\boxed{V_1^- = -\left(\frac{Z_{p,1} - Z_{p,2}}{Z_{p,1} + Z_{p,2}}\right) e^{-2jk_{z,1}d_1} V_1^+.} \tag{2.45}$$

Substitution of Equation (2.45) in Equation (2.42) gives an expression for V_1^+

$$\boxed{V_1^+ = \frac{Z_{p,1}V_g}{Z_{p,in}} \frac{1}{1 + \left(\frac{Z_{p,1} - Z_{p,2}}{Z_{p,1} + Z_{p,2}}\right) e^{-2jk_{z,1}d_1}}.} \tag{2.46}$$

To get an expression for V_1^-, we can substitute Equation (2.46) in Equation (2.45). With the aid of Equation (2.35), it is now possible to calculate the TLGF's $V_{p,1}^v$ and $I_{p,1}^v$ in any observation point z along the transmission line in region 1.

To calculate the TLGF's $V_{p,2}^v$ and $I_{p,2}^v$ in region 2, we need V_2^+. Since V_1^+ and V_1^- are known, we can use Equation (2.44a) to obtain an expression for V_2^+, i.e.,

$$\boxed{V_2^+ = V_1^+ e^{-jk_{z,1}d_1} + V_1^-.} \tag{2.47}$$

Now the amplitudes V_1^-, V_1^+ and V_2^+ are known, the spectral domain Green's function $G_{x,x}^{h,m}$ in *Table* 2.4 can be calculated, since the unknown TLGF's I_{TM}^v and I_{TE}^v can be solved with the aid of Equation (2.35) in any point z along the transmission line.

2.2 Spatial domain Green's functions

In Section 2.1.3, the spectral-domain Green's functions for electric and magnetic sources and observers in terms of the TLGF's are derived. The final step in the procedure is to carry out the inverse Fourier transformations to go back to the spatial domain. These spatial Green's functions are calculated as follows

$$g_{u,v}^{p,q}(x-x', y-y', z, z') = \left(\frac{1}{2\pi}\right)^2 \int_{-\infty}^{\infty}\int_{-\infty}^{\infty} G_{u,v}^{p,q}(k_x, k_y, z, z') e^{-jk_x(x - x')} e^{-jk_y(y - y')} dk_x dk_y, \tag{2.48}$$

where the spectral Green's functions are denoted by $G_{u,v}^{p,q}$. The superscript q is either m or j, indicating a magnetic- or electric-source, where p is either h or e, representing a field component which is magnetic or electric, respectively. The subscripts u, v denote the orientation of source and observer, respectively. The coordinate (x', y', z') gives the location of the source and the coordinate (x, y, z) gives the one of the observer. If we assume that the source is located on the z-axis, we can rewrite Equation (2.48) as follows

$$g_{u,v}^{p,q}(x, y, z, z') = \left(\frac{1}{2\pi}\right)^2 \int_{-\infty}^{\infty} \int_{-\infty}^{\infty} G_{u,v}^{p,q}(k_x, k_y, z, z') e^{-j(k_x x + k_y y)} dk_x dk_y. \tag{2.49}$$

Since the spatial domain expressions are simpler to obtain in a cylindrical coordinate system, we introduce the following transformations

$$\begin{aligned} x &= \rho \cos\phi, & k_x &= k_\rho \cos(\alpha + \phi), \\ y &= \rho \sin\phi, & k_y &= k_\rho \sin(\alpha + \phi), \\ dxdy &= \rho d\rho d\phi, & dk_x dk_y &= k_\rho dk_\rho d\alpha. \end{aligned} \tag{2.50}$$

The decomposition of the vectors $\boldsymbol{k}_\rho$ and $\boldsymbol{\rho}$ are, with the aid of Equation (2.5), plotted in Figure 2.5, as well as the surface elements $\rho d\rho d\phi$ and $k_\rho dk_\rho d\alpha$. Owing to this transformation, the spatial Green's functions of Equation (2.49) can be rewritten as

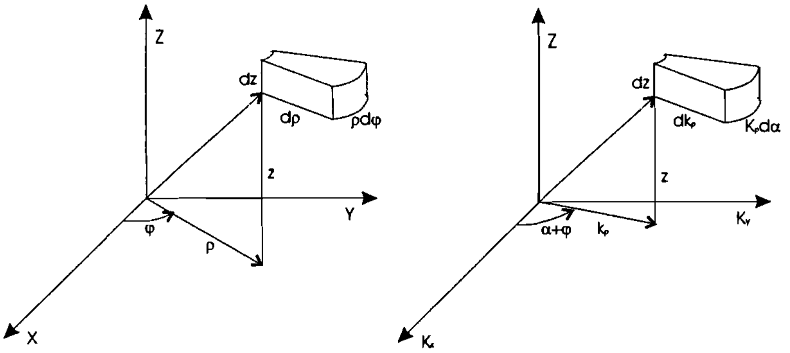

Figure 2.5: transformation to cylindrical coordinates in the spatial and spectral domain

$$g_{u,v}^{p,q}(\rho, \phi, z, z') = \left(\frac{1}{2\pi}\right)^2 \int_{0}^{\infty} \int_{\alpha=-\phi}^{2\pi-\phi} G_{u,v}^{p,q}(k_\rho, \alpha, z, z') e^{-jk_\rho \rho \cos\alpha} k_\rho d\alpha dk_\rho. \tag{2.51}$$

2.2.1 Removal of the inner integral

If we have a closer look at the spectral Green's functions $G_{u,v}^{p,q}(\boldsymbol{k}_\rho, z, z')$ in the *Tables* 2.1-2.4, we observe that we can generalize them into five different representations, i.e.,

$$
\begin{aligned}
G_1(\boldsymbol{k}_\rho, z, z') &= \frac{k_x^2 C_1 + k_y^2 C_2}{k_\rho^2}, && \text{(2.52a)}\\
G_2(\boldsymbol{k}_\rho, z, z') &= \frac{k_x k_y \left(C_3 + C_4\right)}{k_\rho^2}, && \text{(2.52b)}\\
G_3(\boldsymbol{k}_\rho, z, z') &= \frac{k_x}{k_z(z')} C_5, && \text{(2.52c)}\\
G_4(\boldsymbol{k}_\rho, z, z') &= \frac{k_x}{k_z(z)} C_6, && \text{(2.52d)}\\
G_5(\boldsymbol{k}_\rho, z, z') &= -\frac{k_\rho^2}{k_z(z) k_z(z')} C_7, && \text{(2.52e)}
\end{aligned}
$$

where $C_1(k_\rho, z, z')$—$C_7(k_\rho, z, z')$ represents a TLGF $V_p^{i,v}$ or $I_p^{i,v}$.

If we substitute the relationships $k_x = k_\rho \cos(\alpha + \phi)$ and $k_y = k_\rho \sin(\alpha + \phi)$, given by Equation (2.50) in Equation (2.52), we get

$$
\begin{aligned}
G_1(k_\rho, \alpha, z, z') &= \cos^2(\alpha + \phi) C_1 + \sin^2(\alpha + \phi) C_2 && \text{(2.53a)}\\
G_2(k_\rho, \alpha, z, z') &= \cos(\alpha + \phi) \sin(\alpha + \phi) \left(C_3 + C_4\right), && \text{(2.53b)}\\
G_3(k_\rho, \alpha, z, z') &= \frac{k_\rho \cos(\alpha + \phi)}{k_z(z')} C_5, && \text{(2.53c)}\\
G_4(k_\rho, \alpha, z, z') &= \frac{k_\rho \cos(\alpha + \phi)}{k_z(z)} C_6, && \text{(2.53d)}\\
G_5(k_\rho, \alpha, z, z') &= -\frac{k_\rho^2}{k_z(z) k_z(z')} C_7. && \text{(2.53e)}
\end{aligned}
$$

The spectral domain Green's functions $G_3^{p,q}(k_\rho, \alpha, z, z')$ and $G_4^{p,q}(k_\rho, \alpha, z, z')$ have a k_x/k_z dependence. However, if we have a look at, for example, the last column in *Table* 2.1, it is also possible to have a k_y/k_z dependence. This derivation is performed in a similar way, except for the fact that we should replace the cosine by a sine function in the Equations (2.53c) and (2.53d).

With the aid of the following identities [8]

$$\int\limits_{\alpha=-\phi}^{2\pi-\phi} \cos[\nu(\alpha+\phi)] e^{-jk_\rho \rho \cos\alpha} d\alpha = j^{-\nu} 2\pi \cos(\nu\phi) J_\nu(k_\rho \rho), \tag{2.54a}$$

$$\int\limits_{\alpha=-\phi}^{2\pi-\phi} \sin[\nu(\alpha+\phi)] e^{-jk_\rho \rho \cos\alpha} d\alpha = j^{-\nu} 2\pi \sin(\nu\phi) J_\nu(k_\rho \rho), \tag{2.54b}$$

where $J_\nu(k_\rho \rho)$ is the Bessel function of the first kind of order ν, we introduce

$$\begin{aligned} CC &= \int\limits_{\alpha=-\phi}^{2\pi-\phi} \cos^2(\alpha+\phi) e^{-jk_\rho \rho \cos\alpha} d\alpha \\ &= \frac{1}{2} \int\limits_{\alpha=-\phi}^{2\pi-\phi} \Big\{1 + \cos[2(\alpha+\phi)]\Big\} e^{-jk_\rho \rho \cos\alpha} d\alpha \\ &= \pi \big[J_0(k_\rho \rho) - \cos(2\phi) J_2(k_\rho \rho)\big], \end{aligned} \tag{2.55}$$

$$\begin{aligned} SS &= \int\limits_{\alpha=-\phi}^{2\pi-\phi} \sin^2(\alpha+\phi) e^{-jk_\rho \rho \cos\alpha} d\alpha \\ &= \pi \big[J_0(k_\rho \rho) + \cos(2\phi) J_2(k_\rho \rho)\big], \\ CS &= \int\limits_{\alpha=-\phi}^{2\pi-\phi} \cos(\alpha+\phi) \sin(\alpha+\phi) e^{-jk_\rho \rho \cos\alpha} d\alpha \\ &= -\pi \sin(2\phi) J_2(k_\rho \rho), \end{aligned} \tag{2.56}$$

where the angles α and ϕ are shown in Figure 2.5. The TLGF's $C(k_\rho, z, z')$ are independent of α, because the wavenumber $k_{z,i}$, the only parameter dependent on k_x and k_y, is in cylinder coordinates, with the aid of Equation (2.16), given by

$$\begin{aligned} k_{z,i}^2 &= k_i^2 - k_x^2 - k_y^2 \\ &= k_i^2 - k_\rho^2[\cos^2(\alpha+\phi) + \sin^2(\alpha+\phi)] \\ &= k_i^2 - k_\rho^2, \end{aligned} \tag{2.57}$$

where $k_i^2 = \omega^2 \mu \varepsilon_i$. This yields the following expressions for the five spectral Green's functions of Equation (2.53) in the spatial domain

$$\begin{aligned} g_1(\rho, \phi, z) = \left(\frac{1}{2\pi}\right)^2 \int\limits_0^\infty \Big\{ & \pi \big[J_0(k_\rho \rho) - \cos(2\phi) J_2(k_\rho \rho)\big] C_1 \\ & + \pi \big[J_0(k_\rho \rho) + \cos(2\phi) J_2(k_\rho \rho)\big] C_2 \Big\} k_\rho dk_\rho, \end{aligned} \tag{2.58}$$

$$\begin{aligned} g_2(\rho,\phi,z) = \left(\frac{1}{2\pi}\right)^2 \int\limits_0^\infty \Big\{ &- \pi\big[\sin(2\phi)J_2(k_\rho\rho)\big]C_3 \\ &- \pi\big[\sin(2\phi)J_2(k_\rho\rho)\big]C_4\Big\}k_\rho dk_\rho, \end{aligned} \tag{2.59}$$

$$g_3(\rho,\phi,z) = \left(\frac{1}{2\pi}\right)^2 \int\limits_0^\infty \frac{2\pi\cos\phi J_1(k_\rho\rho)}{jk_z(z')}C_5 k_\rho^2 dk_\rho, \tag{2.60}$$

$$g_4(\rho,\phi,z) = \left(\frac{1}{2\pi}\right)^2 \int\limits_0^\infty \frac{2\pi\cos\phi J_1(k_\rho\rho)}{jk_z(z)}C_6 k_\rho^2 dk_\rho, \tag{2.61}$$

and

$$g_5(\rho,\phi,z) = \left(\frac{1}{2\pi}\right)^2 \int\limits_0^\infty -\frac{2\pi J_0(k_\rho\rho)}{k_z(z)k_z(z')}C_7 k_\rho^3 dk_\rho. \tag{2.62}$$

For subsequent application, it will be useful to extend the range of integration in k_ρ from $-\infty$ to ∞. Since the TLGF's C are even functions, owing to their k_ρ^2 dependence, as can be seen in Equation (2.57), and by using the fact that [8]

$$J_\nu(k_\rho\rho) = \big[H_\nu^{(1)}(k_\rho\rho) + H_\nu^{(2)}(k_\rho\rho)\big]/2, \tag{2.63}$$

where $H_\nu^{(1)}$ and $H_\nu^{(2)}$ are the Hankel functions of the first and second kind of order ν, respectively, we obtain, with the aid of the reflection formula

$$-e^{j\nu\pi}H_\nu^{(1)}(k_\rho\rho) = H_\nu^{(2)}(k_\rho\rho e^{-j\pi}), \tag{2.64}$$

the following spatial domain Green's functions:

$$\begin{aligned} g_1(\rho,\phi,z) = \left(\frac{1}{8\pi}\right) \int\limits_{-\infty}^\infty \Big\{&\big[H_0^{(2)}(k_\rho\rho) - \cos(2\phi)H_2^{(2)}(k_\rho\rho)\big]C_1 \\ &+ \big[H_0^{(2)}(k_\rho\rho) + \cos(2\phi)H_2^{(2)}(k_\rho\rho)\big]C_2\Big\}k_\rho dk_\rho, \end{aligned} \tag{2.65}$$

$$\begin{aligned} g_2(\rho,\phi,z) = \left(\frac{1}{8\pi}\right) \int\limits_{-\infty}^\infty \Big\{ &- \big[\sin(2\phi)H_2^{(2)}(k_\rho\rho)\big]C_3) \\ &- \big[\sin(2\phi)H_2^{(2)}(k_\rho\rho)\big]C_4\Big\}k_\rho dk_\rho, \end{aligned} \tag{2.66}$$

$$g_3(\rho,\phi,z) = \left(\frac{1}{4\pi}\right) \int\limits_{-\infty}^\infty \frac{\cos\phi H_1^{(2)}(k_\rho\rho)}{jk_z(z')}C_5 k_\rho^2 dk_\rho, \tag{2.67}$$

$$g_4(\rho,\phi,z) = \left(\frac{1}{4\pi}\right)\int_{-\infty}^{\infty} \frac{\cos\phi H_1^{(2)}(k_\rho\rho)}{jk_z(z)} C_6 k_\rho^2 dk_\rho, \tag{2.68}$$

and

$$g_5(\rho,\phi,z) = \left(\frac{1}{4\pi}\right)\int_{-\infty}^{\infty} -\frac{H_0^{(2)}(k_\rho\rho)}{k_z(z)k_z(z')} C_7 k_\rho^3 dk_\rho. \tag{2.69}$$

If we now introduce the integrals

$$I_1(k_\rho,\rho,z,z') = \int_{-\infty}^{\infty} A_1(k_\rho,z,z')H_0^{(2)}(k_\rho\rho)k_\rho dk_\rho, \tag{2.70a}$$

$$I_2(k_\rho,\rho,z,z') = \int_{-\infty}^{\infty} A_2(k_\rho,z,z')H_2^{(2)}(k_\rho\rho)k_\rho dk_\rho, \tag{2.70b}$$

$$I_3(k_\rho,\rho,z,z') = \int_{-\infty}^{\infty} A_3(k_\rho,z,z')H_1^{(2)}(k_\rho\rho)k_\rho^2 dk_\rho, \tag{2.70c}$$

$$I_4(k_\rho,\rho,z,z') = \int_{-\infty}^{\infty} A_4(k_\rho,z,z')H_1^{(2)}(k_\rho\rho)k_\rho^2 dk_\rho, \tag{2.70d}$$

$$I_5(k_\rho,\rho,z,z') = \int_{-\infty}^{\infty} A_5(k_\rho,z,z')H_0^{(2)}(k_\rho\rho)k_\rho^3 dk_\rho, \tag{2.70e}$$

we can write all spatial Green's functions in terms of these integrals $I_n(k_\rho,\rho,z,z')$, with $n = 1,2,3,4,5$, where $A_n(k_\rho,z,z')$ are functions containing the TLGF's, and consequently depend on the geometry of the dielectric stratification. The results of the four cases for various types of source and observer oriented along the x-, y-, or z-direction are stated in Appendix C.

2.3 Possible configurations of layered structures

Since we have chosen for an approach in which we have to solve the transmission-line equations of Equation (2.21) for **each** possible layer configuration for various excitations by hand, this method is very time-consuming. Therefore, we have made a selection of the most frequently used layered structures in practice. In Figure 2.6, these configurations are shown, and are denoted by 'Sel', which stands for selection.

The selections with a number less than 10, are terminated on both sides by half spaces. In practice, only horizontally or vertically placed electric dipoles can exist here, because of the absence of a ground plane.

The selections of values between 10 and 20 contain *one* perfectly conducting ground plane at h_1. The distances d_1, d_2 and d_3 are **all** positive or negative, implying that the ground plane is on top of or at the bottom of the total layered structure. The position of the horizontal electric dipole is arbitrary as long as it is not located on the ground plane, where it is short-circuited. The horizontal magnetic dipole, on the other hand, should be located on the ground plane. In practice, these configurations are used to simulate a waveguide array with several dielectric layers on top, in which patches can be included.

For the selections above 20, the layered media are terminated by two perfectly conducting ground planes located at h_1 and h_2. For practical purposes, one can think of a parallel-plate waveguide.

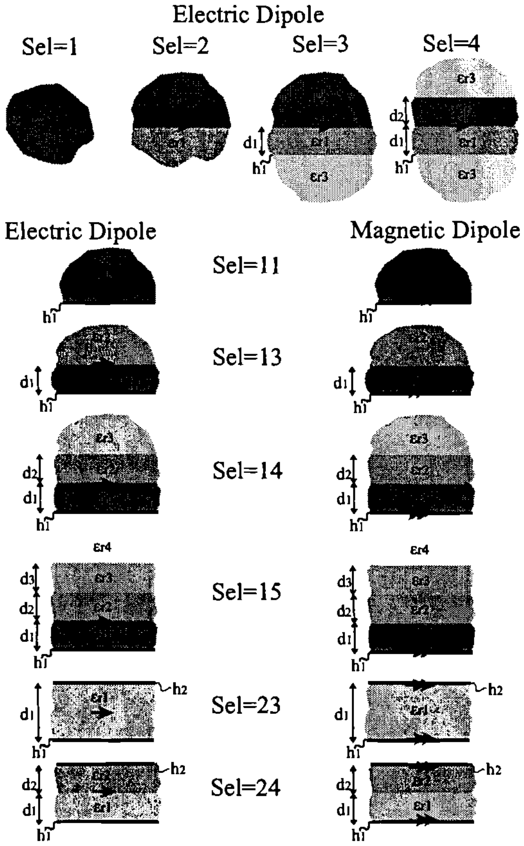

Figure 2.6: some practical configurations, which are analyzed by solving the transmission-line equations for various source and observation points.

Chapter 3

Topology of the k_ρ-plane

In Equation (2.70), we distinguished between five types of infinite integrals. Since these integrals cannot be evaluated in closed form, we have to perform a numerical integration. Therefore, a study of the complex k_ρ-plane, in which the integrals have to be computed, is necessary. The presence of the Hankel function and, in case of a half space, the wavenumber k_z in the integrals introduces so-called *branch points* and *branch cuts* in the k_ρ-plane. Their locations are discussed in the Sections 3.1 and 3.2, respectively. In Appendix B, a basic introduction of these subjects is presented.

Due to the branch cuts, the integration path, now located along the real k_ρ-axis, has to be deformed to the so-called *Sommerfeld Integration Path.* This path is introduced in Section 3.3. In Section 3.4, we will discuss the presence of *surface-* and *leaky-wave singularities* in the k_ρ-plane, which correspond to the poles of the functions $A_n(k_\rho, z, z')$ in Equation (2.70). Although their exact location depends on the geometry of the stratified structures, they can only occur in certain regions of the k_ρ-plane. In Section 3.5, a final composition of the k_ρ-plane is made.

3.1 Location of the branch points

A point $k_\rho = \alpha$ is called a branch point of $f(k_\rho)$ if there is some small enough circle surrounding α such that when k_ρ continuously traverses the circle once, then $f(k_\rho)$

- changes continuously with k_ρ,
- but does not return to its original value.

As discussed in Appendix B, the complex logarithm function $\ln(k_\rho)$ and the complex square root function $\sqrt{k_\rho}$ have branch points, located at the origin. The complex logarithm function is present in the Hankel function, and the complex square root function is present in the wavenumber k_z, as we will discuss in the Sections 3.1.1 and 3.1.2, respectively.

3.1.1 Branch point of $H_\nu^{(2)}(k_\rho \rho)$

The Hankel function of the second kind $H_\nu^{(2)}(k_\rho \rho)$, with order $\nu = 0, 1, 2$ for the integrals of Equation (2.70), has the following form in terms of Bessel functions of the first and second kind [10]:

$$H_\nu^{(2)}(k_\rho \rho) = J_\nu(k_\rho \rho) - jY_\nu(k_\rho \rho). \tag{3.1}$$

These Bessel functions can be written as ascending series, i.e.,

$$\begin{aligned}
J_\nu(z) =& \left(\frac{1}{2}z\right)^\nu \sum_{k=0}^{\infty} \frac{(-\frac{1}{4}z^2)^k}{k!(\nu+k)!}, \\
Y_m(z) =& -\frac{(\frac{1}{2}z)^{-m}}{\pi} \sum_{k=0}^{m-1} \frac{(m-k-1)!}{k!} \left(\frac{1}{4}z^2\right)^k \\
& + \frac{2}{\pi} \ln\left(\frac{1}{2}z\right) J_m(z) - \frac{(\frac{1}{2}z)^{-\nu}}{\pi} \sum_{k=0}^{\infty} \left[\Psi(k+1) + \Psi(m+k+1)\right] \frac{(\frac{1}{4}z^2)^k}{k!(m+k)!}, \\
Y_0(z) =& \frac{2}{\pi}\left[\ln\left(\frac{1}{2}z\right) + \gamma\right] J_0(z) \\
& + \frac{2}{\pi}\left[\frac{\frac{1}{4}z^2}{(1!)^2} - (1+1/2)\frac{(\frac{1}{4}z^2)^2}{(2!)^2} + (1+1/2+1/3)\frac{(\frac{1}{4}z^2)^3}{(3!)^2} - \ldots\right],
\end{aligned} \tag{3.2}$$

where

$$\begin{aligned}
\Psi(1) &= \text{Euler's constant} = \gamma = 0.5772156649, \\
\Psi(\nu) &= -\gamma \sum_{k=1}^{\nu-1} k^{-1},
\end{aligned} \tag{3.3}$$

and $m = 1, 2, \ldots.$ In the ascending series of $Y_\nu(z)$, where $\nu = 0, 1, 2\ldots$, we encounter the complex logarithm function. Therefore, the Hankel function has one branch point located at the origin of the complex k_ρ-plane, as shown in Appendix B. Hence, we do not return to our original value if we encircle the origin once.

3.1.2 Branch points of k_z

The functions $A_n(k_\rho, z, z')$ in Equation (2.70) contain the Transmission-Line Green's Functions (TLGF's), and therefore depend on the wavenumber $k_{z,i}$. Although the square of this wavenumber is well-defined, i.e.,

$$k_{z,i}^2 = k_i^2 - k_\rho^2, \tag{3.4}$$

where we used a general notation of Equation (2.36), with i the layer in which the observer z is located, we have a double-valued function for $k_{z,i}$ itself. If we take $k_{z,i}^2 = \zeta$, where $\zeta \in C$, then the principal square root is defined as [18]

$$k_{z,i} = \sqrt{\zeta} := \sqrt{|\zeta|}e^{j[\arg(\zeta)]/2} \qquad -\pi < \arg(\zeta) \leq \pi. \tag{3.5}$$

A possible square root solution for Equation (3.4) is given by

$$k_{z,i} = -j\sqrt{-(k_i^2 - k_\rho^2)}. \tag{3.6}$$

To locate the branch points of Equation (3.6), we rewrite it as follows

$$\begin{aligned} k_{z,i} &= -j\sqrt{-(k_i + k_\rho)(k_i - k_\rho)} \\ &= -j\exp\left\{\left[\ln|k_i + k_\rho||k_i - k_\rho| + j\arg(k_i - k_\rho) + j\arg(k_i + k_\rho) + j\pi\right]/2\right\}, \end{aligned} \tag{3.7}$$

where we used the fact that

$$f(z) = z^\alpha = e^{\alpha \ln(z)} = e^{\alpha[\ln|z| + j\arg(z)]}. \tag{3.8}$$

If k_ρ encircles either the point $k_\rho = -k_i$ or $k_\rho = k_i$ once, then the corresponding value of $\arg(k_\rho + k_i)$ or $\arg(k_\rho - k_i)$ changes by 2π, so that $k_{z,i}$ changes sign. This implies that we have two branch points, i.e.,

$$k_\rho = \pm k_i. \tag{3.9}$$

The wavenumbers k_i are real, since we assumed that the materials of the layers are lossless, as mentioned in Section 2.1. Hence, the branch points are located on the real k_ρ-axis.

3.1.3 Absence of branch points

Since we have an attenuation factor $k_{z,i}$ for every layer, one might think that each layer has branch points. However, this is not true. Therefore, let us recall the geometry used in Section 2.1.5. We assume that the observation point z is located in region 2 and that we wish to calculate the function $A_1(k_\rho, z, z')$ of the integral I_1 for the spatial Green's function $g^{h,m}_{x,x}(\rho, \phi, z)$. Then we obtain, with the aid of Equation (2.35),

$$\begin{aligned} A_1(k_\rho, z, z') &= -I^v_{TE} - I^v_{TM} \\ &= -\frac{V_2^+}{Z_{TE_2}} e^{-jk_{z,2}z} - \frac{V_2^+}{Z_{TM_2}} e^{-jk_{z,2}z}, \end{aligned} \tag{3.10}$$

where V_2^+ is given by Equation (2.47). Substitution of V_2^+ in Equation (3.10) gives for I^v_p the following expression:

$$\begin{aligned} I^v_p =& 2\left[\frac{Z_{p,1} + jZ_{p,2}\tan(k_{z,1}d_1)}{Z_{p,2} + jZ_{p,1}\tan(k_{z,1}d_1)}\right] \\ &\times \frac{e^{jk_{z,2}(h_1 + d_1 - z)}}{(Z_{p,1} + Z_{p,2})e^{jk_{z,1}(h_1 + d_1 - z')} + (Z_{p,1} - Z_{p,2})e^{-jk_{z,1}(h_1 + d_1 - z')}}, \end{aligned} \tag{3.11}$$

where the subscript p is either TM or TE. The characteristic impedances Z_p are given by Equation (2.39).

If we have a closer look at this expression, we see that if we take $k_{z,1} = -k_{z,1}$ the same expression is obtained. This implies that it does not matter which definition for the square root of Equation (3.4) we take, since all give identical results. Therefore, we can state that for wavenumbers $k_{z,i}$ that correspond to a layer, no branch points exist. However, if we replace the wavenumber $k_{z,2}$ by $-k_{z,2}$, we obtain different results out of Equation (3.11). This implies that we have two branch points for this geometry at $k_\rho = \pm k_2$, which correspond to the half space region.

Hence, the branch points are always associated with the half spaces. Since we can have at most two half spaces, as can be seen in Figure 2.6, the maximum number of branch points is four. If our structure is terminated by two perfectly conducting ground planes, we do not have any branch points. This can be verified with Equation (2.21) combined with the radiation conditions of Equation (2.17).

3.2 Location of the branch cuts and Riemann sheets

To locate the branch cuts of the integrals I_n, given by Equation (2.70), the branch points are of help, since they denote the endpoints of the branch cuts [6, 7].

As discussed in Section 3.1.1, the Hankel function $H^{(2)}_\nu(k_\rho \rho)$ contains a branch point at the origin due to the complex logarithm function. In Figure 3.1, a plot of the Hankel function, defined by Equation (3.1), in the complex k_ρ-plane is made. Since the results of the Hankel function are complex as well, we have only plotted the real part of the results and denoted the imaginary part by colors, as proposed in Appendix B. As long as there is no abrupt color change, the imaginary part of the result is continuous. The branch cut is clearly visible on the negative real k_ρ-axis and has indeed its endpoint at the origin.

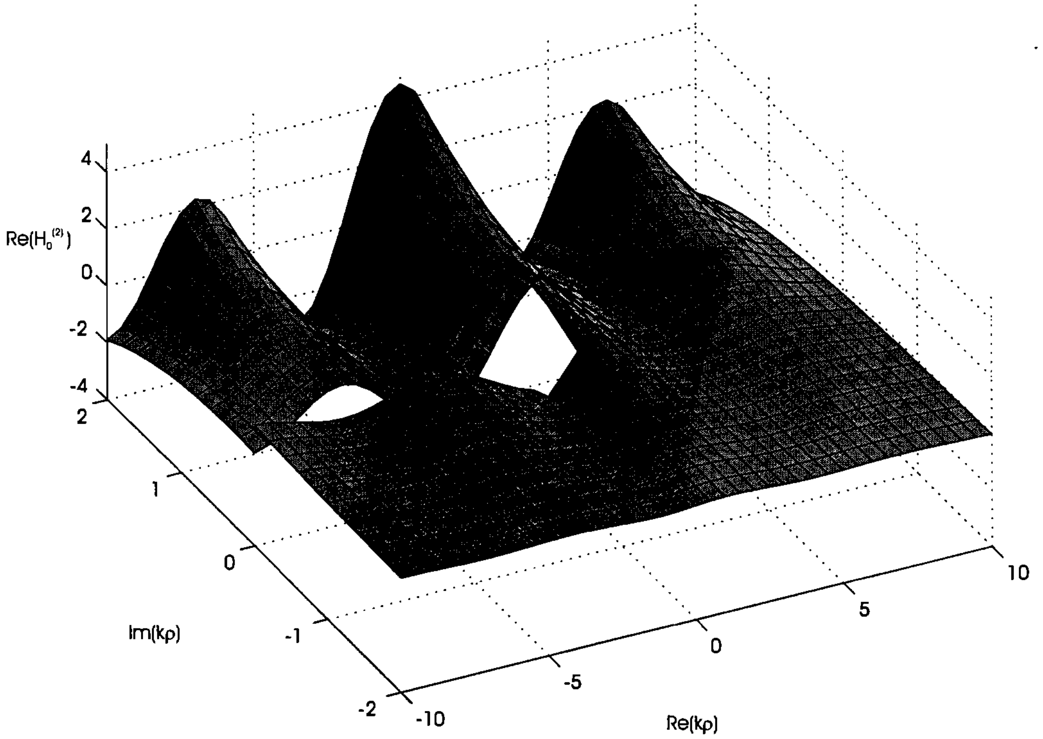

Figure 3.1: the complex Hankel function $H_\nu^{(2)}(k_\rho \rho)$ in the complex k_ρ-plane for $\rho = 1$, where the imaginary part of the Hankel function is denoted by colors.

To locate the branch cuts of the complex square root function $k_{z,i}$, we recall Equation (3.7). If we replace $(k_i + k_\rho)$ by $re^{j\theta}$ and $(k_i - k_\rho)$ by $\rho e^{j\phi}$, we obtain

$$\begin{aligned} k_{z,i} &= -j\sqrt{-r\rho e^{j(\theta+\phi)}} \\ &= -j\sqrt{r\rho}e^{j(\theta+\phi+\pi)/2} \\ &= \sqrt{r\rho}\left[\sin\left(\frac{\theta+\phi+\pi}{2}\right) - j\cos\left(\frac{\theta+\phi+\pi}{2}\right)\right]. \end{aligned} \tag{3.12}$$

The angles θ and ϕ, together with the distances ρ and r are plotted in Figure 3.2. The requirements for the wavenumber $k_{z,i}$, which follow from the radiation conditions, are given

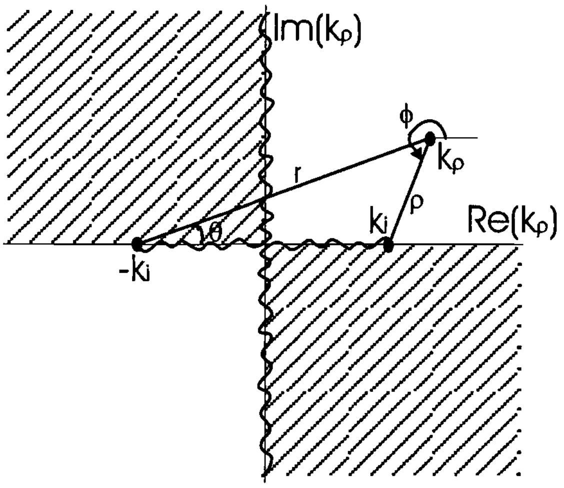

Figure 3.2: k_ρ-plane with $\mathrm{Im}(k_{z,i}) < 0$ on the entire upper Riemann sheet, $\mathrm{Re}(k_{z,i}) > 0$ in the unshaded region, $\mathrm{Re}(k_{z,i}) < 0$ in the shaded region.

by Equation (2.17). The first requirement, i.e. $\mathrm{Im}(k_{z,i}) \leq 0$, implies that

$$-\cos\left(\frac{\theta+\phi+\pi}{2}\right) \leq 0, \tag{3.13}$$

and consequently

$$-\pi < \theta + \phi + \pi \leq \pi. \tag{3.14}$$

This is the same domain as the one of the principal square root of Equation (3.5), which is the reason why we have chosen for this square root definition. This means that the $\mathrm{Im}(k_{z,i}) < 0$ on the entire *upper Riemann sheet*. To go from this upper Riemann sheet to the lower one, where $\mathrm{Im}(k_{z,i}) > 0$, we have to cross the branch cuts at $\mathrm{Im}(k_{z,i}) = 0$. From Equation (3.12) it follows that the branch cuts are located at those points in the k_ρ-plane where

$$\theta + \phi = 0, \pm 2\pi, \pm 4\pi, \ldots \tag{3.15}$$

These branch cuts are shown in Figure 3.2 as well. If we now look at the real part of $k_{z,i}$, which is the sine part of Equation (3.12), we see that the unshaded region in Figure 3.2 corresponds to $\mathrm{Re}(k_{z,i}) > 0$ and the shaded one to $\mathrm{Re}(k_{z,i}) < 0$. Also, note that the branch cuts do not cross in the origin.

In Figure 3.3, we plotted the complex square root definition of Equation (3.6) again by using colors to denote the imaginary part of $k_{z,i}$, as proposed in Appendix B. We can distinguish between the two branch cuts in this figure as well, i.e.,

$$\text{branch cut 1:} \quad \left\{ \begin{array}{l} 0 \leq \mathrm{Re}(k_\rho) \leq k_i \\ \mathrm{Im}(k_\rho) = 0 \end{array} \right. \quad \text{and} \quad \left\{ \begin{array}{l} -\infty \leq \mathrm{Im}(k_\rho) \leq 0 \\ \mathrm{Re}(k_\rho) = 0 \end{array} \right. , \tag{3.16}$$

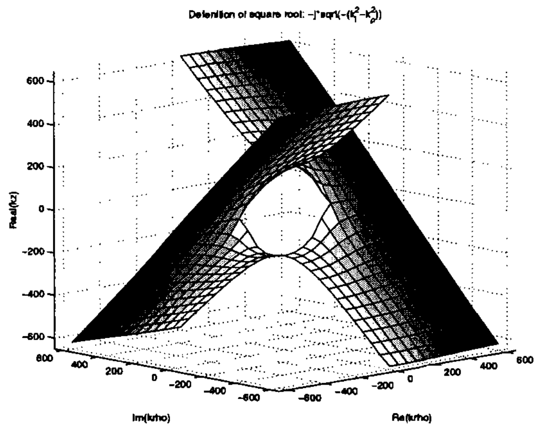

Figure 3.3: the complex square root $k_{z,i} = -j\sqrt{-(k_i^2 - k_\rho^2)}$ with $k_i = 209.5$.

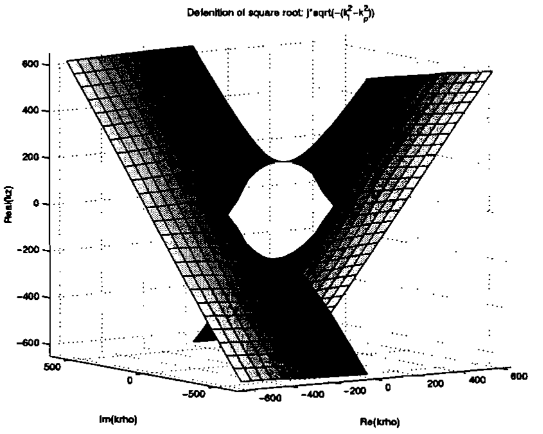

Figure 3.4: the complex square root $k_{z,i} = j\sqrt{-(k_i^2 - k_\rho^2)}$ with $k_i = 209.5$.

$$\text{branch cut 2:} \quad \left\{ \begin{array}{c} -k_i \leq \mathrm{Re}(k_\rho) \leq 0 \\ \mathrm{Im}(k_\rho) = 0 \end{array} \right. \quad \text{and} \quad \left\{ \begin{array}{l} 0 \leq \mathrm{Im}(k_\rho) \leq \infty \\ \mathrm{Re}(k_\rho) = 0 \end{array} \right. . \tag{3.17}$$

Again, the branch points at $k_\rho = \pm k_i = \pm 209.5$, which corresponds to a wavelength of $0.03\lambda_0$, denote the endpoints of the branch cuts.

Let us assume that we wish to pass through a branch cut to go from the upper Riemann sheet to the lower one. To guarantee continuity of the complex square root function when passing through this branch cut, we have to use a square root definition that meets the requirement that $\mathrm{Im}(k_{z,i}) > 0$ for the lower Riemann sheet. This square root definition is given by

$$k_{z,i} = j\sqrt{-(k_i^2 - k_\rho^2)}, \tag{3.18}$$

and plotted in Figure 3.4.

Now, we can combine Figure 3.3 and 3.4, to obtain a unique two-sheeted Riemann surface for the double-valued function $k_{z,i}$. This Riemann surface is shown in Figure 3.5, where the branch cuts provide the means of passing from one Riemann sheet to another. Hence, we have defined the upper and lower Riemann sheet by the following square root definitions

$$\begin{array}{rl} -j\sqrt{-(k_i^2 - k_\rho^2)} & \text{upper Riemann sheet,} \\ j\sqrt{-(k_i^2 - k_\rho^2)} & \text{lower Riemann sheet.} \end{array} \tag{3.19}$$

In Section 3.1.3, we showed that only half spaces give rise to branch points in the k_ρ-plane. This implies also that only those branch cuts that correspond to these branch points are present in the k_ρ-plane. According to [3], these branch cuts represent the **radiation modes**, i.e. a continuum of modes present in the half space carrying energy to infinity. This will be shown in Section 3.4, where we will discuss the surface-wave modes.

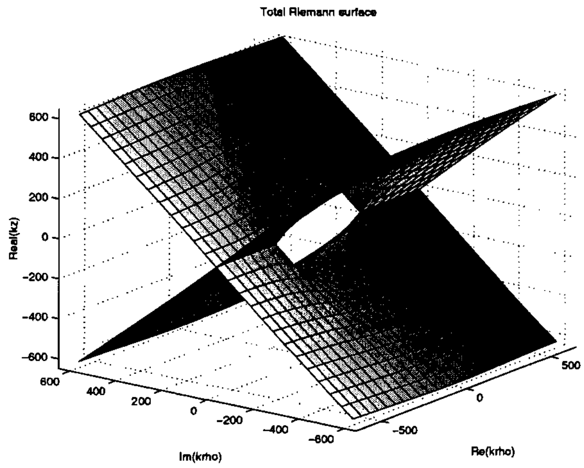

Figure 3.5: a unique two-sheeted Riemann surface obtained by combining two definitions of the complex square root of $k_{z,i}$, with $k_i = 209.5$.

3.3 Sommerfeld Integration Path (SIP)

The integration paths of the integrals I_n of Equation (2.70) are all defined on the real k_ρ-axis. As discussed in the Sections 3.1 and 3.2, branch points and branch cuts are located on this axis as well. To compute the contribution of the branch cuts, we need to know on which side of the cut the integration path passes. Therefore, let us omit the branch point and branch cut, introduced by the Hankel function, for the moment and assume that there are some small losses in the transmission line [6]. This means that for an e^{jwt} time dependence, $k_i = \omega\sqrt{\mu(\varepsilon_R - j\varepsilon_I)}$ has a small negative imaginary part $-\varepsilon_I$. Then the branch points are slightly displaced from the real k_ρ-axis, as shown in Figure 3.6. Since

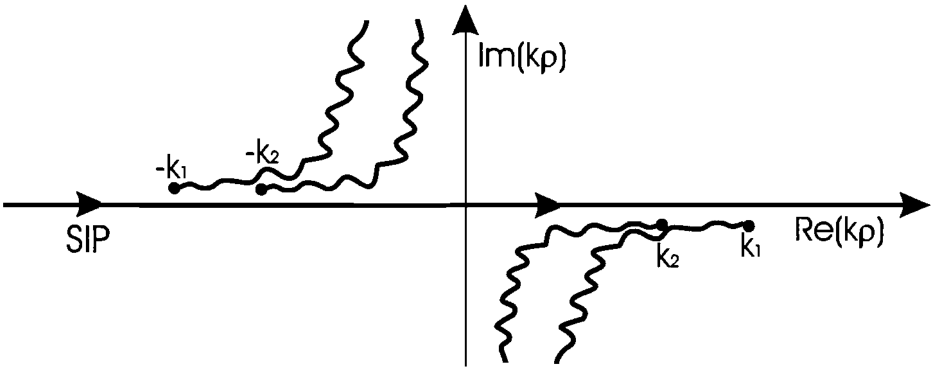

Figure 3.6: integration path in the complex k_ρ-plane with branch points displaced from the real axis due to a slight dissipation.

the endpoints of the branch cuts are the branch points, the integration path moves around these branch cuts in a similar way as it moves around the branch points. So, if we let $\varepsilon_I \downarrow 0$, we obtain the required movement of the integration path around the branch points and branch cuts.

However, in our analysis we left the branch point and branch cut of the Hankel function out. Since its branch cut is located on the negative real k_ρ-axis, our integration path cannot be situated on the axis itself. This results in the integration path, called the *Sommerfeld Integration Path* (SIP), of Figure 3.7.

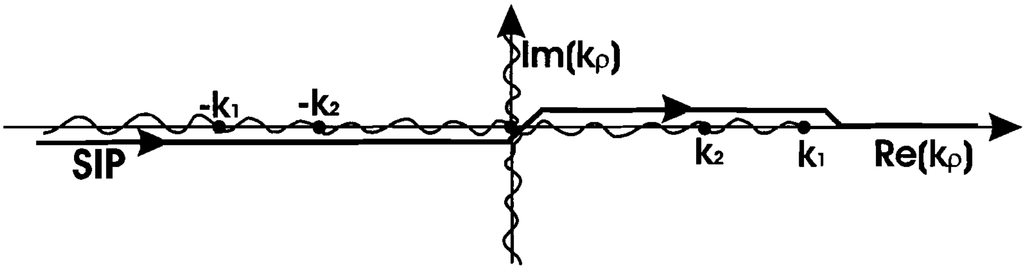

Figure 3.7: Sommerfeld Integration Path in the complex k_ρ-plane avoiding the branch cuts and branch point singularities.

Observe that the SIP does not cross the origin, due to the branch-point singularity of the Hankel function. Because of the manner in which we have selected the reflection formula for Hankel functions of Equation (2.64), the path of integration is below the branch-point singularity at the origin.

Note also that the SIP does not pass through any branch cuts. This means that the total integration path is located on the upper Riemann and consequently the $\mathrm{Im}(k_{z,i}) < 0$, as discussed in Section bc.

3.4 Surface- and leaky-wave poles

The functions $A_n(k_\rho, z, z')$ in the integrals I_n of Equation (2.70) can have singularities as well. These singularities are the so-called surface- and leaky-wave singularities/poles, located at $k_\rho = k_{sw}$ and $k_\rho = k_{lw}$, respectively. For lossless media, surface-wave singularities are only observed on a finite interval on the real k_ρ-axis. This interval is constrained by the requirement that k_{sw} may not be chosen on a branch cut [3]. Taking this condition into account, the surface-wave singularities are located on the upper Riemann sheet in a range given by

$$\max(k_{half\ spaces}) < \mathrm{Re}(k_\rho) \leq \max(k_{layers}), \tag{3.20}$$

If we have a structure, terminated by two perfectly conducting ground planes, there is no lower boundary, since there are no half spaces. The corresponding range for these structures will be discussed in Section 3.4.1.

Leaky-wave poles, on the other hand, are located on the lower Riemann sheet, as we will discuss in Section 3.4.2.

The occurrence of the surface- and leaky-wave poles depends on the geometry of the structure. Therefore, we will discuss some configurations where these singularities occur.

3.4.1 Surface waves along a dielectric slab

Surface waves of both the *TM* and *TE* type may be guided along a dielectric slab. Therefore, let us consider the geometry of Figure 3.8(a), where a slab, with a thickness $d = 0.15\lambda_0$ and $\varepsilon_{r,1} = 9$, is positioned between two half spaces. We consider λ_0 to be the wavelength of free space. The relative permittivities for both half spaces are assumed to be one, i.e. $\varepsilon_{r,2} = \varepsilon_{r,3} = 1$. The source, a horizontally placed electric dipole, is considered to be on the lower transition at $z = z' = 0$ and the observer is located somewhere above the slab in the half space region 2.

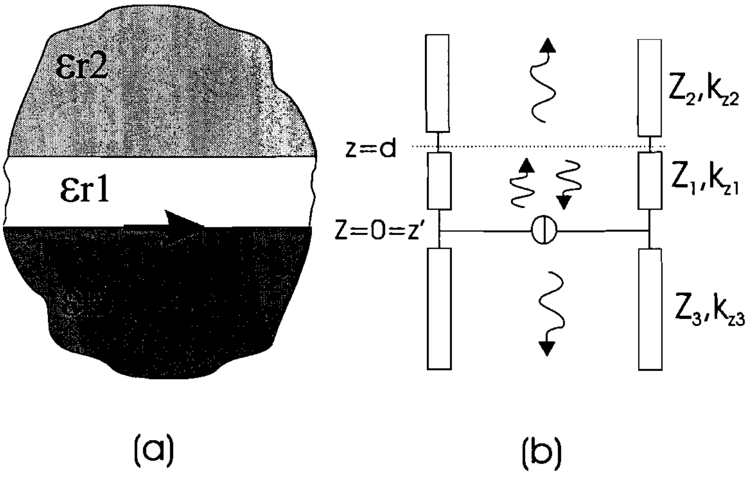

Figure 3.8: (a): a slab between two dielectric media with a horizontal electric dipole at $z = z'$; (b): equivalent transmission-line network.

To solve the homogeneous transmission-line equations of Equation (2.25), we require the equivalent transmission-line network, which is shown in Figure 3.8(b). According to *Table* 2.1, we have to include a unit-strength current source at $z = z'$. If we solve the transmission-line equations of Equation (2.21) for this network, the following denominator for the functions $A_n(k_\rho, z, z')$ is obtained

$$\mathrm{den}\big[A_n(k_\rho, z, z')\big] = Z_{p,3}\big[Z_{p,1} + jZ_{p,2}\tan(k_{z,1}d)\big] + Z_{p,1}\big[Z_{p,2} + jZ_{p,1}\tan(k_{z,1}d)\big]. \tag{3.21}$$

In Figure 3.9, this denominator is plotted for p is TM or TE. The surface-wave pole locations are the zeros in this plot.

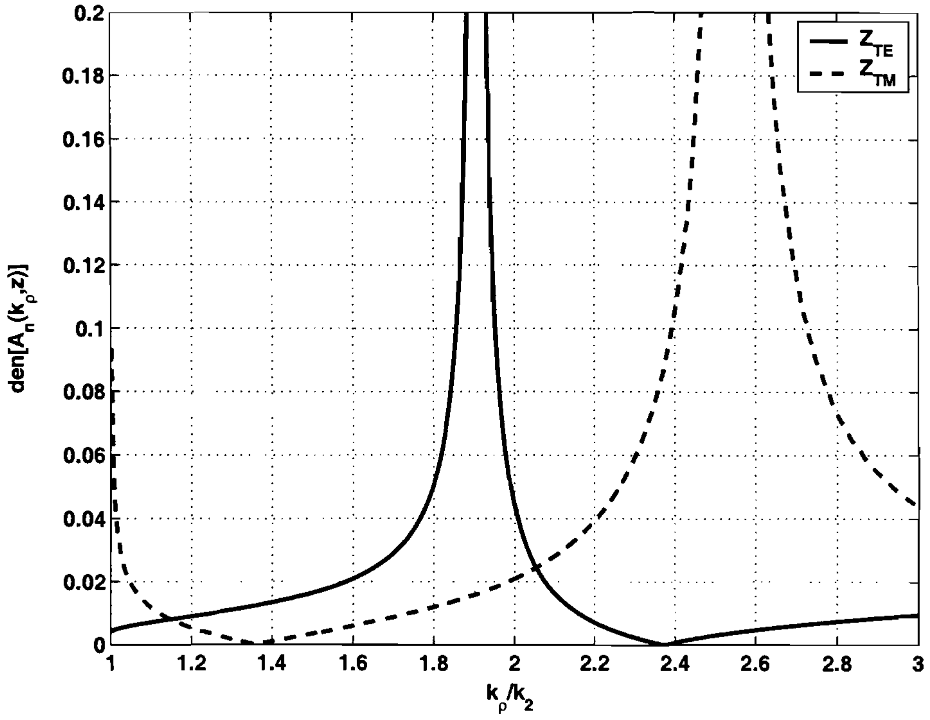

Figure 3.9: location of a TM surface-wave pole at $k_\rho \approx 1.36k_2$ and a TE surface-wave pole at $k_\rho \approx 2.37k_2$, with $k_1 = 3k_2 = 3k_3$ and $d = 0.15\lambda_0$.

In [6, p. 292], another graphical way to find these surface-wave poles is discussed. Not only the surface-wave poles on the upper Riemann sheet, as in Figure 3.9, but also the ones on the lower sheet are visualized there. This is achieved by introducing the following variables for the wavenumbers

$$\begin{aligned} k_{z,1} &= h = -j\sqrt{-(k_1^2 - k_\rho^2)}, \\ k_{z,2} = k_{z,3} &= -jp = -j\sqrt{-(k_2^2 - k_\rho^2)}, \end{aligned} \tag{3.22}$$

which gives us the following equations

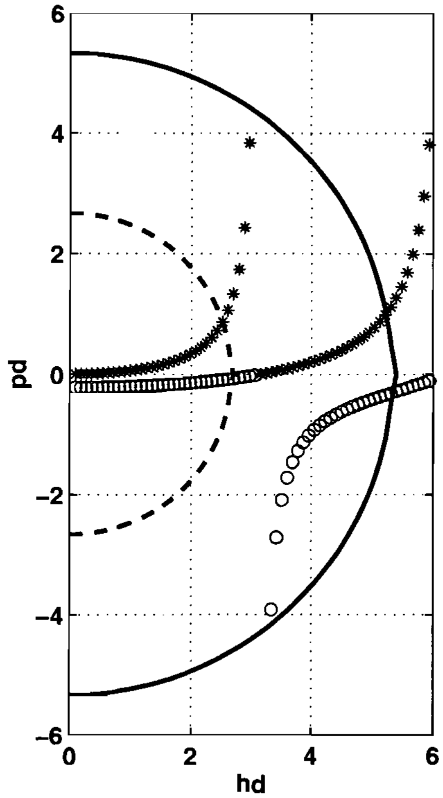

Figure 3.10: graphical solution of the *TM* roots of $\mathrm{den}\left[A_n(k_\rho, z)\right]$, where the dashed line corresponds to $d = 0.15\lambda_0$ and the solid one to $d = 0.3\lambda_0$.

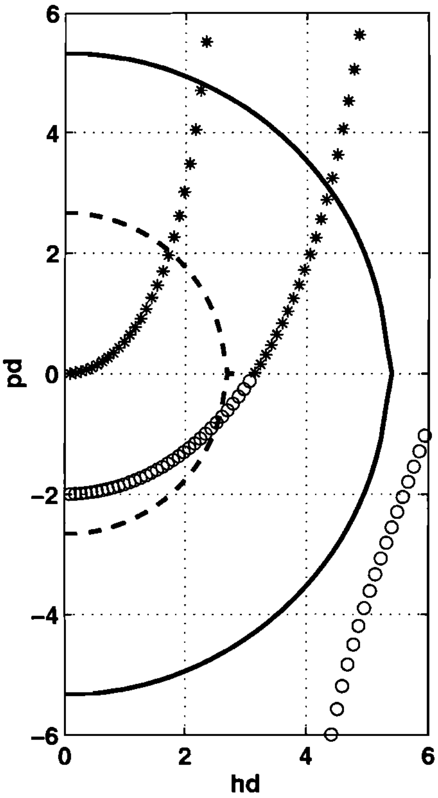

Figure 3.11: graphical solution of the *TE* roots of $\mathrm{den}\left[A_n(k_\rho, z)\right]$, where the dashed line corresponds to $d = 0.15\lambda_0$ and the solid one to $d = 0.3\lambda_0$.

$$\left.\begin{aligned} pd &= \frac{\varepsilon_{r_2}}{\varepsilon_{r_1}}\left[-hd\cot(hd) \pm \sqrt{(hd)^2[\cot^2(hd)+1]}\right] \\ (hd)^2+(pd)^2 &= (k_2d)^2\left[\left(\frac{k_1}{k_2}\right)^2 - 1\right] \end{aligned}\right\} \text{TM modes,} \tag{3.23}$$

$$\left.\begin{aligned} pd &= -hd\cot(hd) \pm \sqrt{(hd)^2[\cot^2(hd)+1]} \\ (hd)^2+(pd)^2 &= (k_2d)^2\left[\left(\frac{k_1}{k_2}\right)^2 - 1\right] \end{aligned}\right\} \text{TE modes.} \tag{3.24}$$

Both equations of Equation (3.23) are plotted in Figure 3.10. The asterisk ($*$) and circle (o) lines represent the first equation. The circle line corresponds to the definition of pd with a plus sign, where the asterisk line denotes the minus sign. The dashed line represents the second equation with $d = 0.15\lambda_0$, which is a circle. For the TE modes of Equation (3.24), a similar plot is made in Figure 3.11. The poles, which are located at the intersections of these lines, can then be retrieved with the aid of Equation (3.22). However, not all intersections represent surface-wave poles. From Equation (3.22), it follows that if $p < 0$, the poles are located on the lower Riemann sheet and thus do not contribute to the integral. These poles are the so-called *improper modes.* Hence, the only surface-wave modes are located in the region where $p > 0$. These modes correspond to the poles in Figure 3.9.

Note that the first mode is always a TE mode if the slab(s) is terminated by two half-spaces. This can be verified if we insert the numerator in Equation (3.21), i.e.,

$$\mathrm{num}\big[A_n(k_\rho, z, z')\big] = Z_{p,1} Z_{p,2}\big[Z_{p,3} + jZ_1 \tan(k_{z,1} d)\big]. \tag{3.25}$$

If we let the slab thickness $d \downarrow 0$ and take $Z_{p,2} = Z_{p,3}$, we obtain the following expression:

$$A_n(k_\rho, z, z') = \frac{Z_3}{2}. \tag{3.26}$$

With the aid of Equation (2.19) and (2.20), we see that the first pole at $k_\rho = k_3$ corresponds to a TE mode, which has no low-frequency cut-off.

Now, let us increase the slab thickness to $d = 0.3\lambda_0$. Then we obtain, with the aid of the Equations (3.23) and (3.24), the solid circles in Figure 3.10 and 3.11. We see that there are now in total four intersections between these solid lines and the asterisk-circle lines, and thus four proper poles. Observe that the asterisk-circle lines are independent of the slab thickness d. The TM surface-wave poles are now given by $k_\rho \approx 1.13k_2$ and $k_\rho \approx 2.54k_2$, and the TE surface-wave poles are given by $k_\rho \approx 1.91k_2$ and $k_\rho \approx 2.75k_2$.

Hence, if we increase the thickness of the slab, the circles in Figure 3.10 and 3.11 get a larger radius and thus more surface-wave modes will exist inside the slab. Consequently, if we increase the frequency, so λ_0 decreases, we obtain more surface-wave modes as well.

In the configuration of Figure 3.8, a dielectric layer was terminated by two half spaces. If we replace one half space by a perfectly conducting ground plane, these surface-wave singularities also occur. For these geometries, the first mode is always TM, since it has no low-frequency cut-off, as can be verified with Equation (3.11) by letting the slab thickness $d \downarrow 0$. Other configurations, like surface waves along a plane impedance surface or along a corrugated plane, are beyond the scope of this report. Details about these configurations can be found in [5].

In Section 3.2, we have mentioned that the branch cuts represent the radiation modes, i.e. the modes present in the half space. This can be verified with the aid of surface-wave modes [3, p. 330-333]. Therefore, let us assume that we have a dielectric stratified structure, which is terminated on both sides by a perfectly conducting ground plane. The upper ground plane is located at a height z_{upper} and the lower one at a height z_{lower}. This means that we only have surface-wave modes and no branch cuts, as discussed in Section 3.1.3. If we increase the distance z_{upper} to simulate a half space, the modes present in the region below z_{upper} increase as well and are distributed exactly on the branch cuts, as encountered in Section 3.2. This implies indeed that the branch cuts correspond to the radiation modes.

3.4.2 Leaky waves along a dielectric slab

All surface-wave poles of the functions $A_n(k_\rho, z, z')$ are located on the real k_ρ-axis in the range of Equation (3.20) for lossless media, if we have at least one half space, as we have discussed in Section 3.4.1. We have discovered that the number of these surface-wave poles inside a dielectric slab depends on the thickness of the slab, and consequently the frequency. The thicker the slab or the higher the frequency, the more poles are found. Therefore, as the frequency gradually lowers, some of the poles must get a value lower than $k_{low} = \max(k_{half\ spaces})$. However, these poles cannot pass the branch point at k_{low} and continue on the real axis, due to the presence of the branch cut. But, since the real part of the term under the square root of $k_{z,low}$ becomes negative now, zeros of Equation (3.21) can only be found, if k_ρ has an imaginary part. This means that we have to pass through the branch cut and go to the lower Riemann sheet. This negative imaginary part indicates that these pole corresponds to modes that 'leak' energy into the half space with wavenumber k_{low}. Therefore, they are called *leaky-wave modes.* Physically, this can be interpreted as shown in Figure 3.12, where 'rays' are radiating in the less dense medium and become weaker as ρ increases.

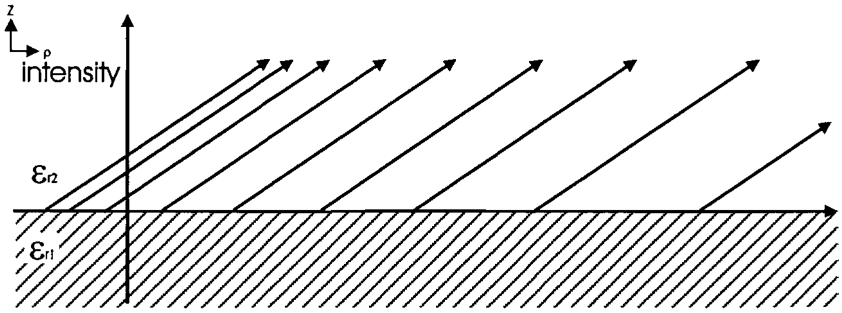

Figure 3.12: intensity pattern of the leaky waves. Closer lines correspond to a higher intensity. The field intensity increases with z and decreases along the propagation direction ρ.

Note, that if we fix ρ to observe the field behavior along the transmission line, an exponential growth is seen in this direction. This implies that these poles are indeed located on the lower Riemann sheet, where $\mathrm{Im}(k_{z,low}) > 0$.

The location of a leaky-wave pole, is graphically much harder to obtain than the one of a surface-wave pole, due to the inclusion of an imaginary part. In Section 4.1.1, a procedure is presented, which computes the locations of the surface- and leaky-wave poles numerically.

3.5 Final composition of the k_ρ-plane

In the previous sections of this chapter, we have encountered several properties of the k_ρ-plane. Now, let us combine all these properties to obtain a final composition of the k_ρ-plane. Therefore, let us consider a structure with two different half spaces, and thus two radiation modes k_1 and k_2 separated by a dielectric layer with wavenumber k_3, where $k_3 > k_1 > k_2$. A possible composition of the k_ρ-plane is shown in Figure 3.13.

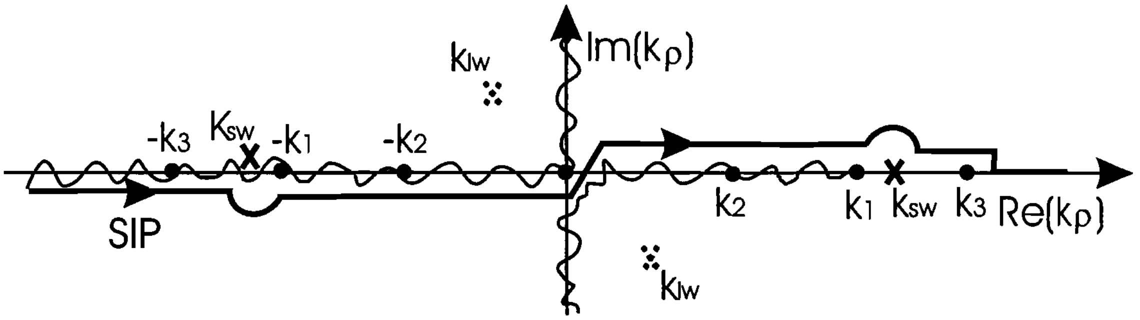

Figure 3.13: topology op the k_ρ-plane with branch points, branch cuts, surface- and leaky-wave poles and the SIP.

The leaky-wave poles are dashed to indicate that they are located on the lower Riemann sheet. The surface-wave poles as well as the Sommerfeld Integration Path (SIP) are solid to denote that they are located on the upper Riemann sheet. Since integration in the vicinity of a singularity takes longer, as we will discuss in Section 4.1, the integration path is slightly deformed in Figure 3.13 to avoid the influence of these singularities.

Since we have two half spaces containing different media, four branch cuts are located in the k_ρ-plane. The branch cuts with branch points at $k_\rho = \pm k_1$ are due to the square root of $k_{z,1}$ and the branch cuts with branch points at $k_\rho = \pm k_2$ are due to the wavenumber $k_{z,2}$. Their upper and lower Riemann sheets are distinguished by Equation (3.19) with $i = 1$ and $i = 2$, respectively. More branch cuts can never occur in the k_ρ-plane, since we cannot have more than two half spaces, as we have seen in Figure 2.6.

Chapter 4

Asymptotic evaluation of the integrals I_n

In Section 3.3, we already encountered the Sommerfeld Integration Path (SIP) as a replacement of the integration path along the real k_ρ-axis, due to the presence of branch cuts and surface-wave singularities there. The computation of these integrals along this path is a difficult task because of the in general oscillatory and slowly convergent behavior of the integrands and the occurrence of singularities near the path, as we will discuss in Section 4.1. However, it is of great importance that their computation is performed *efficiently*, since in order to compute the fields these integrals should be repeatedly evaluated. To speed up the convergency, we will use the *Method of Steepest Descent.*

The procedure for the Method of Steepest Descent requires that the SIP is *deformed* to the so-called Path of Steepest Descent. We will see in Section 4.2, that this is the "fastest" path through the k_ρ-plane, since it passes through the *saddle point* and the integrand decays exponentially at a maximum rate away from this saddle point. However, the location of this integration path differs for every angle ψ, where ψ is given by Figure 2.1. Therefore, we first need a better understanding of the possibilities of deforming the SIP to other integration paths in the complex k_ρ-plane, since branch cuts, branch points and singularities are present in this plane as well. This will be discussed in Section 4.1. Finally, the far-field approximations of the integrals I_n, which are the leading-order approximations of the Method of Steepest Descent, will be presented in Section 4.3.

4.1 Possible contour deformations of the SIP

In Section 3.3, we have presented the Sommerfeld Integration Path (SIP). We have seen that this integration path is located on the upper Riemann sheet and therefore meets the radiation condition, since $\mathrm{Im}(k_{z,i}) \leq 0$. This means that exponential decay is ensured on this sheet as long as $|z - z'| > 0$, since then the exponential $e^{-jk_{z,i}|z - z'|}$, present in the Transmission-Line Green's functions (TLGF's), decays exponentially.

The Hankel function, on the other hand, can be approximated for large arguments by [6, p. 467]

$$H_{\mu}^{(2)}(k_\rho \rho) \sim \sqrt{\frac{2}{\pi k_\rho \rho}} e^{-j(k_\rho \rho - \mu\pi/2 - \pi/4)}. \tag{4.1}$$

For this function, exponential decay is ensured in the lower k_ρ-plane if $\rho > 0$, owing to the exponential $C(k_\rho \rho)e^{-jk_\rho \rho}$. Then, Jordan's lemma [5], allows us to close the SIP in the lower k_ρ-plane, which is shown in Figure 4.1, since there the integrand decays to zero. Note, that if we had not replaced the Bessel function by the Hankel function in Section 2.2.1, the integration path could not have been closed, since it had to start at the origin and consequently Jordan's lemma could not have been applied. The surface- and leaky-wave poles are excluded for the moment, and two branch points located at $k_\rho = \pm k_1$ are assumed. This is for example the case if we have a half space with wavenumber k_1 terminated by a ground plane, which corresponds to selection 11 of Figure 2.6. Since the integration path

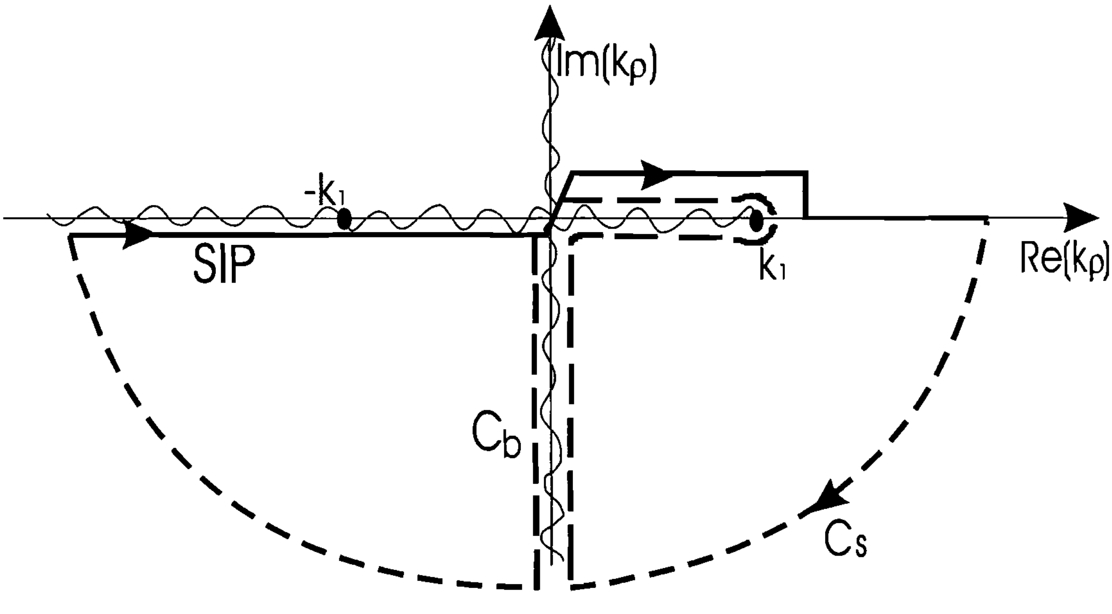

Figure 4.1: closed integration path, SIP and C, over infinity.

at infinity cannot cross the branch cut, the contour must return from infinity, encircle the branch point at k_1 and recede out to infinity again along the other side of the branch cut. This contour is shown in Figure 4.1 where C_s denotes the semicircle over infinity and C_b the branch-cut integral.

Now, let us apply *Cauchy's integral theorem*, i.e., [11]

$$\oint f(z)dz = 0, \tag{4.2}$$

where $f(z)$ is an analytic function on a simply connected region. We speak of a simply connected region if any simple closed curve can be shrunk to a point continuously in the set. This means that as long as there are no 'holes' in a region, i.e. no singularities, the closed integral equals zero. Since we assumed that there are no surface- and leaky-wave singularities inside the contour, we can state that

$$\oint f(z)dz = \int\limits_{SIP} + \int\limits_{C_s} + \int\limits_{C_b} = 0, \tag{4.3}$$

which means that the original integration path along the SIP can be replaced by

$$\int\limits_{SIP} = -\int\limits_{C_s} - \int\limits_{C_b} . \tag{4.4}$$

The integral along the contour C_s vanishes too, owing to Jordan's lemma. This implies that the integral along the SIP is solved for structures of selection 11, if we know the branch-cut contribution.

Now, let us introduce a surface- and leaky-wave singularity located at $k_\rho = k_{sw}$ and $k_\rho = k_{lw}$. This means that we have added a slab to the structure, for example like the structure of selection 13 in Figure 2.6. The wavenumber of the slab is k_1 and the one of the half space is k_2, where $k_1 > k_2$. According to Cauchy's integral theorem of Equation (4.2), no singularities may be encountered in the closed contour and therefore the integration path needs to go around them as well. A possible contour deformation is shown in Figure 4.2, which we will call the *First-Contour Deformation* (FCD).

Observe that it does not matter where the surface-wave singularities are located between k_1 and k_2, since this path does not recede to $-j\infty$ till after k_2. Also the locations of the leaky-wave singularities on the lower Riemann sheet are unimportant, since the total integration path is located on the upper Riemann sheet. Hence, **no** information regarding the locations of the singularities is needed if we integrate along this path.

In Equation (4.1), we have seen that the Hankel function has an $e^{-jk_\rho \rho}$ behavior for large arguments. This implies that if $|\mathrm{Re}(k_\rho)| \rightarrow \infty$, errors can occur in the numerical result, due

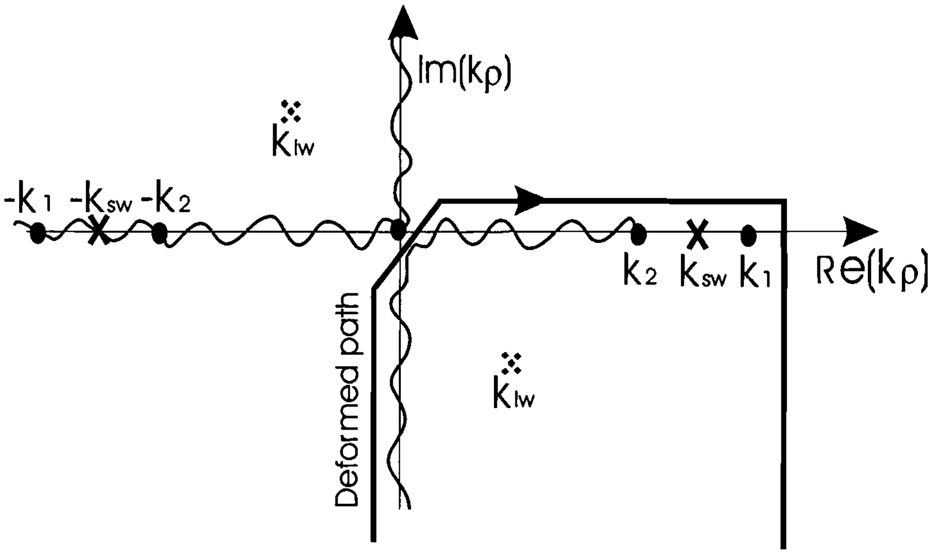

Figure 4.2: a contour deformation of the SIP to the FCD by using Cauchy's integral theorem.

to the rapid oscillations of this function, as we will see in Section 5.1.1. In Figure 4.2, we notice that these oscillating tails of the SIP do not have to be computed for this integration path. However, since also the distance ρ is present in the argument of the Hankel function, errors can still occur if ρ gets large. For small ρ, on the other hand, the Hankel function in the integrand decays more slowly along the integration paths that come and go to $-j\infty$.

Since we are allowed to deform the integration path as long as no singularities are encountered, we can also deform the integration path into the first quadrant to avoid the influence of the surface-wave poles on the real k_ρ-axis. However, the exponential $e^{-jk_\rho \rho}$, present in the Hankel function, diverges in the first quadrant, as can be seen in Figure 3.1. This implies that more integration points are needed, the further we get into this quadrant. Consequently, the total computation time of the integrand increases. This implies that there is an optimal distance $\mathrm{Im}(k_\rho)\rho$ for our integration path, which avoids most of the influence of the singularities, but on the other hand is not located unnecessarily far into the first quadrant.

To visualize the influence of the surface-wave singularities on the integrand, let us assume that we have a configuration like selection 13 of Figure 2.6. The slab has a thickness of $d_1 = 0.74\lambda_0$, a relative permittivity of $\varepsilon_{r,1} = 9$ and a wavenumber k_1. The half space above is filled with air, i.e. $\varepsilon_{r,2} = 1$, and corresponds to the branch points at $k_\rho = \pm k_2$. The real part of the integrand of I_1 along the FCD path is shown in Figure 4.3 for $\mathrm{Im}(k_\rho)\rho = 0.5\lambda_0$, which is the experimentally obtained optimal distance. In the range of Equation (3.20), we find one surface-wave pole at $k_\rho \approx 1.33k_2$, which causes amplitude variations in the

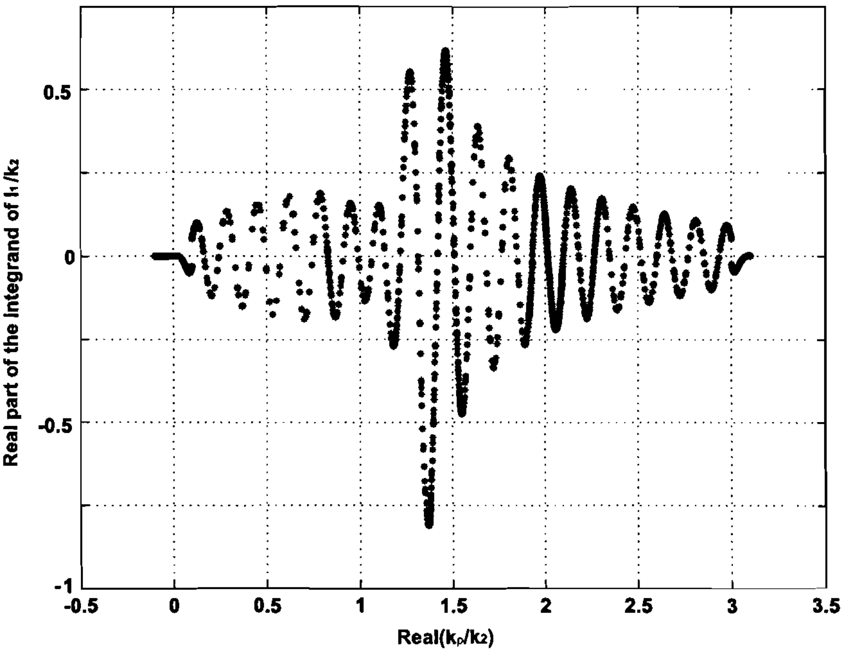

Figure 4.3: influence of a surface-wave pole located at $k_\rho \approx 1.33k_1$ on the real part of the integrand of I_1 for $\text{Im}(k_\rho)\rho = 0.5\lambda_0$.

real part of the integrand. So, if the amount of surface-wave poles located in the region $k_2 - k_1$ increases, and we use the same integration path, the variations in the integrand will become more intense as well and, consequently, the computation of the integrand will take longer. Beyond wavenumber $k_1 = \sqrt{\varepsilon_{r,1}}k_2 = 3k_2$, the integration path returns to $3k_2 - j\infty$ and decays exponentially with $\exp\left(\text{Im}(k_\rho)\rho\right)$.

Now, let us have a look at the contour deformation of Figure 4.4. Also this closed integration path has no singularities inside its contour, since it travels around the surface-wave singularity at $k_\rho = k_{sw}$, and is still analytic since it does not cross the branch cut. Therefore, we can still use Cauchy's integral theorem. Since the contribution of the path towards this singularity is the same as the one returning from it, they cancel each other. The contribution of a singularity is called a **residue**. Hence, the integration along the SIP is equal to

$$\int_{SIP} = -\int_{C_d} -2\pi j \sum \text{Residues from surface-wave singularities.} \qquad (4.5)$$

which follows directly from *Cauchy's residue theorem* [4].

Theorem. *Let C be a negatively oriented simple closed contour within and on which a function f is analytic except for a finite number of singular points $z_1, z_2, ..., z_n$ interior to C. If $B_1, B_2, ..., B_n$ denote the residues of f at those*

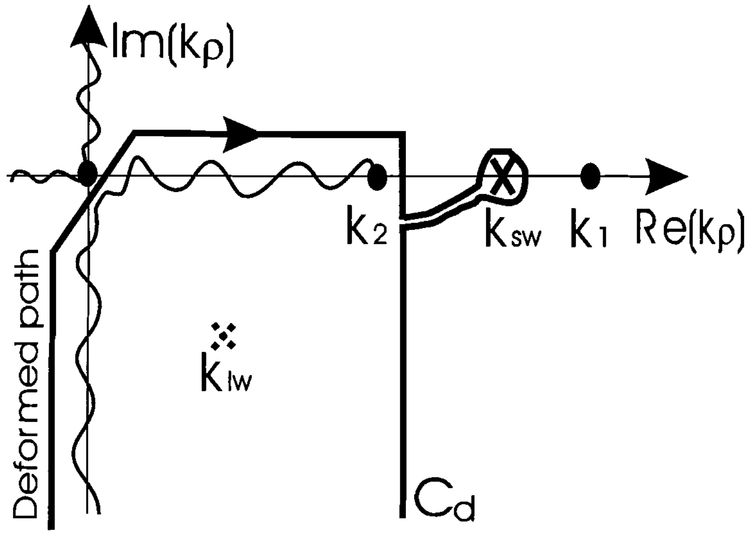

Figure 4.4: a contour deformation of the SIP to the integration path C_d and a path which encircles the surface-wave singularity at $k_\rho = k_{sw}$.

points then

$$\oint_C f(z)dz = -2\pi j\Big(B_1 + B_2 + ... + B_n\Big). \tag{4.6}$$

We observe that the integration path in Figure 4.4 avoids the influence of the surface-wave poles in the first quadrant, as long as they are not too close to the branch point, where the path recedes to $k_2 - j\infty$. However, to compute the residues of these surface-wave singularities accurately, their locations on the k_ρ-axis have to be determined accurately as well, as we will see in Section 4.1.2. A numerical routine that locates the poles will be discussed in Section 4.1.1.

As we introduced the branch cuts in Section 3.2, we discussed the fact that continuity of the complex square root function is guaranteed when passing through a branch cut if we move onto another Riemann sheet. This is shown in the deformation of Figure 4.5, where part of the integration path C_{bp} has passed through the branch cut and therefore is located on the lower Riemann sheet. This part is denoted by the dashed line. We also see that the residues of the encountered leaky-wave poles, located on the lower Riemann sheet, have to be computed as well. Also here the numerical search process of Section 4.1.1 will be used to locate the position of the poles. Note that this integration path starts on the lower Riemann sheet at $k_1 - j\infty$ where $\text{Im}(k_{z,i}) > 0$. However, since the distance $|z - z'| = 0$, the exponential $e^{-jk_{z,i}|z\,-\,z'|}$ equals one and the integrand still becomes exponentially small, owing to the exponential decay of the Hankel function in the lower k_ρ-plane.

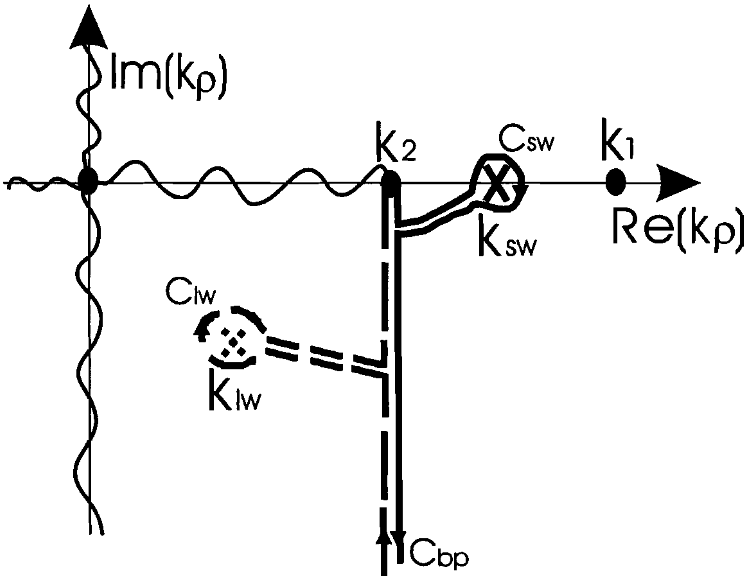

Figure 4.5: deformation of the SIP to the integration path C_{bp} and paths that encircle all encountered surface- and leaky-wave poles.

Hence, we have seen several deformations of the SIP in the complex k_ρ-plane, and are able to deform the integration path to any contour we like, as long as we add the residues of the encountered surface- and leaky-wave singularities and move onto another Riemann sheet if we pass through a branch cut. To meet the radiation condition the start and end points of the integration path at infinity should be located on the upper Riemann sheet if $|z - z'| > 0$.

4.1.1 Numerical calculation of the pole locations

In Section 3.4.1 and 3.4.2, we have discussed the locations of the surface- and leaky-wave singularities in the complex k_ρ-plane. We have seen that the surface-wave pole locations can be obtained graphically. The locations of the leaky-wave poles, on the other hand, are much harder to obtain this way.

In [20, p. 77], a general numerical method to locate all poles in the k_ρ-plane is discussed. This is achieved by placing a grid over those parts of the first and fourth quadrant where we wish to search for poles, as shown in Figure 4.6. The dashed grid indicates that it is located on the lower Riemann sheet. This is where we will search for leaky-wave poles. The solid grid, on the other hand, is placed on the upper Riemann sheet, where the surface-wave poles are located. It is possible to locate surface- and leaky-wave poles using the argument principle [4]

$$N - P = \frac{1}{2\pi j} \oint\limits_C \frac{f'(z)}{f(z)} dz = \frac{\Delta_C}{2\pi} \left[\arg f(z)\right], \tag{4.7}$$

where N is the number of complex roots of $f(z)$ in a closed contour C and P the number of poles in C. The term $\Delta_C \arg f(z)$ represents the change in the argument of $f(z)$ as C is traversed counterclockwise a single time. The function $f(z)$ is given by the denominator of the functions $A_n(k_\rho, z, z')$ and thus the zeros of these functions have to be found. By taking points on every rectangle in the grid, this closed contour C for each rectangle is created. For every pole that is present in such a closed contour, we get a phase difference of -2π, and for every zero, a phase difference of $+2\pi$. This way, we are able to obtain the amount of zeros minus poles in a certain rectangle. However, if there is an equal amount of poles and zeros inside a certain contour, Equation (2.70) always gives zero. To overcome this problem, we determine the zeros by

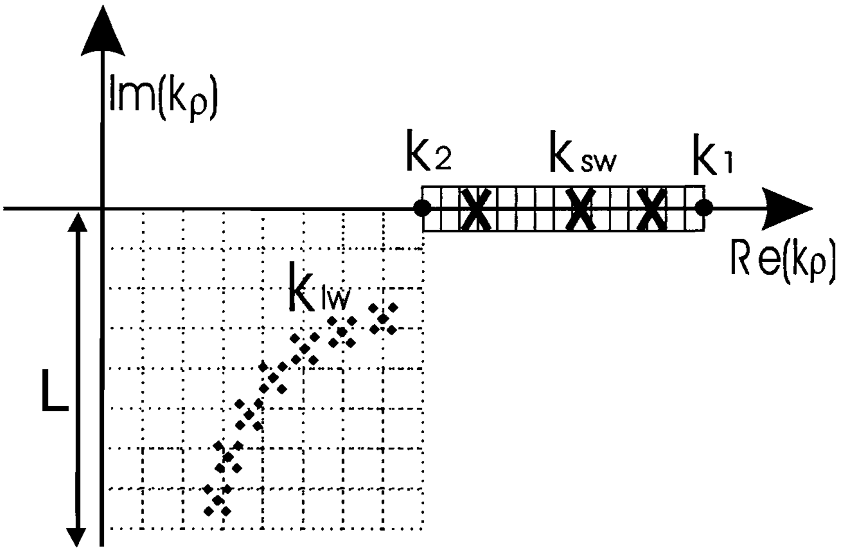

Figure 4.6: grids to find the surface- and leaky-wave poles in the k_ρ-plane.

$$\frac{1}{2\pi j} \oint\limits_C k_\rho^n \frac{f'(k_\rho)}{f(k_\rho)} dk_\rho = k_{\rho,P}^n - k_{\rho,N}^n, \tag{4.8}$$

where $n = 0, 1, 2, ...$ The position of the pole is denoted by $k_{\rho,P}$, and the one of the zero by $k_{\rho,N}$. For $n = 0$, we obtain Equation (4.7), and thus zero in case of a similar amount of poles and zeros. However, for $n = 1$, the right hand side of Equation (4.8), does not equal zero anymore, since the locations of the poles and zeros in the complex k_ρ-plane differ. So, with this search routine it is possible to find all zeros of the function $f(k_\rho) = \mathrm{den}[A_n(k_\rho, z, z')]$ in a given search area. However, if we want to determine their location accurately, a considerable amount of computation time is consumed, due to the large number of function values needed in the evaluation of the contour integral C. Therefore, we only *estimate* the location of the poles and use Muller's method [11], to obtain more accurate pole locations.

The time needed to find the zeros of the denominator of the functions $A_n(k_\rho, z, z')$ is much less than the time needed to find its poles, as will be shown in Section 5.1.3. This is the reason why we have solved the transmission-line equations for **each** possible configuration by hand (cf. Section 2.3), and not a general procedure is applied as, for example, the one suggested by [3], since now this denominator follows explicitly. In Appendix A, another way to determine the zeros of the functions $A_n(k_\rho, z, z')$ for *arbitrary* structures is shown.

4.1.2 The residue of a surface- and leaky-wave singularity

Cauchy's residue theorem of Equation (4.6) makes it possible to add the residues B_k of the singular points z_k, for $k = 1, 2, ..., n$. According to [4, p. 176], the residue of a simple pole is given by

$$B_k = \text{Res} f(z) = \lim_{z \to \alpha} [(z - \alpha) f(z)], \tag{4.9}$$

where $f(z)$ is a function, which has a simple pole in $z = \alpha$.

Now, let us recall the integral I_1 of Equation (2.70a). The poles of the function $A_1(k_\rho, z, z')$ are assumed to be known and defined as $k_\rho = k_{sw}$ and $k_\rho = k_{lw}$ for surface- and leaky-wave poles, respectively. If we assume for the moment that there is only one simple (surface-wave) pole, then the residue of this pole follows from Equation (4.6) and (4.9) as

$$\oint_{C_{\text{sw}}} f(z') dz' = -2\pi j \lim_{k_\rho \to k_{sw}} \left[(k_\rho - k_{sw}) A_1(k_\rho, z, z') H_0^{(2)}(k_\rho \rho) k_\rho \right], \tag{4.10}$$

where the minus sign indicates that the surface-wave pole is encircled in a negative sense over a contour C_{sw}, as can be seen in Figure 4.4. Note that the accuracy of the residue strongly depends on the accuracy of the pole location. To achieve a high accuracy, we used Muller's method in Section 4.1.1. Similar expressions are obtained for the residues of a simple pole for the other integrals of Equation (2.70).

4.2 Steepest-Descent Path (SDP)

The Method of Steepest Descent consist of deforming the integration path along the Sommerfeld Integration Path (SIP) to the Steepest-Descent Path (SDP), along which we have maximum exponential decrease of the integrand [6, p. 370-382]. This implies that the computation of the integrals is performed in a very *efficient* way along this path. Since the SDP changes for different angles ψ (cf. Section 4.2.1), where ψ is, with the aid of Figure 2.1, given by

$$\cos\psi = \frac{\rho}{r} = \frac{\rho}{\sqrt{\rho^2 + (z - z')^2}}, \tag{4.11}$$

to ensure that we indeed have this maximum exponential decay, the presented contour deformations in Section 4.1 are of great use.

To obtain this path, we recall the integral I_1 of Equation (2.70), i.e.,

$$I_1(k_\rho, \rho, z, z') = \int_{-\infty}^{\infty} A_1(k_\rho, z, z') H_0^{(2)}(k_\rho \rho) k_\rho dk_\rho. \tag{4.12}$$

If we substitute the approximation of the Hankel function for *large arguments* of Equation (4.1) in (4.12) and extract the oscillating exponential $e^{-jk_{z,2}|z - z'|}$ out of the function $A_1(k_\rho, z, z')$, we obtain

$$I_1 = \int_{SIP} B_1(k_\rho, z, z') \sqrt{\frac{2}{\pi k_\rho \rho}} e^{-j(k_\rho \rho - \pi/4)} e^{-jk_{z,2}|z - z'|} k_\rho dk_\rho, \tag{4.13}$$

in which we have assumed that k_2 is the wavenumber of a half space, and where

$$B_1(k_\rho, z, z') = A_1(k_\rho, z, z') e^{jk_{z,2}|z - z'|}, \tag{4.14}$$

is a smoothly varying function. Further, we have replaced the integration limits of Equation (4.12) by the Sommerfeld Integration Path of Figure 3.13. Then the exponential of the integrand of Equation (4.13) is explicitly given by

$$e^{q(k_\rho, \rho, z, z')} = e^{-j\left(k_\rho \rho - j\sqrt{-k_2^2 + k_\rho^2}|z - z'|\right)}, \tag{4.15}$$

where we used Equation (3.6), with $i = 2$. Now, let us assume that at a certain point $k_{\rho\ \mathrm{sp}}$ on the integration path, $\mathrm{Re}\left[q(k_\rho, \rho, z, z')\right]$ has a maximum value so that $\mathrm{Re}\left[q(k_\rho, \rho, z, z')\right] < \mathrm{Re}\left[q(k_{\rho\ \mathrm{sp}}, \rho, z, z')\right]$ on the remainder of the path. This means that also the exponential of Equation (4.15) has it maximum value at $k_{\rho\ \mathrm{sp}}$ and decreases exponentially away from this point. The maximum contribution to the integral I_1 is therefore located in the vicinity of the point $k_{\rho\ \mathrm{sp}}$, which is called a *stationary phase point* or *saddle point.* Hence, we have to find this point and make sure that the rate of change along the remainder of the path is maximal, to obtain maximal exponential decay. Since it is hard to distinguish between the real and imaginary part of $q(k_\rho, \rho, z, z')$, which is necessary if we want to calculate the rate of change, we will apply a transformation from the k_ρ-domain to the α-domain.

4.2.1 Transformation to the α-domain

Let us assume that we are dealing with a configuration of selection 13 in Figure 2.6. Then we have branch points at $k_\rho = \pm k_2$, corresponding to the half space. Further, we assume that $k_2 < k_1$, where k_1 is the wavenumber of the slab. Then, let us introduce the following transformation [6, p. 370-382]:

$$k_\rho = k_2 \cos\alpha, \tag{4.16}$$

where α is a complex number. Owing to this transformation, the wavenumber $k_{z,2}$, given by Equation (2.57) with $i = 2$, becomes

$$\begin{aligned} k_{z,2} &= \sqrt{k_2^2 - k_\rho^2} \\ &= \sqrt{k_2^2 - (k_2\cos\alpha)^2} \\ \Rightarrow k_{z,2} &= +k_2 \sin\alpha. \end{aligned} \tag{4.17}$$

With $k_{z,2}(k_\rho = 0) = k_2$, the plus sign is chosen to make the point $k_\rho = 0$ correspond to $\alpha = \pi/2$. This implies that the wavenumber $k_{z,2}$ introduces no branch cuts in the α-plane. Also the wavenumber $k_{z,1}$ introduces no branch cuts, as explained in Section 3.1.3, and therefore the only branch cut in the α-plane corresponds to the one of the Hankel function.

Note, that when applying the transformation to the α-domain, we have to use the arccos function, since from Equation (4.16) follows that

$$\alpha = \arccos\left(\frac{k_\rho}{k_2}\right). \tag{4.18}$$

This function has branch points in $k_\rho = \pm k_2$. Its branch cuts are located on the real k_ρ-axis from $-\infty$ to $-k_2$ and from k_2 to ∞, the same as for the arcsin function, which is discussed in Appendix B.

In Figure 4.7, we plotted the α-plane. Since the cosine is a periodic function, also the α-plane is periodic, as can be seen from the quadrant transformation. To transform the upper and lower Riemann sheet as well, we have to determine the $\text{Im}(k_z)$ first, i.e.,

$$\begin{aligned} \text{Im}(k_{z,2}) &= \text{Im}\big(k_2 \sin\alpha\big) \\ &= k_2 \cos\alpha_r \sinh\alpha_i, \end{aligned} \tag{4.19}$$

where we have used Equation (4.17) and

$$\alpha = \alpha_r + j\alpha_i. \tag{4.20}$$

Then the upper Riemann sheet, where $\text{Im}(k_z) < 0$, is indicated by the horizontal lines in Figure 4.7, and the lower Riemann sheet, where $\text{Im}(k_z) > 0$, by the vertical lines. We

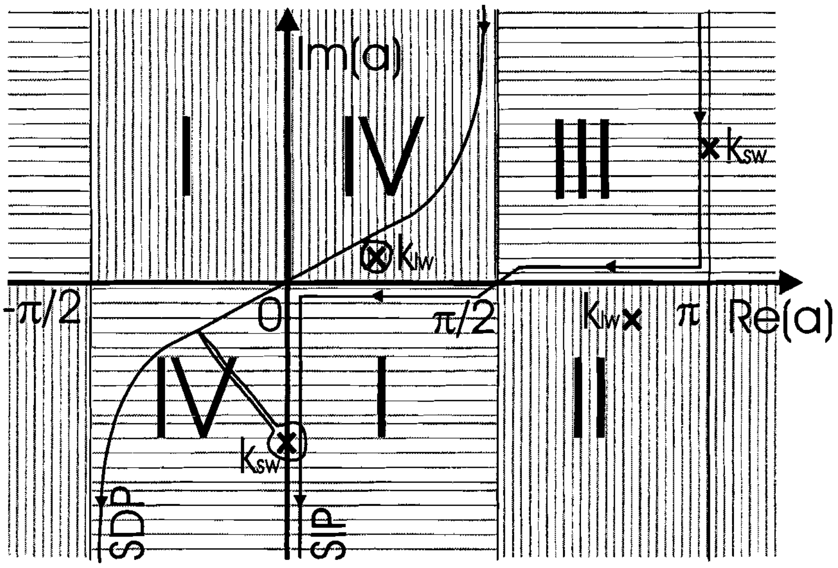

Figure 4.7: the α-plane with SIP, surface- and leaky-wave poles. The four quadrants of the k_ρ-plane are after transformation denoted by I, II, III, IV, respectively. The transformed upper and lower Riemann sheet are indicated by horizontal and vertical lines, respectively.

observe that the Riemann sheets in the k_ρ-plane appear as adjacent regions in the α-plane. The transformed locations of the SIP, and the surface- and leaky-wave singularities are added as well.

Now, let us apply the transformation to the α-plane, given by Equation (4.16), to the integral I_1 of Equation (4.13), i.e.,

$$\begin{aligned} I_1 &= e^{j\pi/4} \int\limits_{SIP} B_1(k_\rho, z, z') \sqrt{\frac{2}{\pi k_\rho \rho}} e^{-j\left(k_\rho \rho + k_{z,2}|z-z'|\right)} k_\rho dk_\rho \\ &= -e^{j\pi/4} \int\limits_{SIP} B_1(\alpha, z, z') \sqrt{\frac{2}{\pi k_2 \rho \cos\alpha}} e^{-jk_2\left(\rho\cos\alpha + |z-z'|\sin\alpha\right)} k_2^2 \cos\alpha \sin\alpha d\alpha. \end{aligned} \tag{4.21}$$

According to the configuration of Figure 2.1, we can introduce

$$\rho = r\cos\psi, \tag{4.22a}$$

$$|z-z'| = r\sin\psi. \tag{4.22b}$$

If we substitute Equation (4.22) in Equation (4.21), we obtain

$$I_1 = \int\limits_{SIP} f(\alpha) e^{-jk_2 r\cos(\alpha-\psi)} d\alpha, \tag{4.23}$$

with

$$f(\alpha) = -e^{j\pi/4} B_1(\alpha, z, z') \sqrt{\frac{2k_2 \cos\alpha}{\pi r \cos\psi}} k_2 \sin\alpha. \tag{4.24}$$

Let us have a closer look at the exponential of Equation (4.23). Since α is complex, the cosine term of the exponential is given by

$$\begin{aligned} \cos(\alpha - \psi) &= \frac{e^{j(\alpha-\psi)} + e^{-j(\alpha-\psi)}}{2} \\ &= \frac{e^{j(\alpha_r - \psi + j\alpha_i)} + e^{-j(\alpha_r - \psi + j\alpha_i)}}{2} \\ &= \cos(\alpha_r - \psi)\cosh(\alpha_i) - j\sin(\alpha_r - \psi)\sinh(\alpha_i), \end{aligned} \tag{4.25}$$

where we have used Equation (4.20). Then the exponential of Equation (4.23) is rewritten as

$$\begin{aligned} \exp[q(\alpha,\psi)] &= \exp[-jk_2 r\cos(\alpha - \psi)] \\ &= \exp\left\{-jk_2 r\Big[\cos(\alpha_r - \psi)\cosh(\alpha_i) - j\sin(\alpha_r - \psi)\sinh(\alpha_i)\Big]\right\} \\ &= \exp\{-jk_2 r\cos(\alpha_r - \psi)\cosh(\alpha_i) - k_2 r\sin(\alpha_r - \psi)\sinh(\alpha_i)\}. \end{aligned} \tag{4.26}$$

In this exponential, the real and imaginary part of the phase function $q(\alpha, \psi)$ are separated explicitly, which was not the case in Equation (4.15). Hence, the transformation to the α-domain has proven successful and the SDP can be determined. First, we will locate the saddle point, where the exponential of Equation (4.26) has its maximum value, as discussed in Section 4.2. The saddle point is located at those points where

$$\frac{\partial q(\alpha,\psi)}{\partial \alpha_r} = \frac{\partial q(\alpha,\psi)}{\partial \alpha_i} = 0, \tag{4.27}$$

which gives

$$\begin{aligned} \frac{\partial q(\alpha,\psi)}{\partial \alpha_r} &= jk_2 r\sin(\alpha_r - \psi)\cosh(\alpha_i) - k_2 r\cos(\alpha_r - \psi)\sinh(\alpha_i) = 0, \\ \frac{\partial q(\alpha,\psi)}{\partial \alpha_i} &= -jk_2 r\cos(\alpha_r - \psi)\sinh(\alpha_i) - k_2 r\sin(\alpha_r - \psi)\cosh(\alpha_i) = 0, \end{aligned} \tag{4.28}$$

and consequently

$$\alpha_r = \psi; \quad \alpha_i = 0. \tag{4.29}$$

This means that the saddle point is located on the real α-axis in the range

$$0 \leq \alpha = \psi \leq \pi/2. \tag{4.30}$$

Now that we have obtained the location of the saddle point, we wish that the integrand decays exponentially at a maximum rate away from this point. Hence, we have to find a

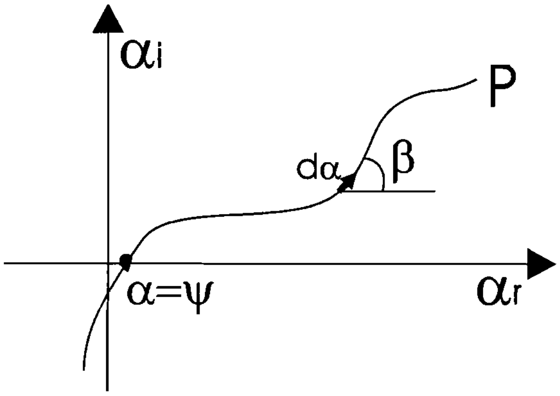

Figure 4.8: possible steepest-Descent Path P in the α-plane.

path P along which the $\mathrm{Re}\big[q(\alpha,\psi)\big]$ decays most rapidly and passes through the saddle point at $\alpha = \psi$, as shown in Figure 4.8. If $d\alpha$ denotes an element of length along the path P, the rate of change of $u(\alpha,\psi) = \mathrm{Re}\big[q(\alpha,\psi)\big]$ along this path is given by

$$\frac{du(\alpha,\psi)}{d\alpha} = \frac{\partial u}{\partial \alpha_r}\frac{d\alpha_r}{d\alpha} + \frac{\partial u}{\partial \alpha_i}\frac{d\alpha_i}{d\alpha} = \frac{\partial u}{\partial \alpha_r}\cos\beta + \frac{\partial u}{\partial \alpha_i}\sin\beta, \tag{4.31}$$

where β is the angle between the element $d\alpha$ and the α_r-axis. Then du/ds has a maximum for

$$\frac{\partial^2 u}{\partial\beta\partial\alpha} = 0 = -\frac{\partial u}{\partial \alpha_r}\sin\beta + \frac{\partial u}{\partial \alpha_i}\cos\beta. \tag{4.32}$$

With the aid of the Cauchy-Riemann Equations [4, p. 41], i.e.,

$$\frac{\partial u}{\partial \alpha_r} = \frac{\partial v}{\partial \alpha_i}, \quad \frac{\partial u}{\partial \alpha_i} = \frac{\partial v}{\partial \alpha_r}, \tag{4.33}$$

where $v(\alpha,\psi) = \mathrm{Im}\big[q(\alpha,\psi)\big]$, we get for Equation (4.32)

$$0 = -\frac{\partial u}{\partial \alpha_i}\frac{d\alpha_i}{d\alpha} - \frac{\partial u}{\partial \alpha_r}\frac{d\alpha_r}{d\alpha} = -\frac{dv}{ds}. \tag{4.34}$$

Hence, $v(\alpha,\psi) = \mathrm{Im}\big[q(\alpha,\psi)\big] =$ *constant*, and thus *not oscillatory* along the path P on which $u(\alpha,\psi) = \mathrm{Re}\big[q(\alpha,\psi)\big]$ changes most rapidly. Since the saddle point, defined by Equation (4.29), is located on this path, $v(\alpha,\psi)$ is in this point, with the aid of Equation (4.26), given by

$$\begin{aligned} v(\alpha,\psi)|_{\alpha=\psi} &= -jk_2 r\cos(\alpha_r - \psi)\cosh(\alpha_i)\,|_{\alpha=\psi} \\ &= -jk_2 r. \end{aligned} \tag{4.35}$$

From Equation (4.35), it follows that the locus of points in the α-plane that verify

$$\cos(\alpha_r - \psi)\cosh(\alpha_i) = 1, \tag{4.36}$$

is the Steepest-Descent Path (SDP), and the integral I_1 of Equation (4.23) is along this path given by

$$I_1 = \int_{SDP} f(\alpha) e^{-jk_2 r - k_2 r \sin(\alpha_r - \psi)\sinh(\alpha_i)} d\alpha. \tag{4.37}$$

In Figure 4.9 and 4.10, the SDP's for the angles $\psi = 0$ and $\psi = \pi/2$ are plotted, respectively. In Figure 4.7, we have chosen for the SDP that starts in the upper left and ends in the lower right, since that is the one that corresponds to the SIP. We observe that if the angle ψ in Figure 2.1 increases, the SDP for $\psi = 0$ moves towards the SDP for $\psi = \pi/2$. This means that the integration path can cross a surface- or leaky-wave singularity for a certain value of ψ. So, we need to determine the angle ψ at which the integration path crosses a singularity, since then we know which residues have to be added to the integral. The residue of a surface-wave pole should be added if [14]

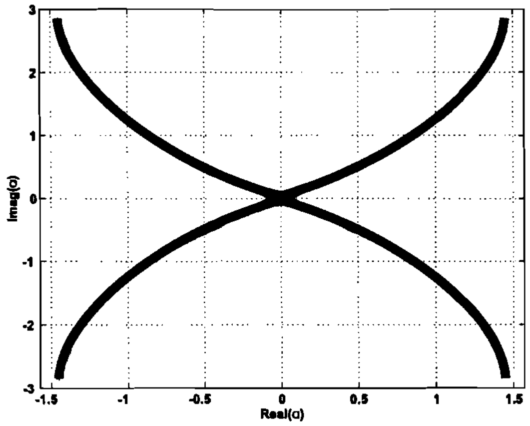

Figure 4.9: possible SDP's for $\psi = 0$ in the α-plane.

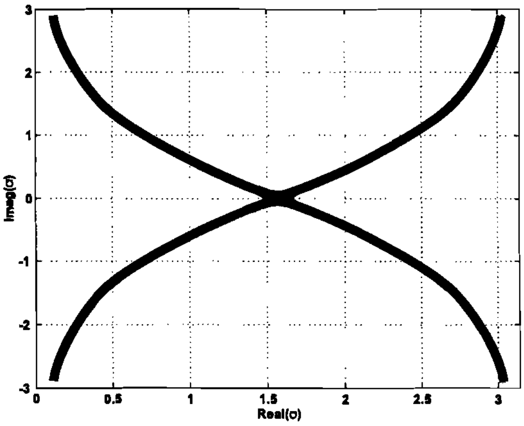

Figure 4.10: possible SDP's for $\psi = \pi/2$ in the α-plane.

$$\begin{aligned} k_{sw} &= k_2 \cos\psi \\ \Rightarrow \psi &< \arccos\left[\frac{k_2}{k_{sw}}\right], \end{aligned} \tag{4.38}$$

where we have used the transformation of Equation (4.16), the fact that k_{sw} is real, and the saddle-point location of Equation (4.29). The contribution of a leaky-wave pole should be added if

$$\begin{aligned} \cos(\alpha_{r,lw} - \psi)\cosh(\alpha_{i,lw}) &= 1 \\ \Rightarrow \psi < \alpha_{r,lw} \pm \arccos&\left[\frac{1}{\cosh(\alpha_{i,lw})}\right] + 2m\pi, \end{aligned} \tag{4.39}$$

where we used the locus of points of Equation (4.36), and where m is an integer.

In case the structure is terminated by two different half spaces with wavenumbers k_1 and k_2 where $k_1 > k_2$, there is always a pair of branch cuts present in the α-plane. The contribution of these branch cuts should then be added too if encountered by the deformed integration path. This is shown in Figure 4.11, where we have performed the transformation to the α-domain on the half space with wavenumber k_2. The SDP crosses the saddle-point in α. The branch cut of the Hankel function, with branch point at $k_\rho = \pi/2$ is plotted as well.

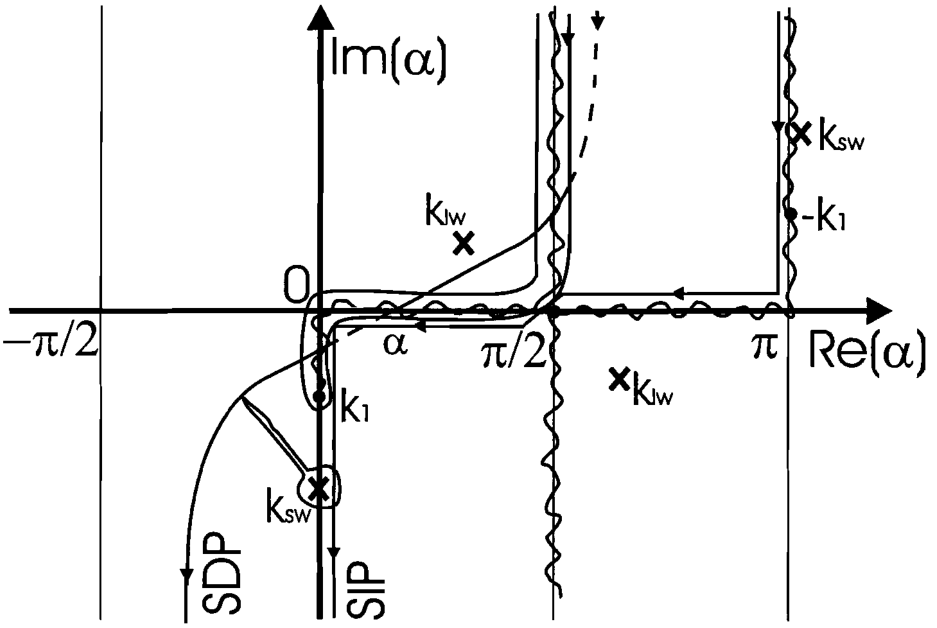

Figure 4.11: the α-plane for a structure terminated by two different half spaces and with inclusion of the branch cut of the Hankel function.

4.2.2 Change of variable to τ

Since the integration limits of the SDP in the α-domain are hard to define exactly, as can be seen in Figure 4.9, we introduce the following change of variable [3, p. 82]

$$\tau^2 = -\sin(\alpha_r - \psi)\sinh(\alpha_i) = \frac{1 - \cos(\alpha - \psi)}{j}, \tag{4.40}$$

which maps the saddle point to the point $\tau = 0$. If we recall the exponential of Equation (4.23) and transform this equation to the τ-domain with the aid of Equation (4.40) and (4.25), we obtain

$$e^{-jk_2 r \cos(\alpha - \psi)} = e^{-jk_2 r - k_2 r \tau^2}. \tag{4.41}$$

For the SDP, defined by Equation (4.36), this change of variable leads to

$$\begin{aligned} \mathrm{Re}\big[\cos(\alpha-\psi)\big] &= \mathrm{Re}\big[1-j\tau^2\big] \\ 1 &= 1+2\tau_i\tau_r \\ \Rightarrow \tau_i &= 0 \text{ or } \ \tau_r = 0, \end{aligned} \tag{4.42}$$

where $\tau = \tau_r + j\tau_i$. With the aid of Equation (4.42), the SDP in the τ-domain is plotted in Figure 4.12. Notice that the integration paths for *all* angles ψ are similar in this domain.

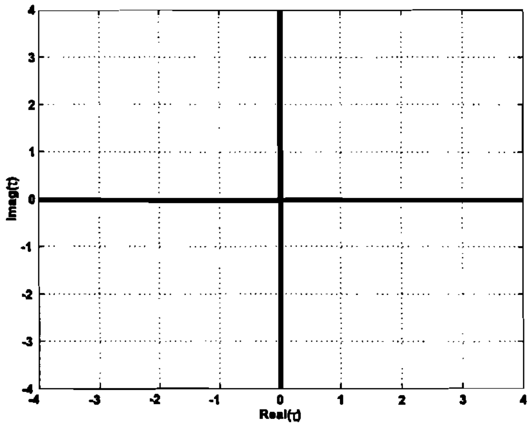

Figure 4.12: the SDP's in the τ-plane are located on the real or imaginary axis, the saddle point is always located in $\tau = 0$.

The SDP with its starting point in the upper right corner and end point in the lower left of Figure 4.9 or 4.10, corresponds to the integration path on the real axis in the τ-plane. When this path is chosen, the integral I_1 of Equation (4.37) becomes

$$I_1 = \int_{-\infty}^{\infty} f(\tau)e^{-jk_2r - k_2r\tau^2}\frac{d\alpha}{d\tau}d\tau. \tag{4.43}$$

The differential $d\alpha/d\tau$, which appeared due to the transformation, is calculated by taking the square root of Equation (4.40), i.e.,

$$\tau = \pm e^{-j\pi/4}\sqrt{2}\sin\left(\frac{\alpha-\psi}{2}\right), \tag{4.44}$$

which gives for the derivative

$$\frac{d\alpha}{d\tau} = \frac{\pm e^{j\pi/4}\sqrt{2}}{\cos\left(\frac{\alpha-\psi}{2}\right)} = \frac{\pm e^{j\pi/4}\sqrt{2}}{\sqrt{1-\sin^2\left(\frac{\alpha-\psi}{2}\right)}} = \frac{\pm e^{j\pi/4}\sqrt{2}}{\sqrt{1-\frac{j\tau^2}{2}}}. \tag{4.45}$$

If we substitute Equation (4.45) in Equation (4.43), we obtain

$$I_1 = \pm e^{j\pi/4}\sqrt{2}e^{-jk_2r}\int_{-\infty}^{\infty} f(\tau)e^{-k_2r\tau^2}\frac{1}{\sqrt{1-\dfrac{j\tau^2}{2}}}d\tau. \tag{4.46}$$

However, the integral is still undefined due to the ±-sign. This problem is solved if we have a closer look at the derivative $d\alpha/d\tau$. Therefore, let us take an arbitrary point on the integration path, for instance the saddle point at $\alpha = \psi$. There, the derivative is given by

$$\frac{d\alpha}{d\tau}(\alpha = \psi) = \pm e^{j\pi/4}\sqrt{2}. \tag{4.47}$$

The '+'-sign implies that

$$\arg(e^{j\pi/4}\sqrt{2}) = \pi/4, \tag{4.48}$$

where the '-'-sign implies that

$$\arg(-e^{j\pi/4}\sqrt{2}) = 5\pi/4. \tag{4.49}$$

Since the SDP moves from the upper right to the lower left corner in Figure 4.7, similar as the SIP, the argument is $5\pi/4$ and thus the minus sign in Equation 4.46 should be used.

4.2.3 The SDP in the k_ρ-domain

Let us return to the k_ρ-domain to obtain some insight in the Steepest-Descent Paths (SDP's) there. The obtained SDP in the τ-domain is transformed back into the k_ρ-domain by taking the inverse of Equation (4.44) and using Equation (4.16). Again we should be cautious, since the inverse of Equation (4.44) has branch cuts originating from the arcsin function, as discussed in Appendix B. Then the integral of Equation (4.13), with the inclusion of the *exact* Hankel function, is rewritten along this path as

$$I_1 = \int_{SDP} A_1(k_\rho, z, z')H_0^{(2)}(k_\rho\rho)k_\rho\frac{dk_\rho}{d\tau}dk_\rho, \tag{4.50}$$

with the following derivative

$$\frac{dk_\rho}{d\tau} = \frac{d\alpha}{d\tau}\frac{dk_\rho}{d\alpha} = \frac{\sqrt{2}e^{j\pi/4}}{1-\dfrac{j\tau^2}{2}}k_2\sin\alpha, \tag{4.51}$$

where α is known, owing to the back transformation.

If we take $\psi = 0$, we obtain the integration path of Figure 4.5. This path passes through the saddle point at k_2, and is partly located on the lower Riemann sheet. To observe how the integrand of I_1 behaves on this lower Riemann sheet, we plotted it in Figure 4.13 for different distances ρ, i.e. $\rho = 0.01\lambda_0$ and $\rho = 0.02\lambda_0$. To perform this numerical integration a Gauss-Kronrod (30-61 points) quadrature rule has been applied. We have considered a structure of selection 13 in Figure 2.6, with $d_1 = 0.1\lambda$, $\varepsilon_{r,1} = 9$, and $\varepsilon_{r,2} = 1$.

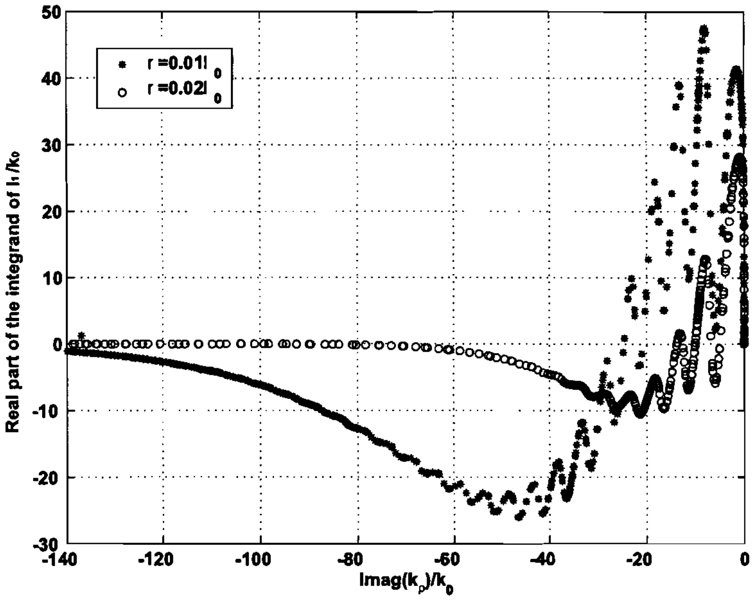

Figure 4.13: values for the real part of the integrand of I_1 along the SDP on the lower Riemann sheet in the k_ρ-plane for $\psi = 0$ and for the distances $\rho = 0.01\lambda_0$ and $\rho = 0.02\lambda_0$.

We observe that the integrand decays much faster, as ρ increases, and therefore we can shorten the length of the tail. This length will be measured by the $\mathrm{Im}(k_\rho)$, which is for the one in Figure 4.13 equal to $144k_0$. The distance ρ, which is also present in the argument of the Hankel function, gives rise to another problem, i.e., the influence of the leaky-wave residues. Therefore, let us recall Equation (4.9), which gives us the residue of a leaky-wave pole, i.e.,

$$\mathrm{Res}(k_\rho = k_{lw}) = -2\pi j \lim_{k_\rho \to k_{lw}} \left[(k_\rho - k_{lw}) A_1(k_\rho, z, z') H_0^{(2)}(k_\rho \rho) k_\rho \right]. \tag{4.52}$$

If the distance ρ decreases, the value of the Hankel function $H_0^{(2)}(k_\rho \rho)$ does not decay rapidly for increasing k_ρ. And since we have to multiply with k_ρ, whose imaginary part can be very large, the residue can be large as well and must therefore be taken into account. This implies that if ρ decreases, the residues of more leaky-wave poles have to be added to the integral, since their contributions cannot be neglected. To locate these singularities, we have to increase the search area in Figure 4.6. More explicitly, this implies that we have to increase the length L. However, if we do not change the density of the grid, the total computation time increases, since more closed contours have to be computed, as will be shown in Section 5.1.2.

We have seen in Section 4.2.1, that if we change the angle ψ, the SDP changes too. To observe what happens to the SDP in the k_ρ-plane, let us increase the height $|z - z'|$ in such a way that $|z - z'|/\rho = 0.33$, and thus $\psi = 18.26°$. If we take $\rho = 0.01\lambda_0$ again, the SDP for this angle is shown in Figure 4.14. A branch point is located in $k_\rho = k_0$. Its corresponding branch cut has been included as well, to distinguish between those parts of the integration path that are located on the lower and upper Riemann sheet. We see that the tails of the integration path also widen by the angle ψ and thus **always** end on the upper Riemann sheet to meet the radiation condition. Owing to this widening, the most lower leaky-wave residues are already 'inside' the integration path, which decreases the search area length L and consequently the computation time and the error in the final result. In Figure 4.15, we plotted the real part of the integrand of I_1 again, but now for the *total* integration path. We see that most of the oscillations have disappeared, since the exponent $e^{-jk_{z,2}|z - z'|}$ ensures that we have exponential decay on the upper Riemann sheet.

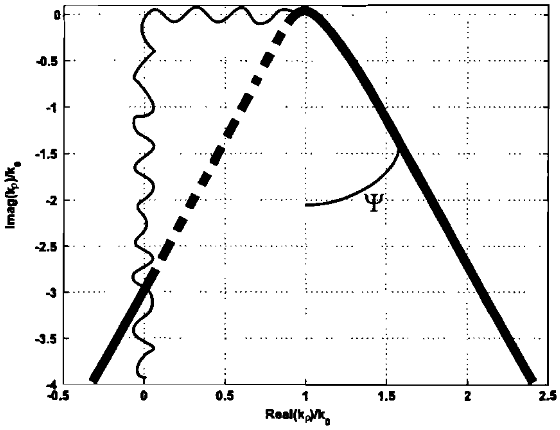

Figure 4.14: the SDP in the k_ρ-plane for a typical case in which $|z - z'|/\rho = 0.33$ and the branch point is located at $k_\rho = k_0$.

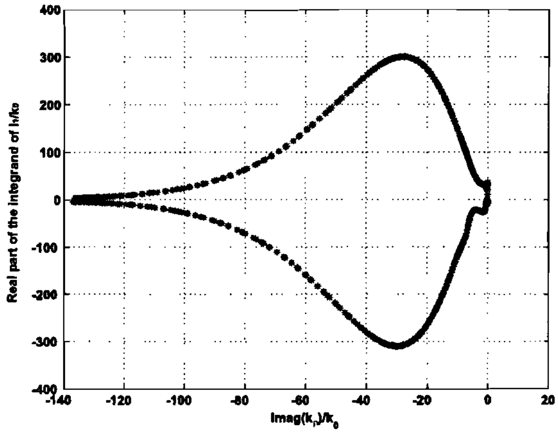

Figure 4.15: values for the real part of the integrand of I_1 along the SDP in the k_ρ-plane $\rho = 0.01\lambda_0$ and $|z - z'| = 0.0033\lambda_0$.

Next, let us increase the distance $|z - z'|$ to $|z - z'|/\rho = 3$. For this configuration, the integration path in the k_ρ-plane is shown in Figure 4.16 and the real part of the integrand of I_1 in Figure 4.17. We observe that the integrand decays faster, owing to the exponential $e^{-jk_{z,2}|z - z'|}$, and that it is possible to shorten the tail length. Hence, we have the worst-case scenario if the angle $\psi = 0$ and ρ gets small, since then the tail length and the search area L have to be large.

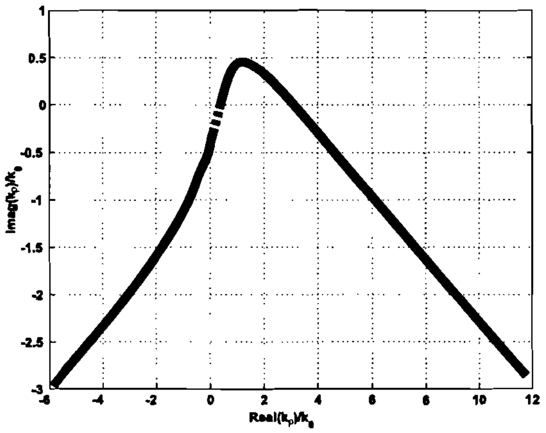

Figure 4.16: the SDP in the k_ρ-plane for a typical case in which $|z - z'|/\rho = 3$ and the branch point is in $k_\rho = k_0$.

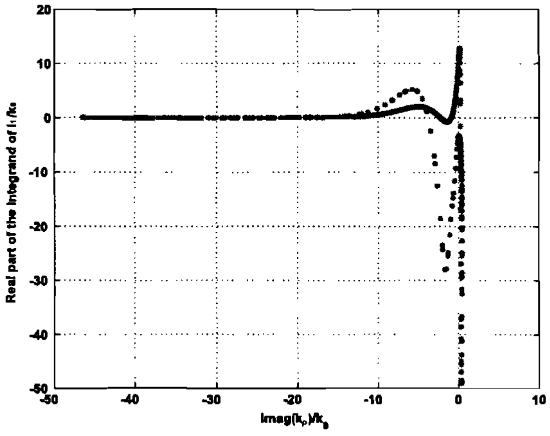

Figure 4.17: values for the real part of the integrand of I_1 along the SDP in the k_ρ-plane $\rho = 0.01\lambda_0$ and $|z - z'| = 0.03\lambda_0$.

Changing the SDP near surface-wave singularities

In Figure 4.14 we have shown that the tail of the SDP widens with the angle ψ. This means that the integration path may come close to a surface-wave pole for certain angles ψ and consequently integration may take longer than usual, due to the high amplitude variations in the vicinity of this pole. These angles ψ are given by the Equations (4.38) and (4.39). If this happens, the integration path will be divided into four intervals. This

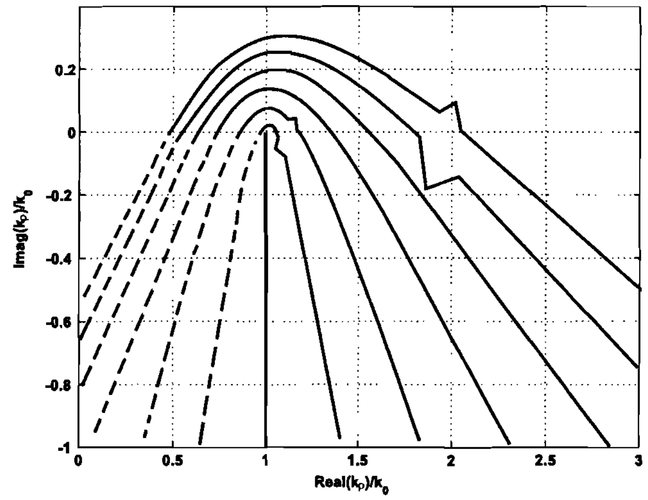

Figure 4.18: changing the SDP to avoid the surface-wave singularities at $k_\rho \approx 1.12k_0$ and $k_\rho \approx 1.97k_0$.

is shown in Figure 4.18, where we increased the distance $|z - z'|$ for a constant ρ for a structure which has two surface-wave poles located at $k_\rho \approx 1.12k_0$ and $k_\rho \approx 1.97k_0$. We see that the integration path now avoids the surface-wave singularities. However, note that this method can only be applied if the surface-wave singularities are not located too close to each other or too close to a branch point. A similar approach can be applied to avoid the leaky-wave singularities.

4.3 Far-field asymptotic approximation

In the far field, we can approximate the solution of the integrals I_n analytically by applying the so-called *stationary-phase* or *saddle-point method* [3]. This method gives us the leading-order approximation, where the Method of Steepest Descent provides us also with all higher-order approximations, in closed form. To apply this saddle-point method, we need the location of the saddle point. As already discussed in Section 4.2.1, this saddle point is in the α-domain located at $\alpha = \psi$ and, with the aid of Equation (4.16), in the k_ρ-domain at $k_{\rho\,\mathrm{sp}} = k_2 \cos\psi$, where the wavenumber k_2 corresponds again to a half space region.

Since the phase function of Equation (4.15) varies rapidly for large ρ or/and $|z - z'|$, the contribution to the integral is small because of the cancellation of the positive and negative parts of the integrand, as can be seen in Figure 4.19. However, in the vicinity of the saddle point, where $q'(k_\rho, \rho, z, z') = 0$, the exponential term does not vary rapidly. Hence, most of the contribution to the integration will come from the neighbourhood of the saddle point.

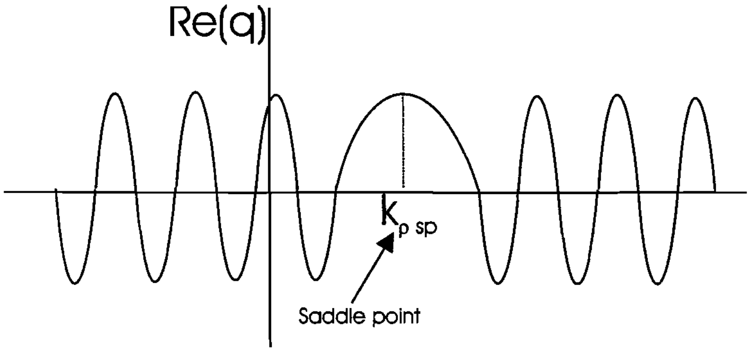

Figure 4.19: a saddle point occurs there where $q'(k_\rho, \rho, z, z') = 0$, and thus the exponential varies slowly.

Let us recall Equation (4.13), i.e.,

$$I_1 = \int\limits_{SIP} B_1(k_\rho, z, z')\sqrt{\frac{2}{\pi k_\rho \rho}}e^{-j(k_\rho \rho - \pi/4)}e^{-jk_{z,2}|z - z'|}k_\rho dk_\rho, \tag{4.53}$$

with

$$B_1(k_\rho, z, z') = A_1(k_\rho, z, z')e^{jk_{z,2}|z - z'|}. \tag{4.54}$$

The function $B_1(k_\rho, z, z')$ is *slowly varying*, since we extracted the exponential, and can be approximated in the vicinity of the stationary phase point by $B_1(k_{\rho\,\mathrm{sp}}, z, z')$. Since this function does not depend on the integration variable k_ρ, it can be extracted from the integral of Equation (4.13), i.e.,

$$I_1 = B_1(k_{\rho\,\mathrm{sp}}, z, z') \int\limits_{-\infty}^{\infty} H_0^{(2)}(k_\rho \rho) e^{-j\sqrt{k_0^2 - k_\rho^2}|z - z'|}k_\rho dk_\rho. \tag{4.55}$$

Indefinite integration to z gives

$$\int I_1 dz = B_1(k_{\rho\,\mathrm{sp}}, z, z') \int\limits_{-\infty}^{\infty} \frac{H_0^{(2)}(k_\rho \rho)k_\rho}{-j\sqrt{k_0^2 - k_\rho^2}} e^{-j\sqrt{k_0^2 - k_\rho^2}|z - z'|}dk_\rho. \tag{4.56}$$

According to [6, p. 481], the following identity holds

$$\frac{e^{-jk_0 r}}{4\pi r} = \frac{1}{8\pi j} \int\limits_{-\infty}^{\infty} \frac{H_0^{(2)}(k_\rho \rho)k_\rho}{\sqrt{k_0^2 - k_\rho^2}} e^{-j\sqrt{k_0^2 - k_\rho^2}|z - z'|}dk_\rho, \tag{4.57}$$

where r is in polar coordinates given by

$$r = \sqrt{\rho^2 - 2\rho\rho' \cos(\phi - \phi') + \rho'^2 + (z - z')^2}. \tag{4.58}$$

Substitution of Equation (4.57) in Equation (4.56) gives

$$\int I_1 dz = -2\frac{e^{-jk_0 r}}{r} B_1(k_{\rho\,\mathrm{sp}}, z, z'). \tag{4.59}$$

If we take to derivative of Equation (4.59) with respect to z, the integral I_1 becomes

$$I_1 = -2B_1(k_{\rho\,\mathrm{sp}}, z, z')\frac{\partial}{\partial z}\left[\frac{e^{-jk_0\sqrt{|z - z'|^2 + \rho^2}}}{\sqrt{|z - z'|^2 + \rho^2}}\right], \tag{4.60}$$

with

$$F(r) = 2\frac{e^{-jk_0 r}}{r}\left(jk_0 + \frac{1}{r}\right). \tag{4.61}$$

Since $H_0^{(2)}(x) = -H_2^{(2)}(x)$ for large arguments, as can be verified with Equation (4.1), the following asymptotic expression for I_2 is obtained

$$I_2 = -B_2(k_{\rho\,\mathrm{sp}}, z, z') \sin\psi F(r), \tag{4.62}$$

where $F(r)$ is given by Equation (4.61). For the integrals I_3 and I_4, we have to integrate with respect to ρ instead of z, to be able to use the identity of Equation (4.57). By using the relationship $H_0^{(2)}(x) = jH_1^{(2)}(x)$ for large arguments, we get

$$\begin{aligned} I_3 &= jB_3(k_{\rho\,\mathrm{sp}}, z, z') \left(\frac{k_z(z)}{k_z(z')} \right) \bigg|_{\mathrm{sp}} \cos\psi F(r), && (4.63) \\ I_4 &= jB_4(k_{\rho\,\mathrm{sp}}, z, z') \cos\psi F(r), && (4.64) \end{aligned}$$

where $F(r)$ is again given by Equation (4.61).

The far field expression for the integral I_5 is obtained if we integrate twice with respect to ρ, and is given by

$$I_5 = B_5(k_{\rho\,\mathrm{sp}}, z, z') \left(\frac{1}{k_z(z')} \right) \bigg|_{\mathrm{sp}} \cos^2\psi G(r), \tag{4.65}$$

with

$$G(r) = 2\frac{e^{-jk_0 r}}{r} \left(k_0^2 - \frac{2jk_0}{r} - \frac{2}{r^2} \right). \tag{4.66}$$

Observe that if we take $\rho = 0$, we can still obtain correct results, although the Hankel function only exists in the limit $\lim_{\rho \to 0} H(k_\rho \rho)$ and not in $\rho = 0$ exactly. However, owing to the identity of Equation (4.57), this singularity has been replaced by $r = |z - z'|$.

Chapter 5

Numerical results

In this chapter, we will discuss the numerical results of the integrals I_n obtained with the theory in the previous chapters. We will perform the integration along the First-Contour Deformation (FCD) of Figure 4.2 and the Steepest-Descent Path (SDP), discussed in Section 4.2 and compare both numerical results in Section 5.1. First, we will discuss the *relative error* and the difference in *computation time* between the two integration paths for the worst-case scenario, i.e. $\psi = 0$, in the Sections 5.1.1 and 5.1.2. These computations will be performed on a structure with one layer located on top of a perfectly conducting ground plane.

Since we solved the transmission-line equations for several practical configurations (cf. Section 2.3) instead of using a general procedure like the one suggested by [3], we will show the gain in computation time of this time-consuming job when searching for surface- and leaky-wave singularities in Section 5.1.3. The average computation time per integral for each selection is computed in Section 5.1.4. In Section 5.2, we will compare the results of the integral I_1 integrated along the FCD and SDP with the far field asymptotic approximations, which are derived in Section 4.3.

5.1 Comparison of the results obtained with the FCD or the SDP as integration path

In Section 4.2.3, we have seen that it takes the most effort to obtain accurate results at the angle $\psi = 0$ for small ρ when integrating along the SDP. This is due to the *tail length*, which has to be increased for small ρ, and the *amount of added leaky-wave residues*, whose contribution cannot be neglected since the Hankel function does not decay rapidly anymore. For large ρ on the other hand, integration along the FCD causes errors, due to rapid phase oscillations, as discussed in Section 4.1. The comparison of the **relative error** in and **computation time** of the results obtained via the two integration paths, gives us a good insight in the efficiency of the SDP-method. For the numerical integration, a Gauss-Kronrod (30-61 points) quadrature rule is used. For practical purposes, we will only consider the range:

$$0.01\lambda_0 < \rho(\lambda_0) < 10\lambda_0. \tag{5.1}$$

5.1.1 Relative error for a structure with one layer

First, let us demonstrate the influence of adding more leaky-wave residues to the integral along the SDP for $\psi = 0$. Therefore, we consider the configuration of Figure 2.4(a), where the slab has a permittivity of nine, and the region above is filled with air, i.e. $\varepsilon_{r,1} = 9$; $\varepsilon_{r,2} = 1$. We assume that the thickness of the slab $d_1 = 0.1\lambda_0$.

For this configuration, we obtain, with the search routine presented in Section 4.1.1, two surface-wave poles at $k_\rho \approx 1.12k_0$ and $k_\rho \approx 1.97k_0$. The three leaky-wave singularities closest to the real axis are given by $k_\rho \approx (0.20 - 6.87j)k_0$, $k_\rho \approx (0.19 - 12.13j)k_0$, and $k_\rho \approx (0.18 - 17.2j)k_0$. In Figure 5.1, we plotted the relative error in I_1 between the FCD and the SDP as a function of the distance ρ, where we have kept the range of Equation (5.1) in mind. Since the relative error is the highest for small ρ, the influence of the leaky-wave residues is plotted especially for that area. The tail length of the SDP is assumed to be 36k_0, and the tail lengths of the FCD that come and go to $-j\infty$ are chosen in such way that the integrand has decayed to zero. Their exact lengths will be discussed in Section 5.1.2.

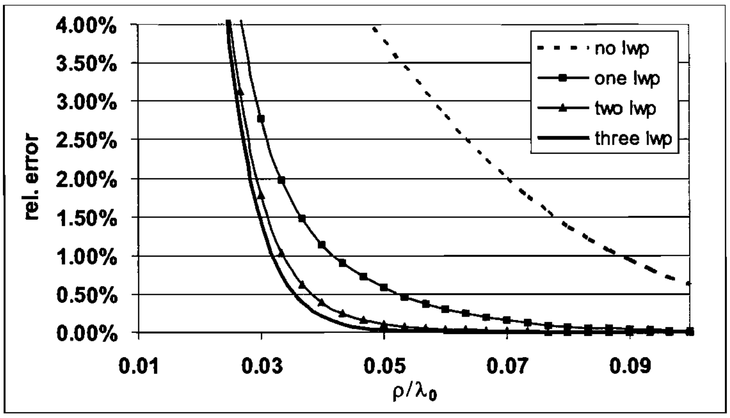

Figure 5.1: influence of the leaky-wave residues on the relative error in I_1, when integrating along the FCD or the SDP for a slab thickness of $d_1 = 0.1\lambda_0$.

In Figure 5.1, we see that if we add the residues of more leaky-wave singularities to the integral I_1 along the SDP, the relative error decreases at a certain distance ρ.

Now, let us change the tail length and keep the amount of added leaky-wave residues constant at three. In Figure 5.2, the influence of the tail length on the relative error in I_1 is plotted as a function of ρ. We observe that also by changing the length of the tail, we can decrease the relative error at a certain distance ρ. This can also be seen in Figure 4.15, where the integrand has become exponentially small for a tail length of about $144k_0$ for $\rho = 0.01\lambda_0$. This means that with a tail length of $225k_0$, as shown in Figure 5.2, the integrand has definitely decayed to zero. Any further extension of the tail beyond $225k_0$ does not decrease the error at $\rho = 0.01\lambda_0$ anymore. However, we still observe that there is a relative error in I_1 of about 0.55%, which can only be decreased if we add more contributions of leaky-wave residues.

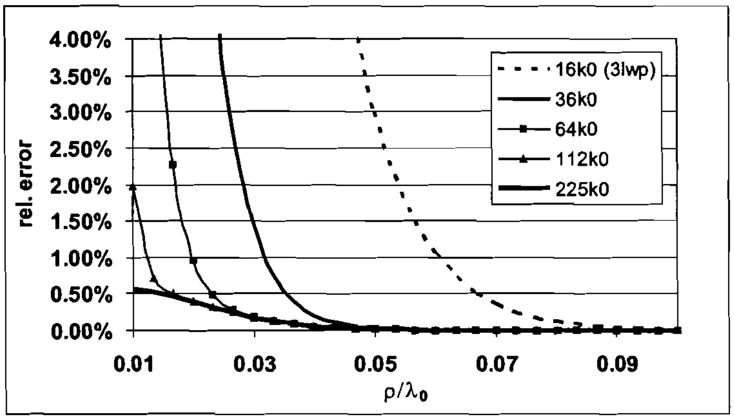

Figure 5.2: influence of the tail length on the relative error in I_1 when integrating along the FCD or the SDP for a constant amount of three added leaky-wave poles.

Changing the thickness of the slab

Next, let us increase the slab thickness to $d_1 = 0.6\lambda_0$. If we consider a *maximum tolerable relative error* of 2% for all ρ in the range of equation (5.1), the tail length should be at least $112k_0$ for a thickness of $d_1 = 0.1\lambda_0$, according to Figure 5.2, and three leaky-wave residues have to be added to the integral. If we use the same search areas for this slab thickness as we did to find the 1, 2 and 3 leaky-wave poles in Figure 5.1, we now find 17, 23, and 32 leaky-wave poles, respectively. Hence, more leaky-wave singularities are present in the same search area if we increase the slab thickness. This means that we also have more contributions of leaky-wave poles just *outside* the search area, and therefore the relative error for a certain distance ρ will be larger. This is shown in Figure 5.3. There where

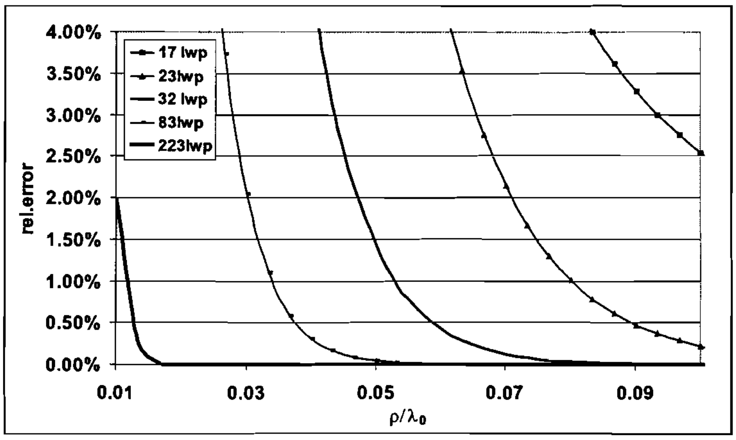

Figure 5.3: influence of the leaky-wave residues on the relative error in I_1 when integrating along the FCD or the SDP for a slab thickness of $d_1 = 0.6\lambda_0$.

the relative error for a slab thickness of $d_1 = 0.1\lambda$ remained below the maximum tolerable error of 2% for all ρ in the range of Equation (5.1) if we added three leaky-wave poles, we observe in Figure 5.3 that the distance $\rho > 0.046\lambda_0$, if we use the same search area. So, if we want to lower this distance, we have to increase the search area for leaky-wave poles again. Increasing the tail length does not decrease the relative error anymore, since it is already large enough. In Figure 5.3, we see that we need at least 223 leaky-wave poles to reach an accuracy of 2% at $\rho = 0.01\lambda_0$. To find these leaky-wave poles, the imaginary part of the search area, denoted by L in Figure 4.6, reaches from $0 - 180k_0$. One can imagine that it takes a lot of time to find all these poles in such a large search area, as we will show in Section 5.1.2.

However, computation time can be reduced, owing to the *pattern* in the location of the leaky-wave poles in Figure 4.6. If the location of the most upper leaky-wave poles is known, the other locations can be obtained from this pattern. This reduces the size of the search area and consequently the computation time. However, this acceleration process has not been applied in this report.

Changing the dielectric material in the slab

Next, let us demonstrate the influence on the relative error in I_1, if we change the permittivity of the medium in the slab. Therefore, we assume that $\varepsilon_{r,1} = 2$ and that $d_1 = 0.1\lambda_0$ again. In Figure 5.4, we plotted the influence of the tail length on the relative error in I_1 for this dielectric material. If we compare this figure with Figure 5.2, we notice that a lower permittivity decreases the relative error in I_1 at a certain distance ρ. This means that the relative error in I_1 between integration along the SDP and FCD depends not only

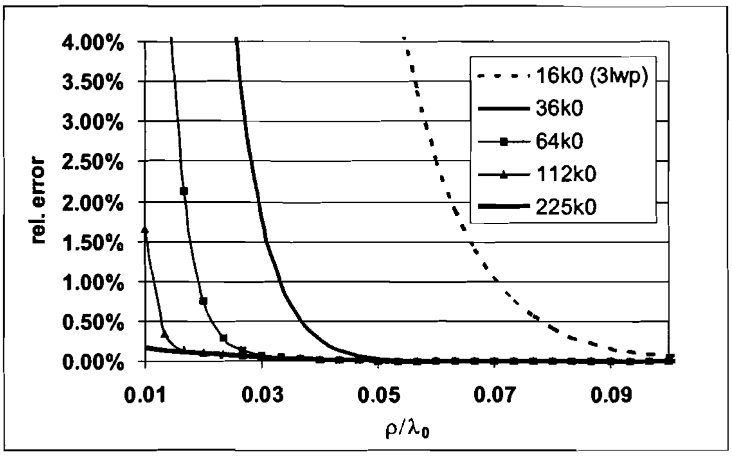

Figure 5.4: influence of the tail length on the relative error in I_1 when integrating along the FCD or the SDP with $\varepsilon_{r,1} = 2$ and $d_1 = 0.1\lambda_0$.

on the *tail length* and the *amount of added leaky-wave poles*, but also on the *thickness* and *dielectric* of the slab. Therefore, it is very hard to obtain a distance ρ beyond which the relative error remains below 2% for all ρ in the range of Equation (5.1), since this distance changes for each different configuration of the stratified structure.

Error in FCD for large ρ

In Section 4.2.3, we already mentioned that for large ρ, the integrals computed along the FCD lose accuracy. This loss is due to the highly oscillatory behavior of the Hankel function for large arguments $k_\rho \rho$. This implies that the result of the integral I_1 with the SDP as integration path is more accurate than the one with the FCD for large ρ. To demonstrate this, let us recall the geometry of Figure 2.4(a) again, with a slab thickness of $d_1 = 0.1\lambda_0$ and dielectric permittivities of $\varepsilon_{r,1} = 9$ and $\varepsilon_{r,2} = 1$. Then Figure 5.5 shows us the relative error in I_1 between the FCD and the SDP for large distances ρ.

5.1.2 Computation times for a structure with one layer

We will compare the computation times needed to compute the integral I_1 between the two integration paths, i.e. the FCD or the SDP, for structures with one layer.

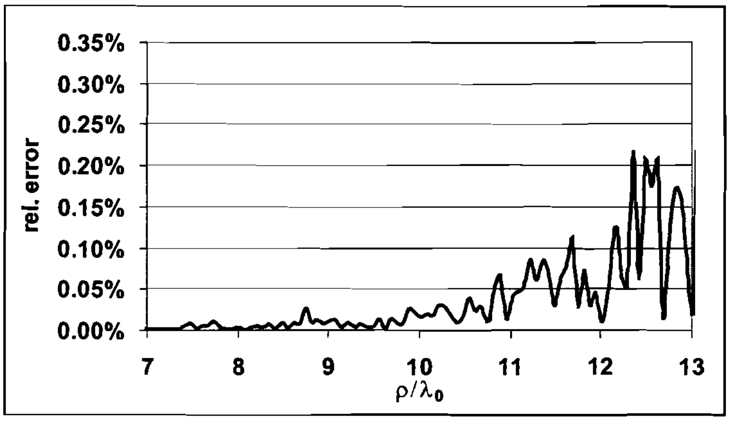

Figure 5.5: relative error in I_1, due to the oscillatory behavior of the Hankel function for large arguments if we integrate along the FCD.

Tail lengths of the SDP and FCD

The tail length does not only influence the relative error, but also the computation time. Since, the longer the tail, the slower the integral is computed. In Figure 4.13, we have already seen that the tail of the SDP can be shortened if the distance ρ increases. However, we have to keep in mind that we do not lose the accuracy in the final result by shortening the tail too much. Therefore, we divide the range of Equation (5.1) in the experimentally obtained intervals given in *Table* 5.1, for various tail lengths. For the same reason, the tail lengths of the FCD that come and go to $-j\infty$ have to be adapted as ρ becomes small, as mentioned in Section 4.1. However, to make the program more general, we also want to be able to use this path below the distance $\rho = 0.01\lambda_0$. Experimentally, we have obtained tail lengths for the FCD, given in *Table* 5.2, for which we are certain that the integrand has decayed to zero, i.e., These tail lengths are used to perform all following computations.

interval	tail length
$0.01\lambda_0 - 0.04\lambda_0$	$144k_0$
$0.04\lambda_0 - 0.1\lambda_0$	$40k_0$
$0.1\lambda_0 - 0.3\lambda_0$	$16k_0$
$0.3\lambda_0 - 10\lambda_0$	$4k_0$

Table 5.1: the tail length of the SDP is adapted to the distance ρ between source and observer to perform the integration as fast as possible, but keep its accuracy.

To decrease computation time, we could also use a Laguerre-Gauss quadrature for the non-

interval in ρ	tail length
below $1\lambda_0$	$3k_0\lambda_0/\rho(\lambda_0)$
$1\lambda_0 - 10\lambda_0$	$3k_0$

Table 5.2: the tail length of the FCD is adapted to the distance ρ between source and observer in such a way that this distance can be smaller than $\rho = 0.01\lambda_0$.

oscillating exponentially decaying end of the tail, for example in Figure 4.13, instead of the Gauss-Kronrod quadrature. This Laguerre-Gauss quadrature has weighting functions $W(x) = e^{-x}$, and therefore suits better for these tail end, since less points are needed. However, this quadrature has not been applied in this report, so all integrals are computed with the Gauss-Kronrod quadrature.

Changing the length L of the search area

In Figure 5.1, we have adjusted the length L of the search area in such a way that we found 1, 2, and 3 leaky-wave poles. Since the amount of poles is small compared with the amount found in Figure 5.3 for the same search areas, a less dense grid can be used here. Theoretically, we should be able to find all singularities inside a search area, when applying Equation (4.8), however, in practice we have noticed that sometimes a singularity is missing. Since this cannot be allowed, we have searched for a grid in which **always** all leaky-wave singularities are found. This turned out to be a 20 × 20 grid with a length of $L = 20k_0$, under the condition that the thickness of all slabs is less than $d_{tot} = 0.4\lambda_0$. For a stratification that is thicker than $d_{tot} = 0.4\lambda_0$, a 40 × 40 grid with a length of $L = 20k_0$ is used. If we have to search for poles below $L = 20k_0$, we keep the density of the grid constant. This has consequences for the total computation time. Therefore, we plotted in Figure 5.6, the amount of time needed to find the leaky-wave poles by a dashed line, versus the length L, computed on a pentium 4 computer of 2.6GHz.

We see that for lengths larger than $L = 20k_0$, the computation time increases drastically. This means that if we have a stratification which is thicker than $d_{tot} = 0.4\lambda_0$, and thus a grid of 40 × 40 for a length $L = 20k_0$ is used, the time to find the leaky-wave poles is already 7.5 seconds. If we also add the time needed to locate the surface-wave poles, we obtain the solid line in Figure 5.6. This loss in time should be compensated by the fast computation of the integral along the SDP. This implies that the amount of integrals to be computed should be larger than a certain break-even point if we want to make use of the integration along the SDP.

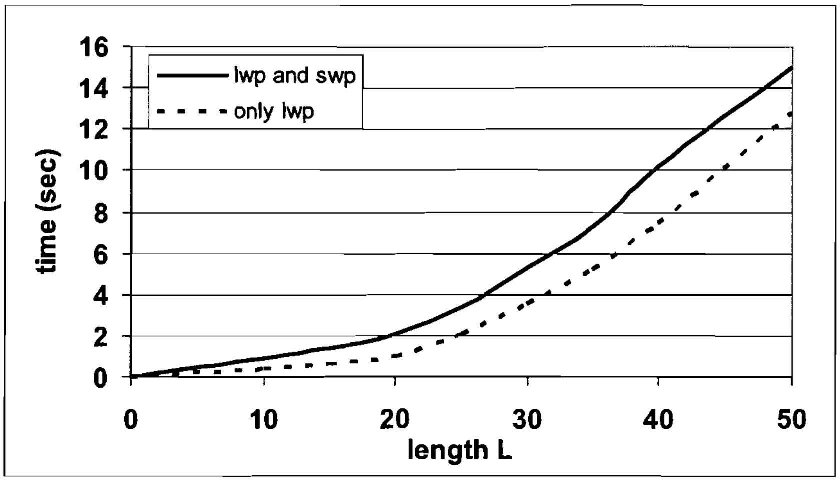

Figure 5.6: amount of time needed to find all poles (solid) or only the leaky-wave poles (dashed) for a structure with one layer versus the search-area length L.

Break-even points

We wish to find the break-even points for all structures discussed in Section 5.1.1. First, we will discuss the structure with a slab thickness of $d_1 = 0.1\lambda_0$ and a permittivity of $\varepsilon_{r,1} = 9$, where the magnetic dipole is located on the ground plane. Because the thickness of the slab is less than $d_{tot} = 0.4\lambda_0$, we will use a grid size of 20×20 with a length $L = 20k_0$. Since, the third leaky-wave singularity is located at $k_\rho \approx (0.18 - 17.2j)k_0$, and the fourth one at $k_\rho \approx (0.18 - 22.3j)k_0$, we have to add the residues of the first three leaky-wave poles to the integral I_1, when integrating along the SDP. In *Table* 5.3, we have tabulated the average computation times of the integral I_1 at a distance $\rho = 0.01\lambda_0$ from the source, where we have used *Table* 5.2 to obtain the tail lengths of the FCD and SDP. We also included the computation time for integration along the SDP with a tail length of $225k_0$, corresponding to a relative error of 0.55% at $\rho = 0.01\lambda_0$, as shown in Figure 5.2. If we compare the average computation time per integral of this path with the one which has a

	pole search (msecond.)	average comp. time per integral (msecond.)
SDP($144k_0$)	2100	41
SDP($225k_0$)	2100	48
FCD($300k_0$)	0	210

Table 5.3: computation times of I_1 by integration along the SDP and the FCD for a distance $\rho = 0.01\lambda_0$ and tail lengths of $144k_0$ and $225k_0$ for the SDP.

tail length of $144k_0$, the difference is only 7 msecond. However, if we calculate for example 1000 integrals, this corresponds to 7 seconds, which is quite a lot as we will see later on in this section.

From *Table* 5.3, the break-even point between the SDP with tail length $144k_0$ and the FCD can be calculated, and is given by 13 integrals. However, this is not a practical situation since all integrals are taken at a distance $\rho = 0.01\lambda_0$ from the source. Therefore, we will divide the range of Equation 5.1 into 5000 equal pieces, which gives us a break-even point of 79 integrals. The average time per integral is, for integration along the SDP, 9.58 msecond. and for integration along the FCD 36.4 msecond. The same break-even point is obtained if we change the relative permittivity of the slab into $\varepsilon_{r,1} = 2$.

Let us increase the slab thickness to $d_1 = 0.6\lambda_0$ and assume that the relative permittivity of the slab is $\varepsilon_{r,1} = 9$. Since $d_{tot} > 0.4\lambda_0$, we now use a grid size of 40 × 40 and a length $L = 20k_0$. According to Figure 5.6, the pole search takes about 10.2 seconds now. However, only 40 leaky-wave poles are found in the search area which means that, according to Figure 5.3, integration along the SDP is only possible if $\rho > 0.046\lambda_0$, due to the 2% boundary. If we divide the range of Equation 5.1 into 5000 equal pieces, but now with a lower boundary at $\rho = 0.046\lambda_0$, we obtain a break-even point at 392 integrals. The average time per integral is for integration along the SDP 11.16 msecond. and for integration along the FCD 37.2 msecond. If we compare these computation times with the ones obtained for the structure with slab thickness $d_1 = 0.1\lambda_0$, e.g. 9.58 msecond. and 36.4 msecond., we notice that the average time per integral does not differ very much. Therefore, the break-even point strongly depends on the amount of time needed to find the poles in the k_ρ-plane.

In *Table* 5.4, we showed the starting values of ρ, the grid size, and the break-even points for several values of the thickness of the slab for $L = 20k_0$. We see that as soon as the thickness of the slab passes $d_1 = 0.42\lambda_0$, the starting value of ρ starts to change. To decrease this value of ρ, we should increase L to find more leaky-wave poles, with the consequence that the break-even point increases. For example, to remain below the 2% boundary at $\rho = 0.01\lambda_0$ with a slab thickness of $d_1 = 0.6\lambda_0$, we have to find at least 223 leaky-wave poles, according to Figure 5.3, which corresponds to a break-even point of 2160 integrals, instead of the 392 integrals shown in *Table* 5.4.

Changing the SDP near surface-wave singularities

Finally, we will discuss the advantage of an integration path that avoids the surface-wave singularities as the angle ψ increases, as suggested in Section 4.2.3. Again, we will use a structure with a single slab of thickness $d_1 = 0.1\lambda_0$ and relative permittivity $\varepsilon_{r,1} = 9$. The region above the slab is filled with air, i.e. $\varepsilon_{r,2} = 1$. In Figure 4.18, the SDP's for

thickness[$d_1(\lambda_0)$]	grid size	break-even points(int.)	start. $\rho(\lambda_0)$
0.1	20 × 20	79	0.010
0.2	20 × 20	98	0.010
0.4	40 × 40	414	0.010
0.42	40 × 40	403	0.010
0.43	40 × 40	438	0.022
0.45	40 × 40	476	0.040
0.5	40 × 40	431	0.046
0.6	40 × 40	392	0.046

Table 5.4: the starting values of ρ, the grid size, and the break-even points for various thicknesses of the slab with permittivity $\varepsilon_{r,1} = 9$ for $L = 20k_0$.

different heights at a constant distance ρ are shown. The surface-wave poles are located at $k_\rho \approx 1.12k_0$ and $k_\rho \approx 1.97k_0$, which corresponds to $|z - z'| \approx 0.5\lambda_0$ and $|z - z'| \approx 1.33\lambda_0$, respectively, for a distance $\rho = 1\lambda_0$. If we compute the average time per integral at a height $|z - z'| \approx 0.5\lambda_0$, we obtain *Table* 5.5. We see that if the 'usual' SDP passes near a surface-wave singularity it is essential to use the 'changed' SDP path, since the average computation time differs almost by a factor of five.

	average comp. time per integral (msecond.)
SDP (usual)	58.9
SDP (changed)	11.9

Table 5.5: computation times of I_1 by integration along the 'usual' SDP and the 'changed' SDP for a path that is in the vicinity of a surface-wave pole.

5.1.3 Comparison between the pole and zero location methods

As discussed in Section 4.1.1, we search for the locations of the singularities in the k_ρ-plane with the aid of the analytically retrieved denominator of the functions $A_n(k_\rho, z, z')$. In this section, we compare the amount of time needed to compute the zeros of this denominator, with the amount of time needed to compute the poles of the functions $A_n(k_\rho, z, z')$. Therefore, we consider all relevant selections of Figure 2.6, which are the ones with layers, and keep the total thickness of all layers below $d_{tot} = 0.4\lambda_0$ for $L = 20k_0$. In *Table* 5.6, the computation times for these selections are shown. The kind of dielectric in the slab(s) does not alter these times.

Selection	Comp. time of poles of A_n(sec)	Comp. time of zeros of A_n(sec)
3	143	2.4
4	192	3.2
13	91	2.1
14	141	2.6
15	204	4.1
23	106	1.8
24	120	2.2

Table 5.6: time needed to locate the singularities in the k_ρ-plane between the methods where the poles of the functions $A_n(k_\rho, z, z')$ or the zeros of its denominator are calculated.

We observe that the computation times to locate the zeros of the denominator are always much lower than the ones in which we find the poles of the functions $A_n(k_\rho, z, z')$. Therefore, we have chosen for the former approach to locate the singularities in the k_ρ-plane, with the disadvantage that the amount of structures that can be computed is limited, since the transmission-line equations should be solved by hand for each structure. Therefore, we have discussed an alternative method in Appendix A to find the poles of a *general* stratified structure by determining the determinant of a matrix.

5.1.4 Average computation time per integral for all selections

For completeness, we will compute the average computation time per integral for all selections of Figure 2.6 for the angle $\psi = 0$, by dividing the interval of Equation (5.1) in 5000 subintervals of equal length. The thickness and the relative permittivities of the layers barely change the average computation time needed to compute one integral, as we have seen in Section 5.1.2. The results are written in *Table* 5.7 for integration along the FCD and SDP. For the selections 23 and 24, we do not have to compute the integral along the SDP, since the residues of the surface-wave poles represent all modes present between the two ground planes. However, these poles can occur on the total imaginary k_ρ-axis and on the real k_ρ-axis, up to the highest wavenumber, due to the absence of the branch cuts, as

Selection	FCD (msecond.)	SDP (msecond.)
1	11.2	4.1
2	23.2	16.5
3	31.4	24.0
4	41.1	27.8
11	10.6	4.3
13	36.4	9.6
14	40.2	12.6
15	58.8	23.6
23	18.6	0.4
24	31.2	0.7

Table 5.7: average computation time per integral for all selections.

discussed in Section 3.4. Therefore, their computation times can be very low if we adapt the search area to both axes.

In *Table* 5.7, we have seen that the integral is computed more efficiently if we integrate along the SDP instead of along the FCD. Now, let us have a look at the average computation times per integral for selection 13, if we divide the range of Equation (2.23) in the intervals, as introduced in *Table* 5.1, and divide these intervals again in 5000 subintervals with equal length. Then we obtain the average computation times shown in Table 5.8. We observe that

interval in ρ	FCD (msecond.)	SDP (msecond.)
$0.01\lambda_0 - 0.04\lambda_0$	59	16
$0.04\lambda_0 - 0.1\lambda_0$	33	10
$0.1\lambda_0 - 0.3\lambda_0$	24	8
$0.3\lambda_0 - 10\lambda_0$	20	7

Table 5.8: average computation times per integral computed along the FCD and SDP for a selection 13.

the average computation times in the first interval are the worst, since there convergence takes longer, as we have seen in Figure 4.13.

5.2 Evaluation of the far-field expressions.

In Section 4.3, we retrieved asymptotic far-field expressions for the integrals I_n. Since these are analytical expressions, their computation time is very small. For example, for selection 11, we obtain an average computation time of 0.2 msecond. per integral. This implies that as soon as we reach the far field, we should use these asymptotic evaluations.

To obtain some insight in the results for I_1 obtained with these asymptotic expressions, we will compare them with the results of this integral computed along the FCD to obtain the relative error. First, we consider a structure like selection 11 of Figure 2.6, where the half space is filled with air, i.e. $\varepsilon_{r,1} = 1$, and a magnetic dipole is located on the ground plane. Since there is no slab, we only have to compute the branch cut contribution. In Figure 5.7, the relative error between the two methods is shown, where $|Z| = |z - z'|$ is the distance between source and observer along the z-direction.

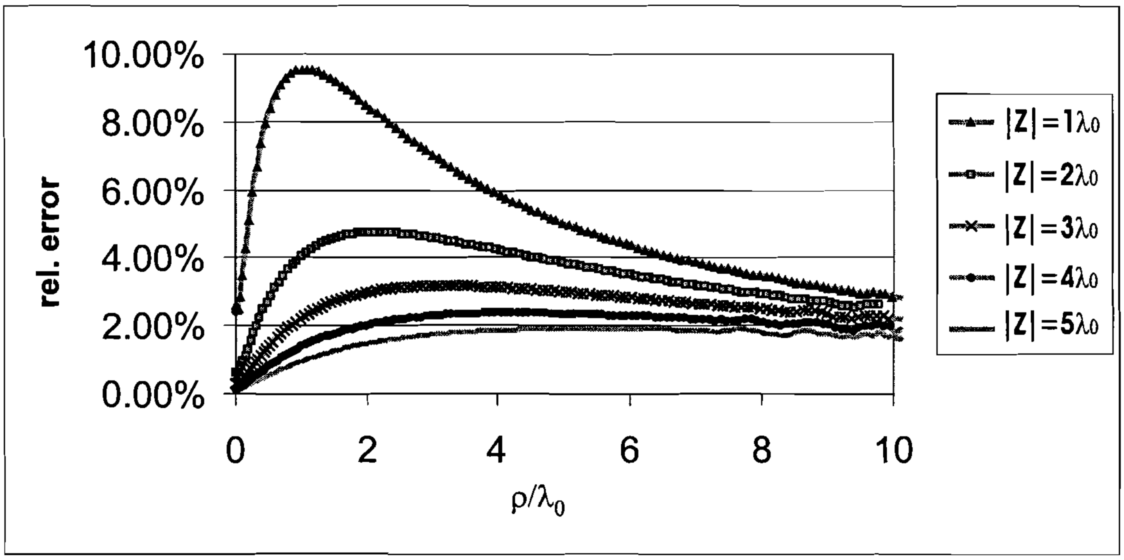

Figure 5.7: relative error in the integral I_1 between the far field asymptotic expression and the FCD for various distances $|Z| = |z - z'|$ for a structure of selection 11.

Notice that as soon as $|z - z'| \geq 5\lambda_0$, the relative error remains less than 2%, which we consider again as the maximum tolerable error, for all ρ in the range of Equation (5.1). Since a higher relative permittivity of the half space decreases the relative error, as we have discovered experimentally, $|z - z'| \geq 5\lambda_0$ is our reference beyond which we may use the far-field asymptotic-expressions for this structure. Also observe that the errors occurring in the integral computed along the FCD for large ρ are clearly visible. Therefore, the following computations will be performed along the SDP.

Further, we notice that the relative error is the worst at angles near $\psi \approx 45°$. This can be explained if we look at the phase function $q(k_\rho, \rho, z, z')$ of Equation (4.15). This function is plotted for $\psi = 88°$ and $\psi = 45°$, where $|z - z'| = 3\lambda_0$ in Figure 5.8 and 5.9, respectively. The saddle points are given by $k_{\rho\,\mathrm{sp}} \approx 0.03$ and $k_{\rho\,\mathrm{sp}} \approx 0.71$, respectively. We see that the major contribution to the integral is indeed located in the vicinity of the saddle point. If we compare Figure 5.8 with Figure 5.9, we notice that the cancellation of the oscillations is worse in the latter. This means that if the smoothly varying function $B_1(k_\rho, z, z')$ changes near the saddle point, these variations cause an error in the final result. Therefore, we plotted the function $B_1(k_\rho, z, z')$ in Figure 5.10. We observe that this function varies in the vicinity of the saddle point $k_{\rho\,\mathrm{sp}} \approx 0.71$ and is nearly constant near $k_{\rho\,\mathrm{sp}} \approx 0.03$. Therefore, the error in the latter will be less, as we have observed in Figure 5.7.

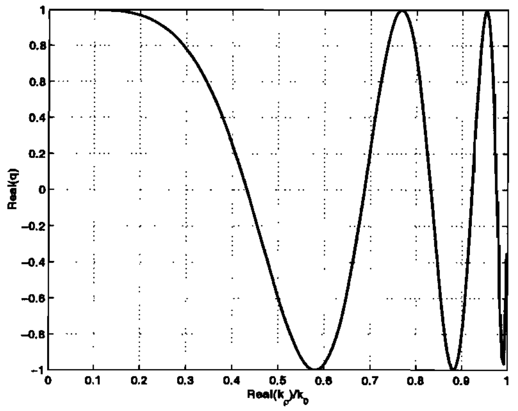

Figure 5.8: the phase function $q(k_\rho, \rho, z, z')$ for $\rho = 1/30|z - z'|$ and $|z - z'| = 3\lambda_0$ with saddle point at $k_{\rho\,\mathrm{sp}} \approx 0.03$.

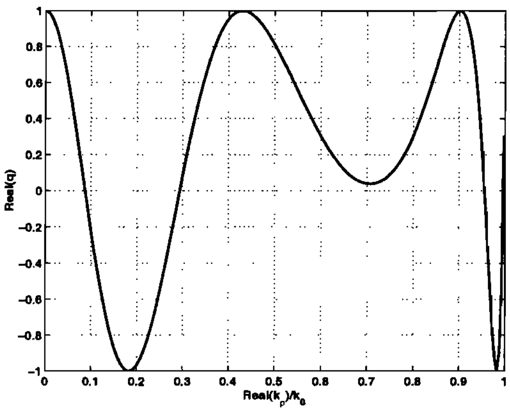

Figure 5.9: the phase function $q(k_\rho, \rho, z, z')$ for $\rho = |z - z'|$ and $|z - z'| = 3\lambda_0$ with saddle point at $k_{\rho\,\mathrm{sp}} \approx 0.71$.

Next, let us demonstrate what happens to the relative error if we add one layer with a thickness of $d_1 = 0.1\lambda_0$ to the structure. This is shown for several values of the relative permittivity of the layer for a height $|z - z'| = 5\lambda_0$ in Figure 5.11 and for a height $|z - z'| = 6\lambda_0$ in Figure 5.12. If we compare both plots, we see that we have to increase the distance $|z - z'|$ to remain below the 2% boundary. However, therefore the distance between source and observer should be about $|z - z'| = 6\lambda_0$. This implies that we cannot simply add the thickness of the layer $d = 0.1\lambda$ to the distance $|z - z'| = 5\lambda_0$ of Figure 5.7 as might seem obvious. This is due the fact that the relative error increases for increasing ρ. We also observe that for a relative permittivity of about $\varepsilon_{r,1} = 2$, the relative error increases the most in both figures. The relative error for higher permittivities always remains below this one.

Now, let us increase the slab thickness to $d_1 = 0.3\lambda_0$ and make a similar plot like the one

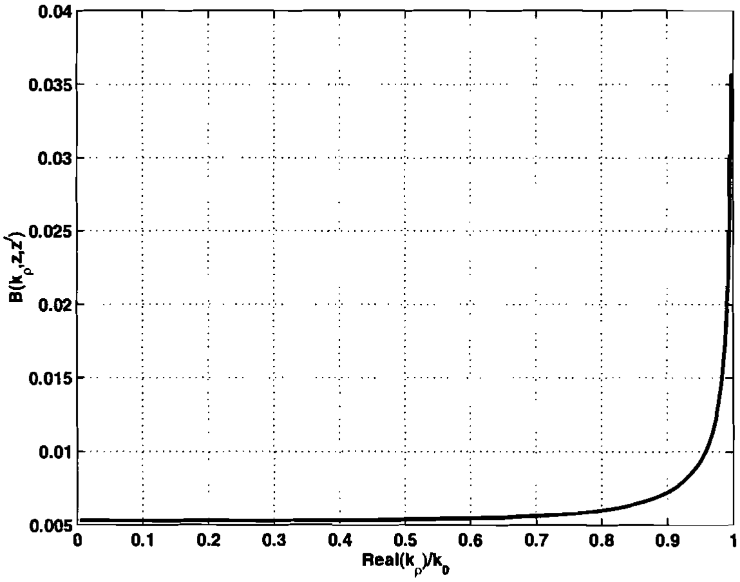

Figure 5.10: the smoothly varying function $B_1(k_\rho, z, z')$ for a structure with ground plane and a half space above with $\varepsilon_r = 1$.

in Figure 5.12. Then, we obtain Figure 5.13 for a height of $|z - z'| = 6\lambda_0$. We see that we have problems to reach our accuracy especially for small ρ. Also for large ρ and high relative permittivities, we lose accuracy. This means that we have to increase the distance $|z - z'|$ even more. Experimentally, we obtained that with a distance of $|z - z'| = 9\lambda_0$, all lines in Figure 5.13 remain below the 2% boundary.

Hence, it is difficult to observe a pattern in the relative error, and therefore, we are unable to give an exact distance $|z - z'|$ beyond which we can use these far-field expressions for structures with slabs, since they strongly depend on the *thickness* and the *relative permittivities* of the layers.

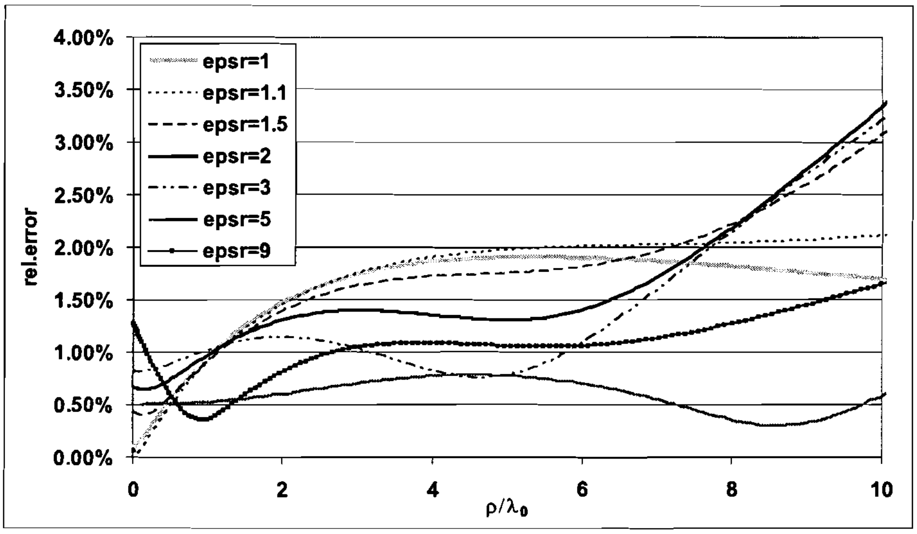

Figure 5.11: relative error in the integral I_1 between the far-field asymptotic-expression and the SDP for various relative permittivities at a height $|Z| = 5\lambda_0$ and a slab thickness of $d_1 = 0.1\lambda_0$.

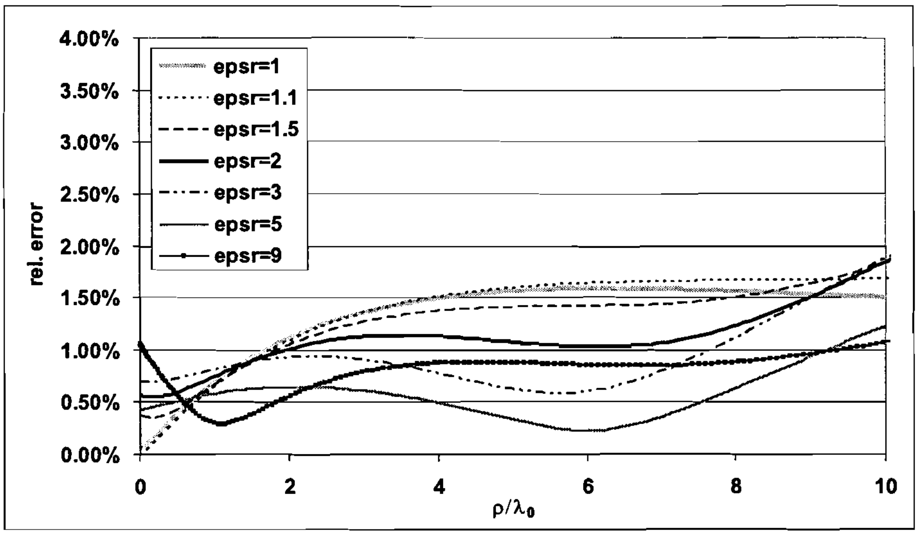

Figure 5.12: relative error in the integral I_1 between the far-field asymptotic-expression and the SDP for various relative permittivities at a height $|Z| = 6\lambda_0$ and a slab thickness of $d_1 = 0.1\lambda_0$.

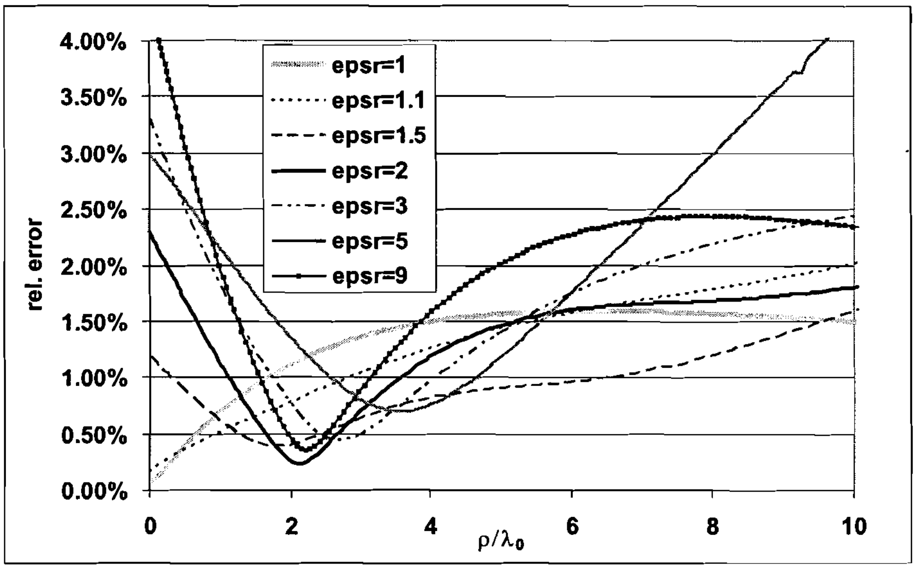

Figure 5.13: relative error in the integral I_1 between the far-field asymptotic-expression and the SDP for various relative permittivities at a height $|Z| = 6\lambda_0$ and a slab thickness of $d_1 = 0.3\lambda_0$.

Chapter 6

Conclusions and recommendations

To obtain a higher efficiency when solving Sommerfeld Integrals, we have deformed the Sommerfeld Integration Path (SIP) to the faster converging Steepest-Descent Path (SDP). This contour deformation is allowed as long as all encountered singularities, due to surface- and leaky-waves inside the slab(s), are taken into account as well. Therefore, the exact location of these singularities is necessary, since their residues have to be computed. The search process to find these singularities takes some extra effort. However, the computation time of this search routine is considerably reduced if we calculate the zeros of the denominator instead of the poles of the Transmission-Line Green's Functions (TLGF's). This is the reason why we have chosen for an approach in which we have to calculate these TLGF's for each stratified structure by hand, since this way the denominator of the TLGF is obtained explicitly. Since this calculation is a very time-consuming job, we only have considered those structures which are mostly used in practice.

To evaluate the numerical results obtained via the Method of Steepest Descent, we have compared it with a slightly deformed SIP, called the First-Contour Deformation (FCD). This path avoids all singularities in the plane of integration, and therefore no information regarding their location is needed. For this evaluation, we have considered a structure with a single slab excited by a magnetic dipole located on the ground plane below the slab. We have observed that the relative error in the results between integration along the SDP and the FCD, becomes the highest for small ρ if source and observer are located at the same height. First of all, this is due to the *leaky-wave singularities* that are located far away from the real k_ρ-axis, i.e. $\mathrm{Im}(k_\rho) \ll 0$, but their residues are still significant for small ρ and thus have to be added to the integral. However, since the search area is limited, the most lower singularities will not be found, which introduces an error in the final result. We also discovered that the relative error increases if we increase the slab thickness, since then the amount of leaky-wave singularities in a similar area increases. Secondly, the *tail lengths* of the SDP and FCD in the imaginary k_ρ-plane are of great importance. Their lengths have to be increased as ρ decreases to obtain accurate results, since the Hankel function does not decay rapidly for small ρ and consequently convergency of the integrand takes longer. Also a large *thickness* and high *relative permittivity* of the slab have a negative effect on the relative error between the numerical results.

The efficiency of the Method of Steepest Descent has been measured by the average computation time per integral. These computation times depend mostly on the *tail length* and the *length* L of the search area to find leaky-wave poles. To obtain better performances, we divided part of the $\rho(\lambda_0)$-axis into four intervals with various tail lengths and avoided the influence of surface- and leaky-wave poles by changing the SDP in their vicinity. For structures with two half spaces, the SDP is about 1.5 times faster than integration along the FCD, and for structures with one half space about 3 to 4 times. If the structure is terminated by two perfectly conducting ground planes, only the residues of the surface-wave poles have to be computed, and therefore the SDP is about 45 times faster than the FCD. Since the search process to find these surface-wave poles is absent if we integrate along the FCD, we have obtained break-even points. These denote the amount of integrals beyond which integration along the SDP is faster than integration along the FCD.

If the angle ψ increases, where ψ is the angle between the source and observation point, the most lower leaky-wave poles in the k_ρ-plane are already accounted for by the integral along the SDP and consequently the relative error in the results between the two paths decreases. Also the integrand decays faster to zero, owing the exponential $e^{-jk_z|z - z'|}$, which decays exponentially if the path is located on the upper Riemann sheet.

For a grounded structure with a single slab on top, we have obtained some minimum distances ρ beyond which we can apply the integration along the SDP if the amount of integrals is higher than the break-even point. We have observed that for a minimum distance of $\rho = 0.01\lambda$, the relative error remains below the assumed maximum tolerable error of 2% for a total slab thickness which is less than $d = 0.4\lambda_0$ and relative permittivities $\varepsilon_r \leq 9$, otherwise, the minimum distance ρ increases. If we wish to decrease the computation time for these cases, larger search areas should be used or other acceleration methods, as for example the one of [17].

Further, we have seen that it is very difficult to obtain a distance beyond which we can use the far-field asymptotic expressions. For a structure with one ground plane, but without slabs, it is still possible to determine this distance, however, as soon as slabs are involved, this distance varies rapidly. Therefore, these expressions should be used carefully.

Computation time can be further reduced if we use a Laguerre-Gauss quadrature to compute the integral for the non-oscillating exponentially decaying end of the tail, instead of the Gauss-Kronrod quadrature. Also the time needed to perform the search process can be reduced, owing to the pattern in the location of the leaky-wave poles.

Bibliography

[1] M. Abramowitz, I.A.Stegun, "Handbook of Mathemetical Functions with Formulas, Graphs, and Mathematical Tables," Dover Publications, New York, 1965.

[2] C.A. Balanis, "Antenna Theory: Analysis and Design," second edition, Chichester, Wiley, 1997

[3] W.C. Chew, "Waves and Fields in Inhomogeneous Media," Van Nostrand Reinhold, New York, 1990.

[4] R.V. Churchill, J.W. Brown, R.F. Verhey, "Complex Variables and Applications," McGraw-Hill Book company, Third Edition, 1974.

[5] R.E. Collin, "Field Theory of Guided Waves," McGraw-Hill Book company, 1990.

[6] L.B. Felsen, N. Marcuvitz, "Radiation and Scattering of Waves," Prentice-Hall, 1973.

[7] W. Fulks,"Complex Variables: an Introduction," Marcel Dekker Inc., 1993.

[8] I.S. Gradshteyn, I.M. Ryzhik, "Table of Integrals, Series and Products," Academic Press, fifth edition, 1994.

[9] G.L. James, "Geometrical Theory of Diffraction for Electromagnetic waves," Peter Peregrinus LTD., 1976.

[10] L. Kuiper, R. Timman, "Handbook of Mathematics," Pergamon Press Ltd., First English Edition 1969.

[11] A. Kyrala, "Applied Functions of a Complex Variable," Wiley-Interscience, 1972.

[12] D.P. Laurie, "Calculation of Gauss-Kronrod Quadratue Rules," Math. Comp., vol. 23, pp.1133-1145, 1997

[13] F. Ling, J-M. Jin, "Discrete Complex Image Method for Green's Functions of General Multilayer Media," IEEE Trans. Microwave and Guided Wave Letters., vol. 10, pp.400-402, Oct. 2000.

[14] A. Neto, Private communication.

[15] K.A. Michalski, J.R.Mosig, "Green's Functions in Integral Equation Formulations," IEEE Trans. Antennas Propagat., vol. 45, pp.508-519, Mar. 1997.

[16] K.A. Michalski, "Extrapolation Methods for Sommerfeld Integral Tails," IEEE Trans. Antennas Propagat., vol. 46, pp.1405-1418, Oct. 1998.

[17] F. Olyslager, H. Derudder, "Series Representation of Green Dyadics for Layered Media Using PMLs," IEEE Trans. Antennas Propagat., vol. 51, pp. 2319-2326, Sept. 2003.

[18] L.A. Rubenfeld, "A First Course in Applied Complex Variables", John Wiley & Sons, 1985.

[19] M.N.O. Sadiku, "Elements of Electromagnetics," Oxford University Press, Inc., second edition, 1995.

[20] A.G. Tijhuis, "Electromagnetic Inverse Profiling," VNU Science Press BV, 1987.

[21] A.G. Tijhuis, A. Rubio Bretones, "Transient Excitation of a Layered Dielectric Medium by a Pulsed Electric Dipole," IEEE Trans. Antennas Propagat., vol. AP-48, pp.1673-1684, Oct. 2000.

[22] K. Umashankar, A.Taflove, "Computational Electromagnetics," Artech House Inc., 1993.

Appendix A

Pole locations for general structures

A way to locate the poles of the functions $A_n(k_\rho, z, z')$ for an *arbitrary* structure will be discussed in this appendix. Again, we use the numerical search routine of Section 4.1.1, to obtain the pole locations in the k_ρ-plane. However, the denominator of the functions $A_n(k_\rho, z, z')$ is not derived analytically this time, as we did for the practical cases of Section 2.3. Now, we fill a matrix containing the transmission-line equations at each transition between two different layers. Since the voltage and current at these transitions should be continuous, owing to the fact that the tangential components of the electric and magnetic field are continuous there, we obtain two equations at every transition. Together with the transmission-line equation at the source point, a square matrix is made. A 7 × 7 matrix, for a magnetic source located on a ground plane is, for example, given by

$$\begin{bmatrix} a_{11} & a_{12} & 0 & 0 & 0 & 0 & 0 \\ a_{21} & a_{22} & a_{23} & a_{24} & 0 & 0 & 0 \\ a_{31} & a_{32} & a_{33} & a_{34} & 0 & 0 & 0 \\ 0 & 0 & a_{43} & a_{44} & a_{45} & a_{46} & 0 \\ 0 & 0 & a_{53} & a_{54} & a_{55} & a_{56} & 0 \\ 0 & 0 & 0 & 0 & a_{65} & a_{66} & a_{67} \\ 0 & 0 & 0 & 0 & a_{75} & a_{76} & a_{77} \end{bmatrix} \begin{bmatrix} V_1^+ \\ V_1^- \\ V_2^+ \\ V_2^- \\ V_3^+ \\ V_3^- \\ V_4^+ \end{bmatrix} = \begin{bmatrix} 1 \\ 0 \\ 0 \\ 0 \\ 0 \\ 0 \\ 0 \end{bmatrix},$$

for a structure with three transitions. Hence, the amount of layers determines the size of the square matrix. The **determinant** of this matrix gives an expression for the denominator of the functions $A_n(k_\rho, z, z')$. We will calculate it with a LU factorization. It is obvious that the computation time increases as the amount of layers increase. For those selections in *Table* 5.6, which have a ground plane, the computation times are given in *Table* A.1. We observe that these times are still much faster than the ones where we have determined the poles of the functions $A_n(k_\rho, z, z')$. Since the analytical derivation of the denominator for each selection is very time-consuming, especially as the amount of layers increases, this

Selection	Time for poles of GF(sec)
13	16
14	21
15	26

Table A.1: time needed to calculate of the determinant of a general matrix containing the poles a stratified structure.

gives us a general way to determine the pole locations for *arbitrary* structures.

Appendix B

Multiple-valued functions

A multiple-valued function is a function for which several distinct values correspond to one and the same point. While trigonometric, hyperbolic, exponential and integer power functions are all single-valued functions, since they only have one solution to each complex number z, their inverses are multiple-valued functions. In this appendix, we will show that the logarithm function, the inverse of the exponential function, is such a multiple-valued function. Next, the complex square root function will be discussed, which is a double-valued function, since every complex number we obtain two solutions. Finally, a combination of the two, the complex arcsin function, will be presented.

B.1 Complex logarithm function

The exponential function e^z maps every complex number z to a well-defined number e^z [18]. However, its inverse function, the logarithm $ln(z)$, maps an infinite number of values. If we transform the complex number z from cartesian coordinates to polar coordinates, the complex logarithm function is given by

$$\ln(z) = \ln(x + jy) = \ln(re^{j\theta}) = \ln(r) + j\theta, \tag{B.1}$$

where the angle θ is shown in Figure B.2. Remembering the fact that

$$e^{j\theta} = e^{j(\theta + 2n\pi)}, \tag{B.2}$$

where n is an integer value, gives for the same complex number more solutions, i.e.,

$$\ln(z) = \ln(r) + j(\theta + 2n\pi). \tag{B.3}$$

Riemann solved this problem by stating that complex numbers with more than $2\pi j$ difference are not the same number, at least as far as the logarithm function is concerned. This means that if the domain is defined correctly, the logarithm function will be single-valued.

For the logarithm the starting point in the complex k_ρ-plane is arbitrary. Let us choose it along the negative real k_ρ-axis. Then, this axis is called a *branch cut*. As soon as we pass through such a branch cut, we encounter a phase difference of $2\pi j$ and go to another *Riemann sheet*.

The endpoint of the branch cut is called a *branch point*. If we encircle this point, $f(k_\rho)$ does not return to its original value anymore. For the logarithm function the branch point is located at the origin. A possible way to plot this function is shown in Figure B.1. Here, two of the infinite number of Riemann sheets of the complex logarithm function are plotted. Since k_ρ is complex and therefore $\ln(k_\rho)$ as well, we actually need four dimensions to plot the Riemann sheets. This fourth dimension is achieved by introducing colors. The imaginary part of $\ln(k_\rho)$ is represented this way. As long as we do not encounter an abrupt color change, the imaginary part is continuous.

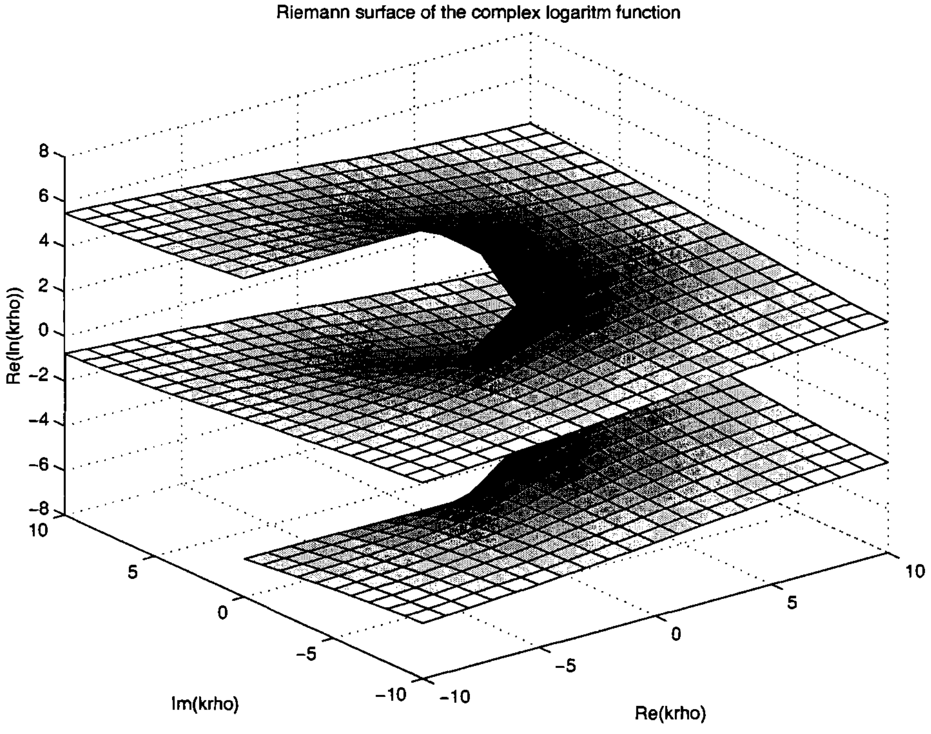

Figure B.1: the complex logarithm function $\ln(k_\rho)$ in the complex k_ρ-plane.

Since these plots are hard to work with, we can make the plot two dimensional as shown in Figure B.2, where the k_ρ-plane, with its branch cut and branch point, is plotted. Hence,

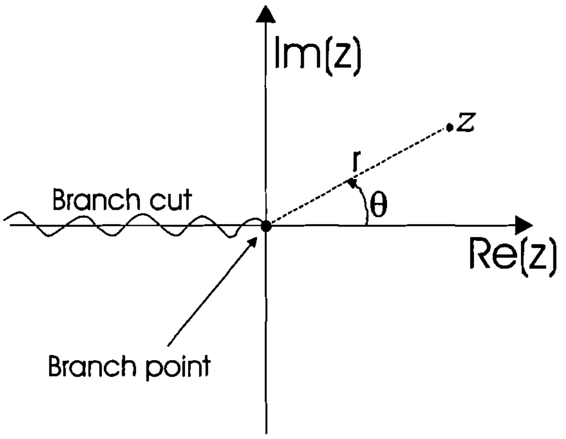

Figure B.2: branch point and branch cut of the complex logarithm function in the z-plane.

passing through a branch cut means that we go to a higher or lower Riemann sheet.

B.2 Complex square root function

Now, let us consider the square root of a complex number z. Since the square root is the inverse of an integer power function, it is a multiple-valued function. Transformation to polar coordinates gives

$$\sqrt{z} = \sqrt{re^{j\theta}} = \sqrt{r}e^{j\theta/2}. \tag{B.4}$$

However, this function does not have an infinite number of Riemann sheets as we encountered with the complex logarithm function. Since after a phase difference of $4\pi j$, we obtain an identical solution, i.e.,

$$\sqrt{r}e^{j\theta/2} = \sqrt{r}e^{j(\theta/2\,+\,2\pi)}. \tag{B.5}$$

Though, after a phase difference of $2\pi j$, the complex square root becomes

$$\sqrt{r}e^{j\theta/2} = \sqrt{r}e^{j(\theta/2\,+\,\pi)} = \sqrt{r}e^{-j\theta/2}, \tag{B.6}$$

implying that this function has <u>two</u> Riemann sheets. In Figure B.3 the Riemann surface of the complex square root function $\sqrt{k_\rho}$ is plotted. Again the colors represent the fourth dimension. Notice that indeed a passage twice around the origin gets us to the original sheet again. So, the branch point is located at the origin and the branch cut is chosen along the negative real k_ρ-axis. The two dimensional plot of the k_ρ-plane is therefore the same as the one for the logarithm function of Figure B.2.

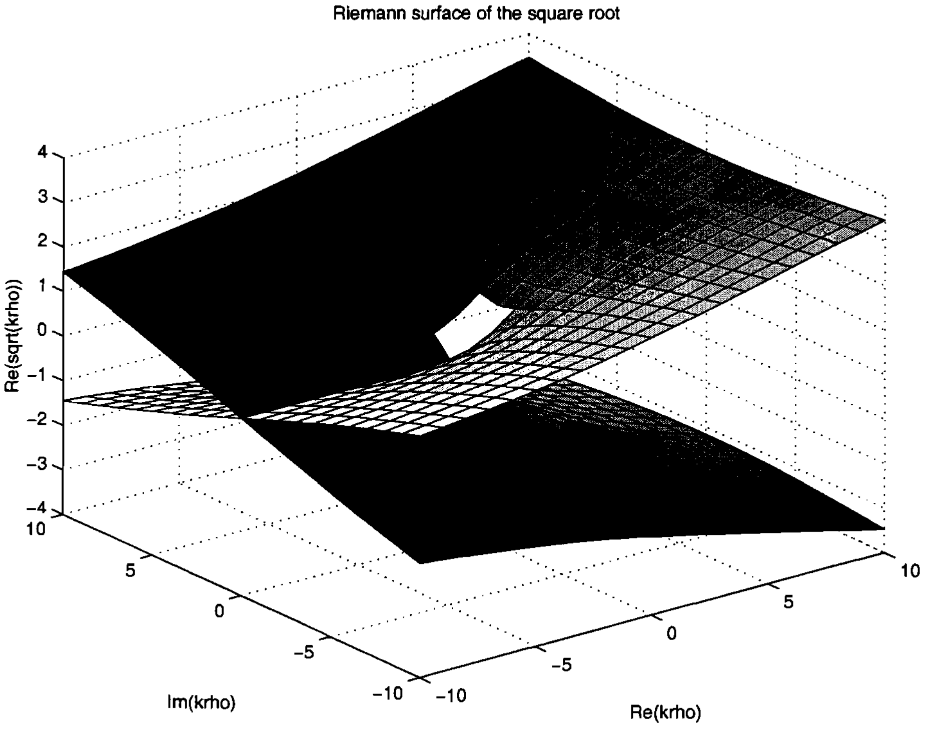

Figure B.3: the complex square root function $\sqrt{k_\rho}$ in the complex k_ρ-plane.

B.3 Complex arcsin function

Since the complex arcsin function is the inverse of the sine function, we can write is as follows:

$$z = \sin\alpha = \frac{e^{j\alpha} - e^{-j\alpha}}{2j}. \tag{B.7}$$

Then α becomes

$$\alpha = \frac{\ln(jz \pm \sqrt{-z^2+1})}{j}. \tag{B.8}$$

This function has branch points in $z = \pm 1$. The branch cuts are located on the real z-axis from $-\infty$ to -1 and from 1 to ∞, as shown in Figure B.4.

Figure B.5 shows the location of the branch points and branch cuts as well. To guarantee continuity of the function when we pass through a branch cut, the '$\pm$'-sign of Equation (B.8) changes sign.

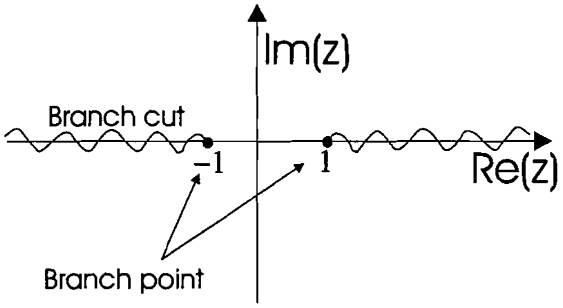

Figure B.4: branch point and branch cut of the complex arcsin function in the z-plane.

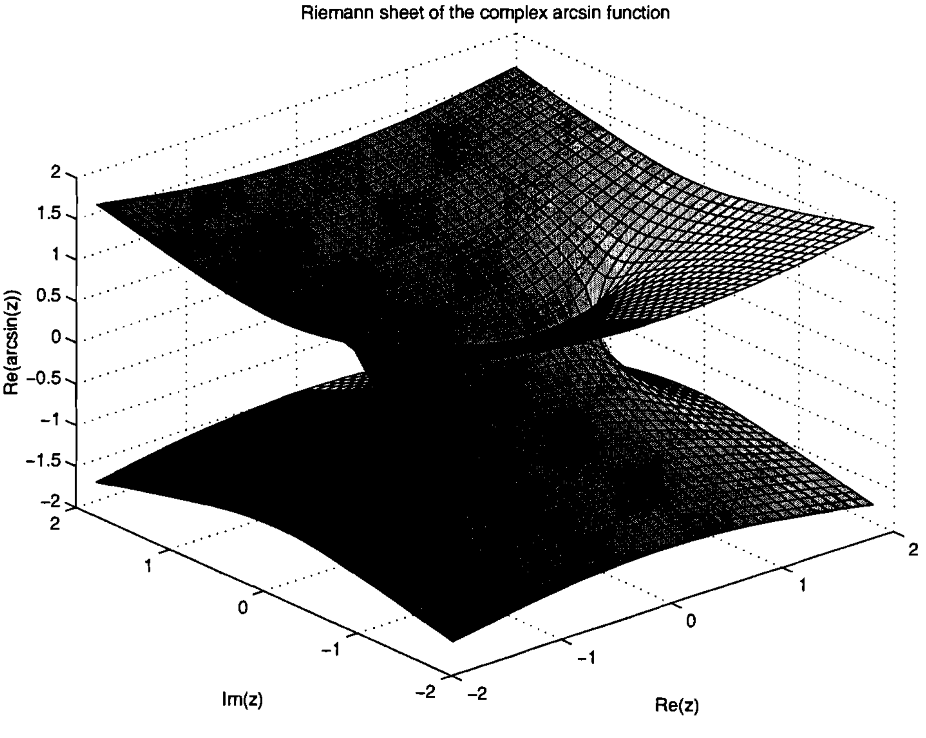

Figure B.5: the complex arcsin function in the complex z-plane.

Appendix C

Further evaluation of spatial Green's function

The inner integral of the spatial Green's function of Equation (2.49) is calculated analytically in Section 2.2.1. The spatial dyadic Green's functions of the four cases for various types of source and observer will be stated in the next sections.

C.1 Magnetic fields from magnetic sources

The integrals I_n are defined as

$$I_1 = \int\limits_{-\infty}^{\infty} \left[- I^v_{TE} - I^v_{TM} \right] H_0^{(2)}(k_\rho \rho) k_\rho dk_\rho, \tag{C.1a}$$

$$I_2 = \int\limits_{-\infty}^{\infty} \left[I^v_{TE} - I^v_{TM} \right] H_2^{(2)}(k_\rho \rho) k_\rho dk_\rho, \tag{C.1b}$$

$$I_3 = \int\limits_{-\infty}^{\infty} \frac{1}{k_z(z')} Y_{TE}(z') I^i_{TE} H_1^{(2)}(k_\rho \rho) k_\rho^2 dk_\rho, \tag{C.1c}$$

$$I_4 = \int\limits_{-\infty}^{\infty} \frac{1}{k_z(z)} Y_{TE}(z) V^v_{TE} H_1^{(2)}(k_\rho \rho) k_\rho^2 dk_\rho, \tag{C.1d}$$

$$I_5 = \int\limits_{-\infty}^{\infty} \frac{1}{k_z(z) k_z(z')} Y_{TE}(z) Y_{TE}(z') V^i_{TE} H_0^{(2)}(k_\rho \rho) k_\rho^3 dk_\rho, \tag{C.1e}$$

which results into the following table for the spatial dyadic Green's functions of $\underline{\underline{g}}^{h,m}$:

	M_x	M_y	M_z
H_x	$\frac{1}{8\pi} I_1 + \frac{1}{8\pi} \cos(2\phi) I_2$	$\frac{1}{8\pi} \sin(2\phi) I_2$	$\frac{1}{4\pi j} \cos\phi I_3$
H_y	$\frac{1}{8\pi} \sin(2\phi) I_2$	$\frac{1}{8\pi} I_1 - \frac{1}{8\pi} \cos(2\phi) I_2$	$\frac{1}{4\pi j} \sin\phi I_3$
H_z	$\frac{1}{4\pi j} \cos\phi I_4$	$\frac{1}{4\pi j} \sin\phi I_4$	$-\frac{1}{4\pi} I_5$

Table C.1: spatial dyadic Green's functions $\underline{\underline{g}}^{h,m}(x, y, z, z')$ in terms of the integrals I_n.

C.2 Electric fields from magnetic sources

We define the following integrals

$$\begin{aligned}
I_1 &= \int_{-\infty}^{\infty} \left[V_{TM}^v + V_{TE}^v\right] H_0^{(2)}(k_\rho \rho) k_\rho dk_\rho, && \text{(C.2a)}\\
I_2 &= \int_{-\infty}^{\infty} \left[V_{TM}^v - V_{TE}^v\right] H_2^{(2)}(k_\rho \rho) k_\rho dk_\rho, && \text{(C.2b)}\\
I_3 &= \int_{-\infty}^{\infty} \frac{1}{k_z(z')} Y_{TE}(z') V_{TE}^i H_1^{(2)}(k_\rho \rho) k_\rho^2 dk_\rho, && \text{(C.2c)}\\
I_4 &= \int_{-\infty}^{\infty} \frac{1}{k_z(z)} Z_{TM}(z) I_{TM}^v H_1^{(2)}(k_\rho \rho) k_\rho^2 dk_\rho, && \text{(C.2d)}\\
I_5 &= 0, && \text{(C.2e)}
\end{aligned}$$

which gives the spatial dyadic Green's function $\underline{\underline{\boldsymbol{g}}}^{e,m}$ in *Table* C.2.

	M_x	M_y	M_z
E_x	$-\frac{1}{8\pi}\sin(2\phi) I_2$	$-\frac{1}{8\pi} I_1 + \frac{1}{8\pi}\cos(2\phi) I_2$	$\frac{1}{4\pi j}\sin\phi I_3$
E_y	$\frac{1}{8\pi} I_1 + \frac{1}{8\pi}\cos(2\phi) I_2$	$\frac{1}{8\pi}\sin(2\phi) I_2$	$-\frac{1}{4\pi j}\cos\phi I_3$
E_z	$-\frac{1}{4\pi j}\sin\phi I_4$	$\frac{1}{4\pi j}\cos\phi I_4$	0

Table C.2: spatial dyadic Green's functions $\underline{\underline{\boldsymbol{g}}}^{e,m}(x, y, z, z')$ in terms of the integrals I_n.

C.3 Electric fields from electric sources

The different integrals are

$$I_1 = \int_{-\infty}^{\infty} \left[- V_{TM}^{i} - V_{TE}^{i} \right] H_0^{(2)}(k_\rho \rho) k_\rho dk_\rho, \tag{C.3a}$$

$$I_2 = \int_{-\infty}^{\infty} \left[V_{TM}^{i} - V_{TE}^{i} \right] H_2^{(2)}(k_\rho \rho) k_\rho dk_\rho, \tag{C.3b}$$

$$I_3 = \int_{-\infty}^{\infty} \frac{1}{k_z(z')} Z_{TM}(z') V_{TM}^{v} H_1^{(2)}(k_\rho \rho) k_\rho^2 dk_\rho, \tag{C.3c}$$

$$I_4 = \int_{-\infty}^{\infty} \frac{1}{k_z(z)} Z_{TM}(z) I_{TM}^{i} H_1^{(2)}(k_\rho \rho) k_\rho^2 dk_\rho, \tag{C.3d}$$

$$I_5 = \int_{-\infty}^{\infty} \frac{1}{k_z(z) k_z(z')} Z_{TM}(z) Z_{TM}(z') I_{TM}^{v} H_0^{(2)}(k_\rho \rho) k_\rho^3 dk_\rho. \tag{C.3e}$$

For the spatial dyadic Green's function $\underline{\underline{g}}^{e,j}$, this results in *Table* C.3

	J_x	J_y	J_z
E_x	$\frac{1}{8\pi} I_1 + \frac{1}{8\pi} \cos(2\phi) I_2$	$\frac{1}{8\pi} \sin(2\phi) I_2$	$\frac{1}{4\pi j} \cos\phi I_3$
E_y	$\frac{1}{8\pi} \sin(2\phi) I_2$	$\frac{1}{8\pi} I_1 - \frac{1}{8\pi} \cos(2\phi) I_2$	$\frac{1}{4\pi j} \sin\phi I_3$
E_z	$\frac{1}{4\pi j} \cos\phi I_4$	$\frac{1}{4\pi j} \sin\phi I_4$	$-\frac{1}{4\pi} I_5$

Table C.3: spatial dyadic Green's functions $\underline{\underline{g}}^{e,j}(x, y, z, z')$ in terms of the integrals I_n.

C.4 Magnetic fields from electric sources

The following integrals are defined for this case

$$\begin{aligned}
I_1 &= \int\limits_{-\infty}^{\infty} \left[I^i_{TM} + I^i_{TE}\right] H_0^{(2)}(k_\rho \rho) k_\rho dk_\rho, && \text{(C.4a)}\\
I_2 &= \int\limits_{-\infty}^{\infty} \left[I^i_{TM} - I^i_{TE}\right] H_2^{(2)}(k_\rho \rho) k_\rho dk_\rho, && \text{(C.4b)}\\
I_3 &= \int\limits_{-\infty}^{\infty} \frac{1}{k_z(z')} Z_{TM}(z') I^v_{TM} H_1^{(2)}(k_\rho \rho) k_\rho^2 dk_\rho, && \text{(C.4c)}\\
I_4 &= \int\limits_{-\infty}^{\infty} \frac{1}{k_z(z)} Y_{TE}(z) V^i_{TE} H_1^{(2)}(k_\rho \rho) k_\rho^2 dk_\rho, && \text{(C.4d)}\\
I_5 &= 0, && \text{(C.4e)}
\end{aligned}$$

which results in *Table* C.4 for the spatial dyadic Green's function $\underline{\underline{g}}^{h,j}$.

	J_x	J_y	J_z
H_x	$-\frac{1}{8\pi}\sin(2\phi) I_2$	$\frac{1}{8\pi} I_1 + \frac{1}{8\pi}\cos(2\phi) I_2$	$-\frac{1}{4\pi j}\sin\phi I_3$
H_y	$-\frac{1}{8\pi} I_1 + \frac{1}{8\pi}\cos(2\phi) I_2$	$\frac{1}{8\pi}\sin(2\phi) I_2$	$\frac{1}{4\pi j}\cos\phi I_3$
H_z	$\frac{1}{4\pi j}\sin\phi I_4$	$-\frac{1}{4\pi j}\cos\phi I_4$	0

Table C.4: spatial dyadic Green's functions $\underline{\underline{g}}^{h,j}(x, y, z, z')$ in terms of the integrals I_n.